Growth and Characterization of Magnetic Perovskite and Perovskite-related Phases

By

I-TING CHIU
DISSERTATION

Submitted in partial satisfaction of the requirements for the degree of

DOCTOR OF PHILOSOPHY

in

Chemical Engineering

in the

OFFICE OF GRADUATE STUDIES

of the

UNIVERSITY OF CALIFORNIA

DAVIS

Approved:

_____

Yayoi Takamura, Chair

_____

Roopali Kukreja

_____

Shirley Chiang

Committee in Charge

2021

Growth and Characterization of Magnetic Perovskite and Perovskite-related Phases

ABSTRACT

Perovskite oxides ABO_3, where A is usually an alkaline-earth or rare-earth cation and B a transition metal element, have received a great deal of interest because of their wide range of functional properties such as ferroelectricity, superconductivity, and ferromagnetism, with a unique sensitivity to external stimuli including chemical doping, lattice strain, and electrical and magnetic fields. This sensitivity makes perovskite oxides highly tunable materials, and further investigation into their fundamental physical properties are critical for future device development. Unlike metallic systems that have been studied for decades for a variety of applications such as hard disk drives and logic/memory devices, thin films of perovskite oxides are a relatively new field and they show diverse functional properties compared to their metal counterparts, creating novel pathways for designing specific device applications. The work in this dissertation was focused on extending our current knowledge on the magnetic perovskite oxides, and further exploring the ability to precisely tune and control their functional properties.

Resonant x-ray reflectivity, soft x-ray photoemission electron microscopy (X-PEEM), and magnetometry measurements were employed to study the physical properties of perovskite

oxide $Nd_{0.5}Sr_{0.5}MnO_3$ (NSMO) thin films grown on (110)-oriented $SrTiO_3$ substrates, where it displays coupled magnetic and electronic transitions from paramagnetic/insulator to ferromagnetic (FM)/metal and then to antiferromagnetic (AFM)/charge-ordered insulator with decreasing temperature, due to the anisotropic strain state induced by the underlying substrate. The FM and AFM properties of the NSMO film were probed as a function of temperature using soft x-ray magnetic spectroscopy, and the coexistence of lateral FM and AFM domains was demonstrated using X-PEEM, showing both vertical and lateral magnetic phase separation in the film. These characterization techniques demonstrate the multiple magnetic and electronic phase transitions in the NSMO films, and thus the possibility and diversity of functional properties to be applied in next generation devices.

Ion migration-induced modification of physical properties is another emerging research direction in the search for tunable materials that can revolutionize the growing field of neuromorphic computing. Among the candidate materials, perovskite oxides including cobaltites ($La_{0.7}Sr_{0.3}CoO_3$, LSCO and $LaCoO_3$, LCO) and ferrites ($La_{0.7}Sr_{0.3}FeO_3$, LSFO) are ideal candidates due to their high oxygen vacancy conductivity, relatively low oxygen vacancy formation energy, and strong coupling of the magnetic and electronic properties to the oxygen stoichiometry. The evolution of the physical properties of LSCO, LCO and LSFO thin films upon exposure to highly reducing environments was studied in this dissertation. In the cobaltite

systems, the rarely-reported crystalline Ruddlesden-Popper (RP) phase was observed, which involved the loss of both oxygen anions and cobalt cations upon annealing, where the cobalt is found as isolated Co ions or Co nanoparticles. First principles calculations confirm that the concurrent loss of oxygen and cobalt ions is thermodynamically possible. In the ferrite system, however, the films remained in the oxygen-deficient perovskite phase even when annealed at the most reducing conditions explored in this dissertation. The strong correlation of the magnetic and electronic properties to the crystal structure highlights the potential of utilizing ion migration as a basis for emerging applications such as neuromorphic computing.

ACKNOWLEDGEMENTS

First and foremost, I would like to offer my sincerest gratitude to my advisor Dr. Yayoi Takamura for her consistent support and guidance throughout my Ph.D. career. With a chemical engineering background, I am extremely thankful for her immense patience to teach me the basic knowledge of materials science and guide me through the world of research. Her dedication to research and teaching was outstanding, however, what impressed me even more was the mentorship and friendship she provided. Her understanding and thoughtfulness throughout made my graduate school experience an enjoyable journey.

I would like to thank Dr. Roopali Kukreja and Dr. Shirley Chiang for offering excellent courses to teach me fundamental materials science concepts, and for serving on my committee from the qualifying exam to this final dissertation review. I would also like to acknowledge Dr. Kukreja for the fruitful collaboration with her research group, and for granting our group to use some of her equipment.

I would like to thank all the current and former members in the Takamura Research Group (TRG) for the invaluable help and discussion throughout my studies at UC Davis. I thank Dr. Rajesh Chopdekar, Dr. Yue Jia, Dr. Michael Lee and Dr. Alex Kane for providing the

mentorship guidance and answering all my questions with great patience, as well as showing me how to operate and maintain the laboratory equipment in Davis and offering training at the beamlines at the Stanford Synchrotron Radiation Lightsource and the Advanced Light Source. Thanks to Nolan Ahlm and Dayne Sasaki for the interesting discussions and excellent company during the long synchrotron beamtime shifts, and for maintaining the x-ray diffractometer and the pulsed laser deposition chamber. I would also like to thank Mingzhen Feng for the insightful discussions and the experimental assistance. When she joined the group, her friendship throughout made a big difference to my graduate school life and made me feel at home in Davis. I would express my gratitude to all the other TRG members I worked with: Aleksey Ionin, Kyle Hoke, Atharva Deshpande, Hudson Shih, Ishmam Nihal, Ryan Fillhouer, Peifen Lyu, Eric Zhu and Daniel Jiang.

I am grateful for the support and guidance from Dr. Padraic Shafer, Dr. Alpha N'Diaye, Dr. Andreas Scholl, and Dr. Elke Arenholz at the Advanced Light Source and Dr. Apurva Mehta at the Stanford Synchrotron Radiation Lightsource. This dissertation would not have been possible without the research help from Dr. Min-Han (Hank) Lee, Dr. Zhen Zhang, Dr. Shenli Zhang, Dr. Ivan Schuller, Dr. Shriram Ramanathan and Dr. Giulia Galli. I would also like to acknowledge all the collaborators that I have worked with: Dr. Shaobo Cheng, Larry Heki, Michael Taejoon Park, Dr. Yahya Mohtashami, Dr. Pavel N. Lapa, Dr. Jon A. Schuller, and Dr.

Yimei Zhu. This work was supported as part of the Quantum Materials for Energy Efficient Neuromorphic Computing, an Energy Frontier Research Center funded by the U.S. Department of Energy (DOE), Office of Science, Basic Energy Sciences under Award No. DE-SC0019273.

I cannot thank my parents and my brothers enough for their unconditional love and guidance, supporting my decision to pursue a graduate degree in the U.S. I would also like to thank Demmy Hsiao, Candy Chiu, Jessica Tseng and Shian Lin for all the emotional support during the most stressful periods of my program. Lastly, I thank Gary for his patience and (virtual) company, bringing me joy along with YY and Fatty through numerous videocalls, motivating me throughout my graduate school studies and helping me deal with the stress and challenges I faced.

Table of Contents

Chapter 1: Introduction

In order to maintain the current pace of innovation in memory/logic devices and neuromorphic computing applications, novel classes of materials and alternative device designs are imperative for further breakthroughs [1]. Complex metal oxides (CMOs), a broad category of materials containing oxygen and at least two different metal cations, are promising candidates due to their diverse functional properties such as ferromagnetism, ionic conductivity, controllable phase transformations and abrupt metal-to-insulator transitions [2-9]. Within the family of CMOs, perovskite crystal structures have received a great deal of interest because of the wide range of their functional properties. Perovskite originally refers to a crystalline mineral consisting of a calcium titanium oxide ($CaTiO_3$) repeating unit, which later lent its name to any material with the same structure but different cation elements [10]. Consequently, the terms “perovskite” and “perovskite structure” are often used interchangeably nowadays.

Although most perovskite structures are generally a type of oxide, there are still some exceptions in the natural environment [11]. Fluoride perovskites such as $NaMgF_3$ is a good and common example. In addition, $MgCNi_3$ is also a metallic perovskite compound that contains no oxygen. It has drawn lots of attention recently because it exhibits superconducting properties.

1.1 Perovskite Oxides

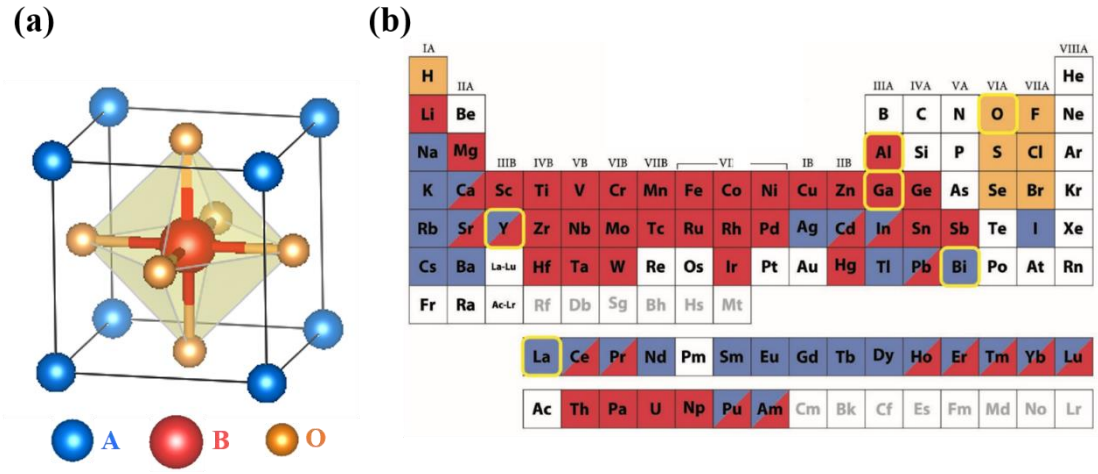

Fig. 1.1. *(a) The ideal cubic perovskite structure with chemical formula ABO_3 where A and B are cations and O is an oxygen anion. (b) A periodic table showing the different elements that can be incorporated into the atomic sites of a perovskite structure [16]. Blue elements can be substituted on the A-site, red elements on the B-site, and orange elements on the face center positions.*

Analogous to $CaTiO_3$, the general chemical formula for perovskite oxides is ABO_3. Ideally, perovskite has a cubic structure (**Fig. 1.1(a)**): an *A*-site cation is usually an alkaline earth or rare earth element which is located at the corners of the lattice, while *B*-site cations could be *3d*, *4d*, and *5d* transition metal elements which sit at the center of the unit cell. These two ions differ in their ionic radii ("*A*" atoms are usually larger than "*B*" atoms). *O* is the oxygen anion that bonds to both *A* and *B* ions and sits at the face-centered positions. Perovskite oxides have

recently drawn attention due to the wide variety of functional properties which can be controlled through chemical substitutions on the *A* and *B* sites, as well as the oxygen stoichiometry [12-15].

Since different ions exist in the perovskite structure, not only the size of the cations and anions but the attractive and repulsive forces between them would affect the stability of an ideally cubic lattice. Due to these interactions between different ions, the buckling and distortions of less symmetric unit cells are characterized by periodic tilting, increase in size of the unit cell, and non-cubic crystal systems [17]. The Goldschmidt tolerance factor, *t*, can be used to predict the crystal symmetry of a perovskite structure by calculating the ratio between the two unit-cell lengths, *i.e.*, *A*-*O*-*A* along the face centers and *O*-*B*-*O* along the octahedral axes.

$$t = \frac{r_A + r_O}{\sqrt{2}\,(r_B + r_O)} \qquad \textbf{(1.1)}$$

As shown in **Eqn. (1.1)**, the r_A, r_B and r_O refer to the ionic radii of ions *A*, *B*, and *O*, respectively. The relationship between the Goldschmidt tolerance factors and their corresponding crystal structures are summarized in **Table 1.1**.

Table 1.1 *Room temperature calculation of the Goldschmidt tolerance factor, t, and the resulting crystal symmetry.*

Tolerance factor t	Crystal symmetry
$1 < t$	Hexagonal or Tetragonal
$0.9 \leq t \leq 1$	Cubic
$0.7 \leq t < 0.9$	Orthorhombic or Rhombohedral
$t < 0.7$	Trigonal or Non-perovskite

The crystal asymmetry makes the perovskite structures versatile in several aspects, for example, the distortion in $BaTiO_3$ perovskite structure can lead to electric dipoles and ferroelectric properties [18]. Among all of the non-cubic variants, the orthorhombic (*e.g.*, $GdAlO_3$ [19]) and tetragonal (*e.g.*, $PbTiO_3$ at room temperature [20]) phases are the most common. Because of the ordered and disordered variants, complex perovskite structures with two different B cations are also possible [21,22]. Introducing cation dopants of similar size can induce octahedral rotations and further change the length and angles of the *B-O-B* bonds. These rotations will affect the electronic interactions between the *d* orbitals in transition metals and the *2p* orbitals in oxygen ions, and are thereby the sources of the interesting functional properties of perovskite oxides. In summary, perovskite oxides are considered as strongly correlated electronic systems which combine intriguing functionalities such as ferromagnetism with interrelated spin, charge, lattice, and orbital degrees of freedom.

1.1.1 Crystal Field Splitting

The properties of the perovskite oxides are strongly coupled to the electrostatic interactions between the metallic *3d* and oxygen-*2p* orbitals when their *B*-sites are occupied by the first-row transition metals. In a spherical field, the *3d* orbitals are energetically degenerate; however, for the transition metal ions in a perovskite structure, the octahedral bonding environment with the oxygen ions breaks the five-fold *d*-orbital degeneracy. The oxygen has $2p_x$, $2p_y$, and $2p_z$ orbitals, resulting in the d_{z^2} and $d_{x^2-y^2}$ orbitals of the transition metal having more interactions with the oxygen *p*-electrons. The greater spatial overlap and static/coulombic repulsion of the electron clouds increase the energy of the two 3*d* orbitals. The higher energy levels which are doubly degenerated are denoted as e_g orbitals, *i.e.*, d_{z^2} and $d_{x^2-y^2}$ orbitals which have electron distributions with lobes oriented parallel to the crystallographic axes similarly to the *O*-2*p* orbitals; the other three degenerated orbitals (d_{xy}, d_{xz}, and d_{yz} orbitals) are t_{2g} orbitals, which have a reduced energy state and have lobes aligned 45 degrees from the crystallographic axes. The resultant energy splitting of the transition metal *3d*-orbitals is shown in **Fig. 1.2**. The octahedral crystal field stabilization energy (CFSE, Δ_{oct}) is a function of the ligand bonding strength, while the relative energy levels of e_g and t_{2g} obeys the conservation of energy.

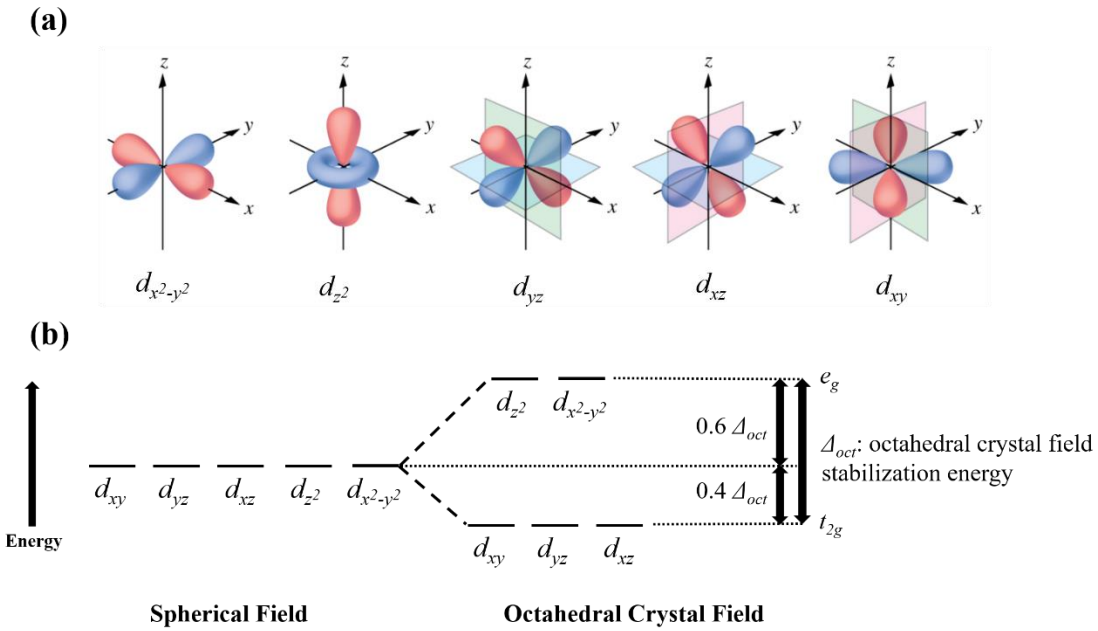

Fig. 1.2. *(a) Schematic of 3d-orbital electron distributions on a Cartesian coordinate axis [23]. (b) Crystal field splitting in their relative energy levels for an octahedrally-coordinated B-cation in perovskite oxides.*

When electrons fill the orbitals starting from the lowest energy, high-spin, intermediate-spin, or low-spin states can be possible, depending on the competition of the CFSE and the spin/Hund's pairing energy (*i.e.*, the coulombic energy cost of placing a second electron into a half-filled *d*-orbital). A high-spin state maximizes the number of unpaired elections but fills higher energy orbitals, whereas a low-spin state avoids filling higher energy orbitals but takes up the cost of increased spatial overlap arising from the pairing of electrons. Intermediate-spin states are the mix of high-spin and low-spin states and can occur in structures with strong *2p* hybridization, for example, the perovskite cobalt oxides, or cobaltites [24].

These metallic *d*-orbital energy levels can be further affected by epitaxial strain states in thin films or Jahn-Teller distortions. A thin film under a compressive strain in the *xy* lattice plane can break the degeneracies of the e_g and t_{2g} levels: due to the compression of the lattice along the *x* and *y* directions that leads to an increase in orbital overlap, the $d_{x^2-y^2}$ orbital shifts to an energy higher than that of the d_{z^2} orbital. Similarly, the d_{xz} and d_{yz} orbitals have lower energy relative to the d_{xy} orbital. Splitting can also occur through Jahn-Teller distortions, which are best illustrated by the example of $3d^9$ or high-spin $3d^4$ ions, when the electron is expected to occupy either of the e_g orbitals with equal probability. In order to minimize the overall energy of the system, the *3d* orbitals with a z-component can shift to higher or lower energies depending on the intrinsic properties of the material (**Fig. 1.3**). This energy shift can also affect the overlap of oxygen-*2p* and metallic *3d* orbitals. The crystal field splitting and crystal symmetry can influence orbital occupation and affect the magnetic behavior.

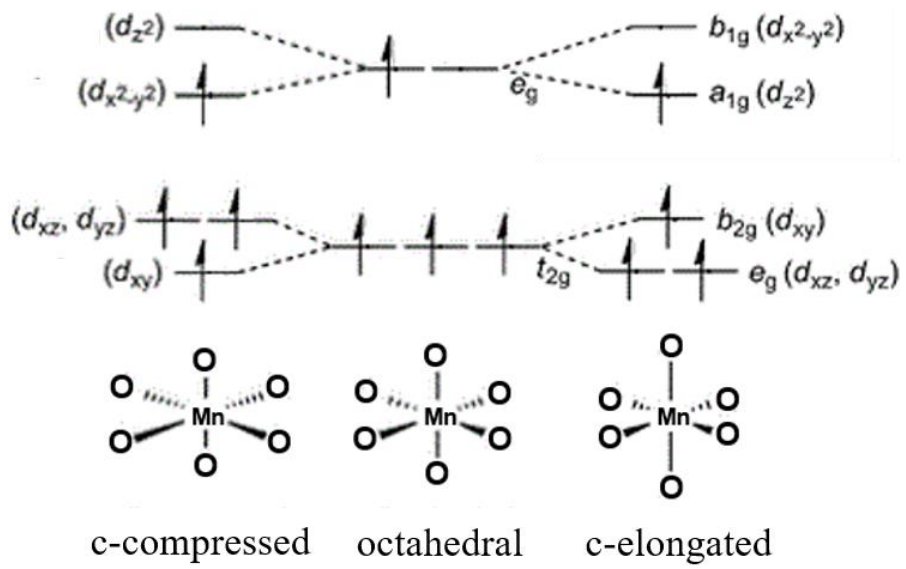

Fig. 1.3*. Two possible scenarios of the metallic d-orbital energy splitting in an octahedrally bonded manganite affected by epitaxial strain states in thin films or Jahn-Teller distortions [25]. Starting from the middle octahedral, the Jahn-Teller effect is active when the high-spin* Mn^{3+} e_g *electron has degeneracy in energy. In order to minimize the overall energy of the system, the 3d orbitals with a z-component can shift to higher or lower energies depending on the intrinsic properties of the material. This energy shift can also affect the overlap of oxygen-2p and Mn-3d orbitals.*

1.1.2 Magnetism in Perovskite Oxides

The quantum mechanical exchange interactions between adjacent atoms are the sources for ferromagnetism in metallic materials. The electron occupancy in an orbital is dictated by Fermi-Dirac statistics (where the Coulomb repulsion between two electrons is greater when their spatial overlap is larger or when they exist in the same orbital) and the Pauli exclusion principle

(which states that electrons occupying the same orbital must have opposite spins). Combining these two phenomena, the electrostatic energy can be minimized by aligning the electron spins parallel to each other to avoid the electrons sharing the same orbital and to increase the distance of electron distribution so as to decrease the repulsion between them.

The direct exchange mechanism can explain the magnetic interaction of electrons from adjacent metallic atoms. However, the strength of the direct exchange mechanism decays exponentially as a function of the distance between atoms and thus it does not describe the magnetism in perovskite oxides. The magnetically active cations in perovskites (usually the *B*-site ions) are separated by oxygen anions so the bond distance is too great for electrons to interact directly. Their magnetic properties are instead explained by indirect exchange mechanisms (Goodenough – Kanamori – Anderson rules), where the ferromagnetic and antiferromagnetic properties are determined by the orbital filling of the two metal cations between the metal-oxygen-metal (M_1-O-M_2) covalent bonds [26-28].

One important indirect exchange mechanism in oxides is the double exchange mechanism, which explains the magnetic behavior involving the oxygen-*2p* and metal-*d* orbitals. In the case of the doped rare earth manganites [29], the manganese ions are in different valence states, *i.e.*, Mn^{3+} and Mn^{4+} ions, with an oxygen anion bonded in between. In this double exchange

interaction of the high-spin state shown in **Fig. 1.4(a)**, one of the oxygen *2p* electrons jumps into an available e_g orbital of the Mn^{4+} ion, and the electron in the e_g orbital of the Mn^{3+} ion then fills that vacant hole in the oxygen-*2p* orbital. This movement involves two electrons, lowering the system overall energy by decreasing the electrostatic repulsion between manganese and oxygen orbitals. Due to this interaction, the electron spins are all parallel in both Mn^{3+} and Mn^{4+} ions to avoid incurring any energy. The parallel spin alignment favors the ferromagnetic character in the material. Furthermore, the electrons are physically transferring between the ions, resulting in the metallic conducting behavior being concurrent with the ferromagnetic property.

This ferromagnetic property induced by the double exchange mechanism dominates at low temperature below the Curie temperature (T_C) of a material. At high temperature above T_C, the magnetic moments are randomized by the large thermal energy, resulting in paramagnetic behavior. Compared to the ferromagnetic region, the resistivity above T_C shows insulating behavior (negative dependence of resistivity and temperature) as the double exchange mechanism does not dominate anymore. This implies that it is not energetically favorable for the electrons to transfer between the ions, and the spin flip events will impact the resistivity through mobility.

Consider another example of the indirect exchange mechanism, the super-exchange mechanism in La_2CoMnO_3 which contains both Co^{2+} and Mn^{4+} as *B*-site cations [30]. The Co^{2+} ions have the electron configuration as $3d^7$ and their e_g orbitals are half-filled (when Co^{2+} ions are in high-spin state) while the Mn^{4+} ions have the configuration of $3d^3$ and their e_g orbitals are empty. When the interacting orbitals bond together, the spins must align antiparallel. If the Co^{2+} ions have one up-spin electron in each of their e_g orbitals, the oxygen spin that bonds with them must have the down-spin orientation. According to the Pauli exclusion principle, the other oxygen electron must be up-spin, and thus the electrons in Mn^{4+} ions also have to be up-spin since their e_g orbitals are empty in the high-spin state. In this pairing configuration, the electrostatic energy can be minimized. This scenario then dictates a ferromagnetic alignment between the perfect ordering of the two *B*-site ions (Co and Mn ions) in the double perovskite structure La_2CoMnO_3 (**Fig. 1.4(b)**).

Another type of super-exchange mechanism can be demonstrated in the case when both M_1 and M_2 metal cations have the same valence state, for example, $LaFeO_3$, where the Fe ions are in the high spin $3d^5$ state. If both of the Fe–O interacting orbitals are forming covalent bonds, the oxygen spins must align antiparallel to both Fe ions. The Pauli exclusion principle forces the oxygen spins in the same orbital to have opposite directions, and therefore the neighboring Fe ions have antiparallel alignment: the up spin in the oxygen orbital must couple with the Fe ion

with all the down spins and vice versa (**Fig. 1.4(c)**). As a result, $LaFeO_3$ has an antiferromagnetic ordering throughout the crystal and has insulating properties due to virtual hopping instead of real hopping of electrons.

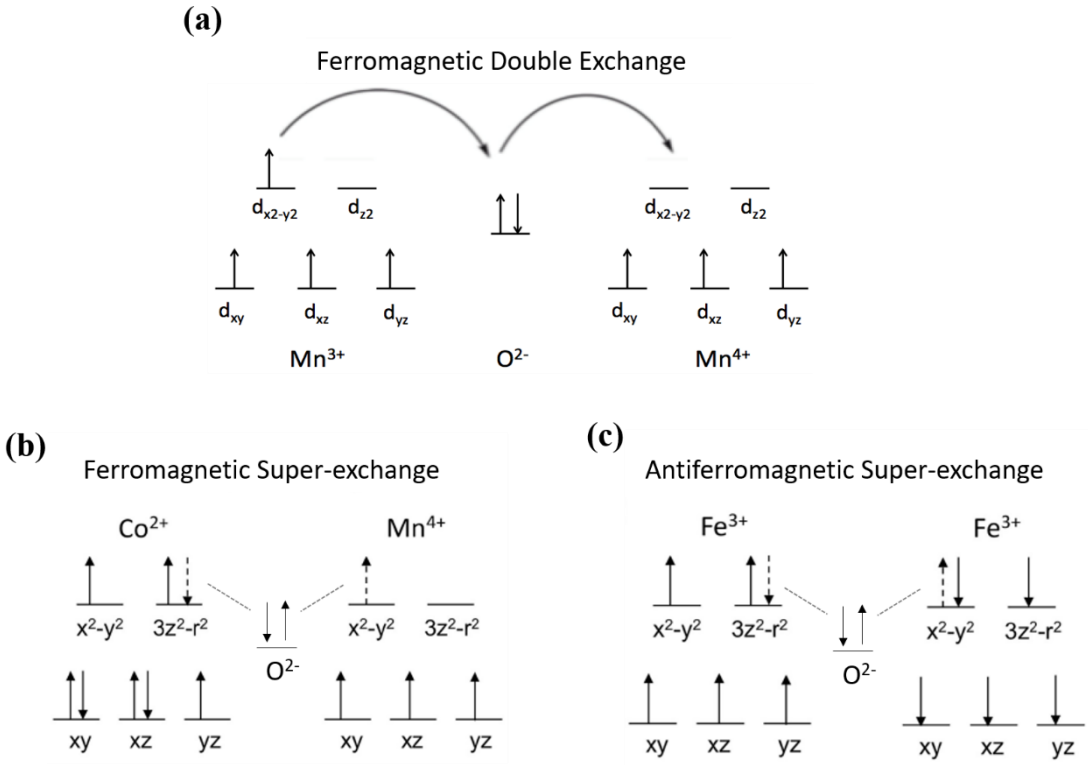

***Fig. 1.4**. (a) Ferromagnetic double-exchange, (b) Ferromagnetic super-exchange, and (c) Antiferromagnetic super-exchange examples [31]. In (b) and (c), the dashed arrows refer to the spins from O-2p orbitals.*

As shown in **Fig. 1.5**, the antiferromagnetism (AFM) can be categorized into different types depending on their moment orientations. The most common ones are A, C, and G-type AFM.

An A-type AFM has moments with ferromagnetic ordering within individual (001) crystallographic planes, while adjacent layers have antiparallel alignment; a C-type AFM has ferromagnetic alignment within (110) planes and adjacent planes have antiparallel alignment; and finally, a G-type AFM has antiparallel alignment between each nearest magnetic moment which can also be interpreted as ferromagnetic alignment within (111) planes. Besides these three types of AFM, E-type and CE-type AFM are also possible, as illustrated in **Fig. 1.6**.

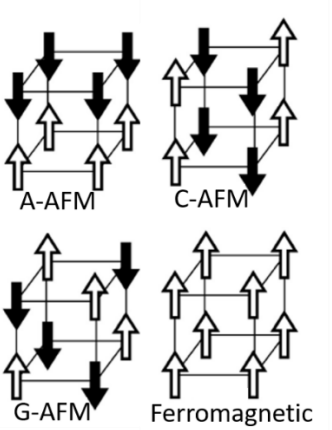

Fig. 1.5*. Illustrations of A, C, and G-type AFM ordering and FM ordering. White and black arrows are magnetic moments oriented up and down, respectively [32].*

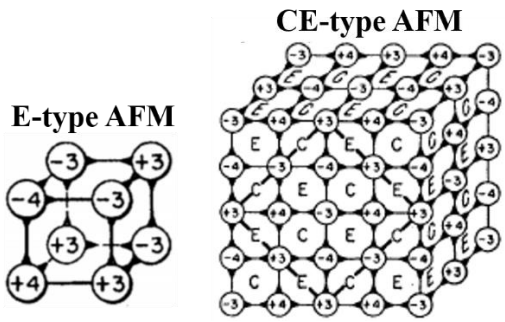

***Fig. 1.6**. E-type and CE-type AFM structure [33], where the latter is a combination of C-type and E-type AFM structures. The circles refer to perovskite B-site ions: the numbers indicate the valence state, and the plus or minus signs refer to the spin directions. To sum up, B^{3+}/up-spin, B^{4+}/up-spin, B^{3+}/down-spin, and B^{4+}/down-spin are denoted as +3, +4, -3, -4, respectively.*

1.1.3 $Nd_{0.5}Sr_{0.5}MnO_3$

The hole-doped manganite $Nd_{1-x}Sr_xMnO_3$ is one of the perovskite oxides that received a great deal of attention lately due to its rich phase diagram of different magnetic and electronic phases depending on the Sr doping level, offering tantalizing possibilities for energy-efficient logic and memory applications. As shown in **Fig. 1.7**, the phases include paramagnetic (PM) insulator, ferromagnetic (FM) metal, and (canted) antiferromagnetic (AFM) insulator/metal depending on the Sr doping level. When changing temperature at x = 0.5 ($Nd_{0.5}Sr_{0.5}MnO_3$, NSMO), two magnetic and electronic transitions can occur. As temperature decreases, the PM/insulating phase transforms to the FM/metallic phase at around 250 K, and then the FM/conducting phase changes to the AFM charge-ordered insulating phase at around 150 K.

The temperature where the PM phase changes to FM phase is known as the Curie temperature (T_C), and the temperature of the FM-to-AFM transition is known as the Neél temperature, T_N.

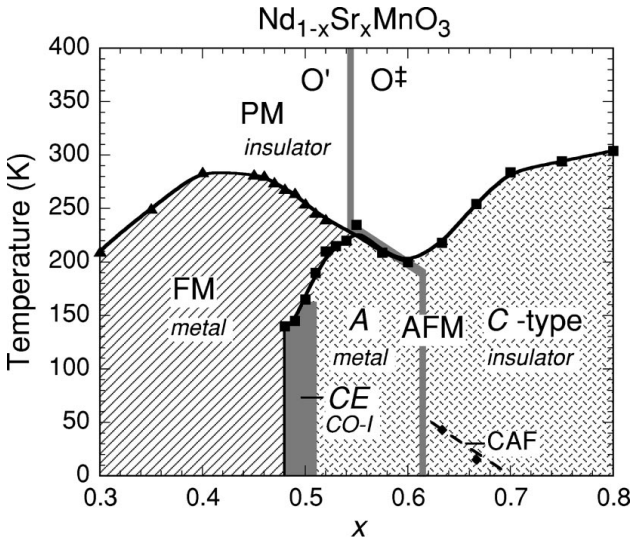

Fig. 1.7*. Phase diagram of bulk $Nd_{1-x}Sr_xMnO_3$ [34]. The notations are as follows, (in alphabetical order) A: A-type AFM; C: C-type AFM; CAF: canted AFM state; CE: CE-type AFM; CO-I: charge-ordered insulator; O': orthorhombic crystal structure; O++: tetragonal crystal structure.*

The Jahn-Teller (JT) effect is necessary to describe the transitions in NSMO as a function of temperature. For bulk NSMO, elongation of the *a*- and *b*-lattice parameters, and compression of the *c*-parameter occurs due to the intrinsic properties of this material [34]. These changes alter the overlap between manganese-*3d* and oxygen-*2p* orbitals from the ideal MnO_6 octahedron. Thus the *3d* orbitals with a *z*-component shift toward higher energy levels, and the

$3d_{x^2-y^2}$, $3d_{xy}$ orbitals shift toward lower energy levels (**Fig. 1.3** left), supporting the JT distortions already present in the Mn^{3+} ions which have the $3d^4$ electron configuration.

As temperature decreases, the transition of NSMO from the PM/insulating to the FM/metal phase is easily explained: the thermal energy is no longer enough to randomize the magnetic moments. When cooled to around 150 K, the JT distortion of Mn^{3+} ions drives the Mn^{3+} and Mn^{4+} ions into the charge-ordered CE-type AFM phase to minimize the overall energy, as shown in **Fig. 1.6** [33].

Unfortunately, stabilizing the FM/metal to AFM/insulator transition in NSMO thin films has proven to be rather difficult. According to previous literature [35,36], CE-type AFM ordering in NSMO films requires anisotropic strain in the in-plane lattice directions to further support the JT distortions. In order to provide some structural freedom and induce different strain states of the *a*- and *b*-axes of the BO_6 octahedron, the choice of (110)-oriented substrates is preferred. The *a*- and *b*-axes are both canted 45° out of the (110) surface plane, creating some freedom for the BO_6 octahedral bond directions to distort below T_N. This orientation presents a growth surface with a rectangular growth surface: the [001] lattice direction (*c*-parameter) of the film is strained to the substrate, while the other direction $[1\bar{1}0]$ is partially relaxed [36].

1.1.4 $La_{1-x}Sr_xCoO_3$

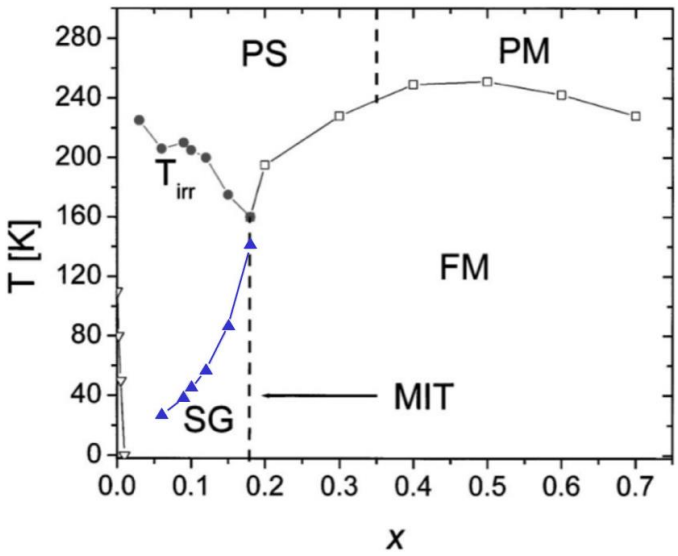

***Fig. 1.8**. Phase diagram of bulk $La_{1-x}Sr_xCoO_3$ [40]. The notations are as follows, SG: spin glass; PS: paramagnetic semiconducting; PM: paramagnetic metallic; FM: ferromagnetic metallic. T_{irr} denotes the temperature where the diversion occurs between zero-field-cooled and field-cooled M vs. T (Magnetization vs. Temperature) curves. MIT is the metal-to-insulator transition that takes place at the Sr doping level of x = 0.18 [39]. At x = 0, the spin-state transition in $LaCoO_3$ leads to ferromagnetic behaviors at ~ 4 to 120 K (denoted in open triangles) [40].*

In condensed matter physics, a spin glass (SG) is a disordered magnetic state where there is only short-range order of parallel magnetic spin alignment. As shown in the phase diagram in **Fig. 1.8**, $La_{1-x}Sr_xCoO_3$ exhibits SG behavior at low Sr doping level ($x < 0.18$), where the FM/metallic and non-magnetic/insulating clusters coexist. The clusters form a percolation

network above this critical Sr doping level and exhibit long-range magnetic order below its T_C [37-39]. Depending on the Sr doping, the FM/metallic behavior transforms to PM/semiconducting phase (when $x < 0.35$) or PM/metallic (when $x > 0.35$) phase above T_C, which ranges from ~ 200 to 240 K.

The SG behavior present in the low Sr doping regime can be identified in magnetization as a function of temperature (*M vs. T*) curves performed with field-cooled and zero-field cooled scenarios. When the sample is field-cooled, all of the ferromagnetic regions are aligned in the direction of the applied field; while in the case of zero-field cooling, the ferromagnetic spin orientations are affected by their surrounding anisotropic antiferromagnetic matrices arising from the super-exchange interactions between Co^{3+} - Co^{3+} and Co^{4+} - Co^{4+} ions. As shown in **Fig. 1.9**, T_{irr} denotes the temperature where the diversion occurs between zero-field-cooled and field-cooled *M vs. T* curves. The zero-field cooled *M vs. T* curve displays a peak at the freezing temperature (denoted in solid triangles in **Fig. 1.8**). Below the freezing temperature, the ferromagnetic regions are in a disordered state and the spins are oriented randomly due to the local antiferromagnetic anisotropy induced by the identical Co ions, giving rise to the spin glass behavior. Above the freezing temperature, the thermal energy is large enough to start randomizing the ferromagnetic moments and the magnetization thereby decreases.

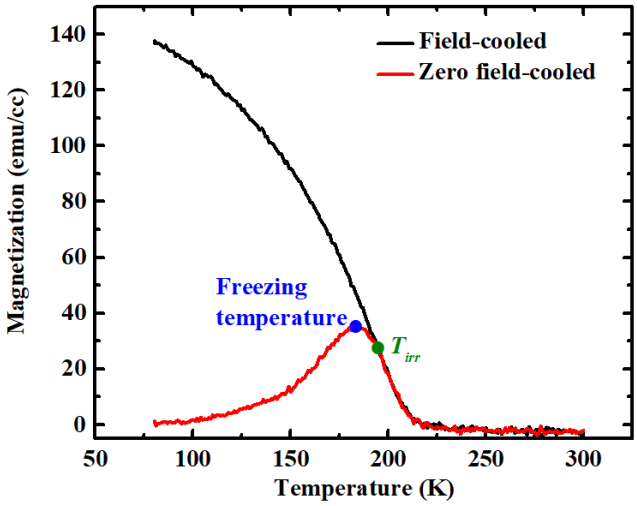

Fig. 1.9. *Film-averaged magnetization as a function of temperature of a field-cooled (black) and a zero field-cooled (red) case, measured along the [100] direction of a LSCO film grown on a* $(LaAlO_3)_{0.3}(Sr_2TaAlO_6)_{0.7}$ *(LSAT) substrate. During cooling, a magnetic field of 0.5 T was applied for the field-cooled case, while no magnetic field was applied for the zero field-cooled case. Both magnetization curves shown in the figure were measured upon warming from 80 K with an applied magnetic field of 0.08 T. In the zero field-cooled case (red curve), the ferromagnetic spins are originally in disordered orientations at low temperature with no magnetization, and they slowly begin to align as the temperature is increased, with a peak at the freezing temperature.*

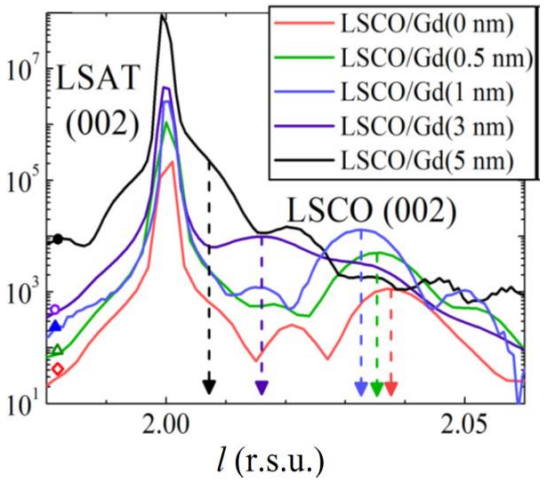

***Fig. 1.10**. By depositing a Gd capping layer on perovskite LSCO films, the spontaneous oxidation of Gd to GdO_x progressively leaches oxygen ions from the LSCO layer and leads to LSCO phase change. From the thinnest (red curve) to the thickest (black curve) Gd thicknesses, the film peak moves from higher to lower reciprocal space units, indicating the lattice parameter of the LSCO expands and phase change occurs.*

$La_{1-x}Sr_xCoO_3$ has been a candidate material for novel memory applications, next-generation ionic devices, and cathodes of solid oxide fuel cells [41]. At x = 0.3, $La_{0.7}Sr_{0.3}CoO_3$ (LSCO) is an ideal system for investigating phase transformations due to its high oxygen vacancy conductivity, relatively low oxygen vacancy formation energy, and strong coupling of the magnetic and electronic properties to the oxygen stoichiometry [42-47]. As shown in **Fig. 1.10**, structural changes have been demonstrated in LSCO by the deposition of ultrathin Gd layers of varying thicknesses [48,49]. The Gd capping layer on top of the LSCO films triggers the

spontaneous oxidation of Gd to GdO_x, progressively leaching oxygen ions from the bottom LSCO layer. This phenomenon leads to an expansion of the LSCO lattice parameter and further impact the associated magnetic and electrical properties of the films. The structural evolution of LSCO thin films upon exposure to highly reducing environments has also been studied [50], which highlights the potential of utilizing ion migration as a basis for emerging applications due to the strong correlation of the magnetic and electronic properties to the LSCO crystal structures.

1.2 Outlook

This dissertation focuses on the synthesis and characterizations of magnetic perovskite oxides, particularly on manganites, cobaltites, and ferrites. Chapter 2 describes the various techniques used to synthesize and characterize the properties of the magnetic perovskite oxides studied in the following chapters. Chapter 3 presents a study of the physical properties of NSMO thin films, which involves two temperature-dependent magnetic/electronic transitions. Phase transformations in LSCO thin films and their corresponding functional properties are investigated in Chapter 4. Then in Chapter 5 oxygen deficiency in LSCO thin films are quantified with a combination of theoretical explanations and experimental results across multiple complementary characterization techniques. Finally, the preliminary results of phase transformations in two other thin film samples ($LaCoO_3$ and $La_{0.7}Sr_{0.3}FeO_3$) are discussed in

Chapter 6. Chapter 7 includes a conclusion and some potential future work based on the outcomes from this dissertation.

Chapter 2: Experimental Techniques

This chapter provides a summary of the various experimental techniques used in the research described in this dissertation. All the thin film synthesis was performed by pulsed laser deposition and the structural characterization for measuring the film thickness, density, roughness, and lattice constants included x-ray reflectivity and high-resolution x-ray diffraction. A Lakeshore cryogenic probe station was used to measure the electrical transport properties of the films. The bulk magnetic properties were measured using a superconducting quantum interference device magnetometer from Quantum Design. Element-specific magnetic properties were measured using soft x-ray magnetic spectroscopy/microscopy.

2.1 Deposition Technique

2.1.1 Pulsed Laser Deposition

Pulsed laser deposition (PLD) is a versatile physical vapor deposition method effective for growing layers of perovskite oxide thin films and many other materials with complex compositions and structures. The simplicity of PLD make it well-suited for research purposes compared with other thin film deposition techniques including molecular beam epitaxy [51], chemical vapor deposition, radio frequency sputtering, and magnetron sputtering. With optimized growth conditions, the stoichiometric transfer of constituent elements from the ablated target to the film [52] can be obtained and high-quality thin films with thickness control

down to atomic layer precision can be deposited. A schematic diagram of a standard PLD system is shown in **Fig. 2.1**. The essential components of a PLD system consist of a vacuum system and a gas inlet, an ultraviolet laser (the KrF excimer laser with the wavelength of 248 nm was used in this dissertation), targets, and a substrate. The vacuum system and the gas inlet are used to pump and vent the chamber, respectively. The gas inlet is also for controlling the gas pressure during film growth. The focused laser beam with high intensity impinges the target in the deposition chamber. The target surface is then sublimated and partially ionized, forming the ablation plume. The plume, containing a variety of atomic, ionic and molecular species, is transported through the chamber and condenses onto the substrate (which is approximately 5-10 cm from the target and in the path of the plume). The substrate is affixed to a heater plate that can reach high temperatures and is often rotated to facilitate uniform film growth.

The growth parameters in a PLD system are interrelated so a trial-and-error process is typically used to obtain optimal growth conditions and to produce high-quality films. Sufficient energy density of the laser is crucial to create the plume of the ablated target materials and to achieve stoichiometric transfer of material from the target to the substrate. If the energy density is too low, film depositions only occur via evaporation with the heated target surface. This is undesired since the evaporation rates depend on the vapor pressures of the different elements in the target and would thus lead to non-stoichiometric film deposition. On the other hand, if

the laser energy density is too high, large particulates of target material are ejected and the film quality can degrade. Generally ~ 1-3 J/cm^2 provides sufficient energy to ensure stoichiometric deposition and in the meantime avoid large particulates. Laser energy density can be tuned through either the laser power or the laser spot size.

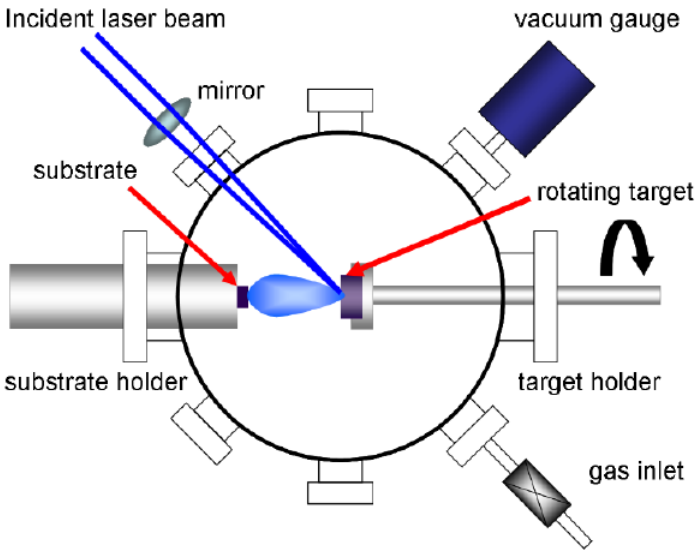

***Fig. 2.1**. A schematic diagram of a standard PLD system [53]. The focused laser beam with high intensity impinges the rotating target, allowing each laser pulse to strike different positions on the target. The target surface is then sublimated and partially ionized, forming the ablation plume. The plume is then transported through the chamber and condenses onto the substrate to form film growth.*

To avoid forming oxygen vacancies in the perovskite oxides and to successfully create a plume

in the PLD chamber, the synthesis and film growth procedures must be performed in an oxygen atmosphere in the range of 100-300 mTorr. This is crucial to maintain the magnetic properties of perovskite oxides and to support their indirect ferromagnetic exchange interactions that arise from the oxygen anions. Furthermore, by atomic collisions, the presence of (oxygen) gas during deposition can also lower the kinetic energy of the chemical species impinging on the substrate. The energetic ions within the plume can be detrimental to the substrate surface and prevent the deposited film from smooth interfaces and high crystallinity. The key to optimizing the oxygen pressure in a PLD film growth is to find a balance between oxygen incorporation in the growing films and the reduction of plasma kinetic energy to obtain films of high structural quality and desired functional properties.

The substrate temperature also plays an important role in the resulting film quality. The ionic species within the plume are first adsorbed onto the substrate surface, and heating the substrate provides thermal energy to assist surface diffusion of the deposited ions to the lowest energy sites for incorporation into the growing film. If the substrate temperature is too low, amorphous or nanocrystalline films are grown due to insufficient energy for appropriate surface diffusion. However, if the substrate temperature is extremely high, significant interdiffusion can occur between layers and thus prevent the formation of films with abrupt chemical interfaces. Certain species could also sublimate off the substrate if the temperature is too high. The optimization

of substrate temperatures should take into account both the surface diffusion and the interdiffusion between layers to obtain thin films with high structural quality.

2.1.2 Thin Film Growth Modes

The fundamental mechanism of film growth and nucleation is determined by the surface energies and the interfacial energy between the film and the substrate. As shown in **Fig. 2.2**, the growth modes can be categorized into one of the following four types: three-dimensional (3D) island growth, two-dimensional (2D) step-flow growth, 2D layer-by-layer growth, and Stranski-Krastanov growth. In 3D island growth, the ions prefer to form 3D clusters rather than bond to the substrate, covering an entire monolayer of material and usually resulting in a rough film surface due to the coarsening of the clusters. In contrast, for the step-flow mode, ions deposited on the growth front diffuse to naturally occurring step edges between adjacent levels of atomic planes. The growth then proceeds with the step flowing across the growth front, leaving a very smooth atomically flat surface with a terrace-like structure. Though the film interfacial quality is preserved in the step-flow mode, during growth it is difficult to monitor the completion of one atomic layer using reflection high-energy electron diffraction (RHEED). As a result, the 2D layer-by-layer growth mode is generally desired for epitaxial thin films since the monolayer of atoms covers the full substrate surface before the growth of the successive monolayers. It is capable of controlling the layer thickness in unit cell precision and

achieving chemically abrupt multilayers with high-quality crystalline quality. Lastly, Stranski-Krastanov growth is a combination of 3D island growth and 2D layer-by-layer growth. Several complete monolayers first grow in a layer-by-layer fashion, after which the films grow in clusters and island growth replaces layer-by-layer growth. The critical thickness where the transition takes place from layer-by-layer to island growth is determined by the lattice strain between the film and substrate and their corresponding surface energies.

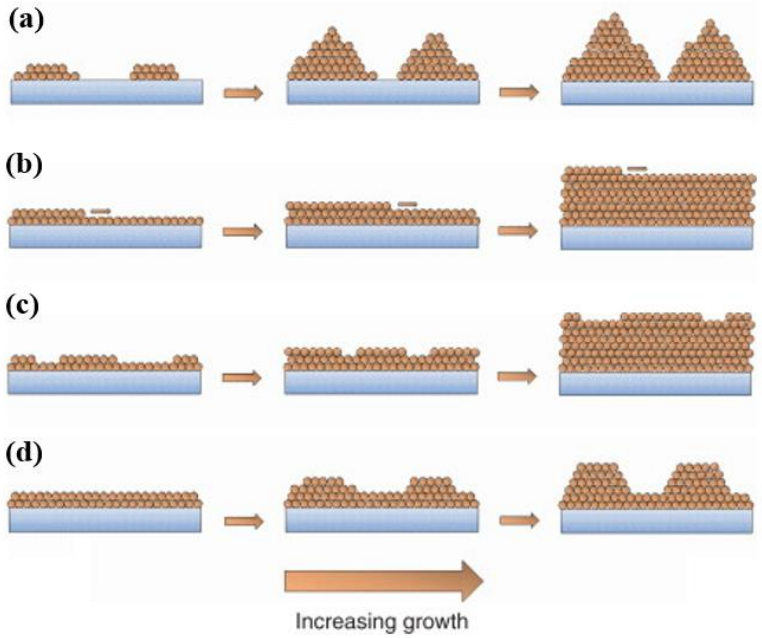

Fig. 2.2*. Illustrations of the basic growth modes including (a) 3D island, (b) 2D step-flow, (c) 2D layer-by-layer, and (d) Stranski–Krastanov growth [54]. The blue region refers to the substrate, while the orange spheres are the deposited ions.*

The growth mechanism is determined by the balance of three energies, *i.e.*, the energy between

the film and atmosphere (γ_F), the energy between the substrate and atmosphere (γ_S), and the energy between the film and substrate interface (γ_I). With the mechanical equilibrium shown in **Fig. 2.3**, the relationship between these energies can be described as follows:

$$\gamma_S = \gamma_F \cos\theta + \gamma_I \tag{2.1}$$

where θ is the contact angle between the film and the substrate.

Layer-by-layer growth takes place when $\theta = 0$, which means

$$\gamma_S \geq \gamma_F + \gamma_I \tag{2.2}$$

On the other hand, island growth occurs when the contact angle $\theta > 0$, which satisfies

$$\gamma_S < \gamma_F \cos\theta + \gamma_I \tag{2.3}$$

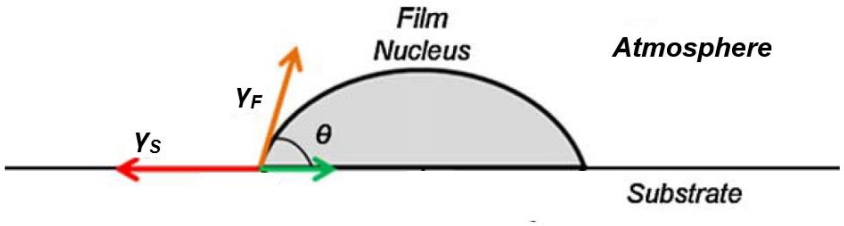

***Fig. 2.3**. Relevant surface energy terms during the film growth process and the contact angle formed between the film and substrate [55].*

In Stranski-Krastanov growth, the additional energy term, elastic energy, has to be taken into

consideration due to the lattice strain induced between the film and the substrate. At the initial stage of growth when the film is extremely thin, the growth process is dominated by the balance between the surface energy and the interfacial energy, resulting in the layer-by-layer growth. After a critical thickness, the growth mode transitions from 2D layer-by-layer growth to 3D island growth, in order to reduce the elastic energy in the film and relax the strain from lattice mismatch.

2.2 Structural Characterization

X-ray crystallography is an experimental technique to determine the crystalline structure of a material. A Bruker D8 Discover four-circle diffractometer was used for the structural characterization of the thin films investigated in this dissertation. The schematic diagram of an x-ray diffractometer is shown in **Fig. 2.4**.

For a lab-based x-ray diffractometer, the x-rays are typically generated by a copper anode, which produces three characteristic x-ray wavelengths from *K* shell emission: K_{α_1}, K_{α_2} and K_{β}. A parabolic Göbel mirror is used to filter the K_{β} radiation and produce mutually parallel beam of x-rays. To achieve high angular resolution, a Ge (220) two-bounce monochromator is placed in the incident beam path to remove the K_{α_2} radiation which has the lower intensity between the two K_{α} emissions. Slits are used for balancing the x-ray intensity and selecting the

collimated x-ray beam with high angular resolution.

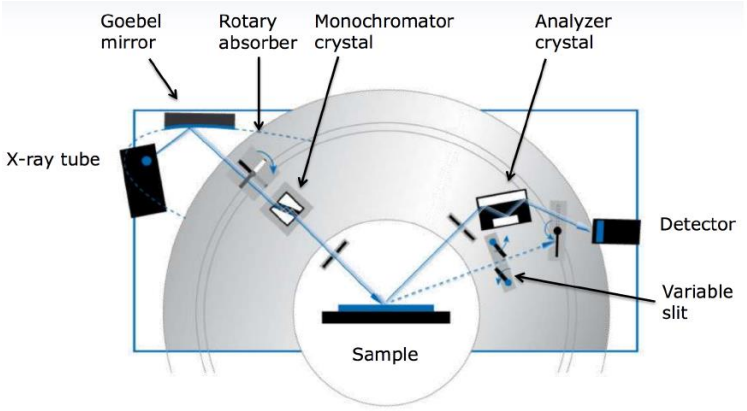

***Fig. 2.4**. A schematic diagram of an x-ray diffractometer [56]. A Göbel mirror and a monochromator crystal is used to filter the K_β and $K_{\alpha 2}$ radiation, respectively. Slits are used for balancing the x-ray intensity and selecting the collimated x-ray beam with high angular resolution. Rotary absorber can avoid saturating the detector for high intensity diffraction peaks, while having sensitivity for low intensity peaks. An analyzer crystal on the diffracted optics is not used in this dissertation.*

2.2.1 X-ray Reflectivity

X-ray reflectivity (XRR) is a surface characterization technique that utilizes incident x-rays at grazing angles relative to the sample surface and that measures their specular reflection. The x-ray beam gets reflected at the film surface and all interfaces between materials with different density, including the substrate-film interface. XRR is an ideal technique for determining key

structural information such as layer thickness, interfacial roughness, and density of a single layer or multi-layer thin films. The measurement geometry is illustrated in **Fig. 2.5**.

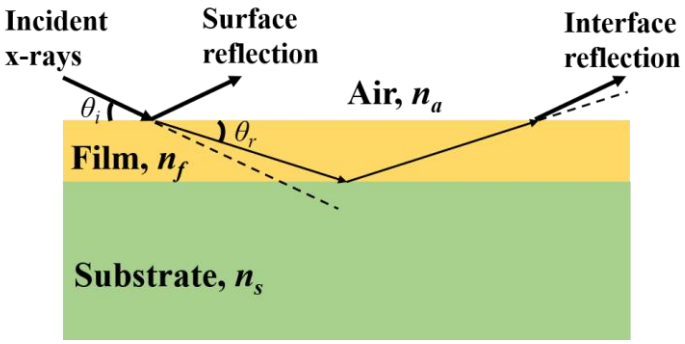

***Fig. 2.5**. Schematic geometry of a generic XRR measurement.*

According to Snell's Law, the relationship between the indices of refraction, n, and the reflection angles, θ, can be described as follows:

$$\frac{n_a}{n_f} = \frac{\cos\theta_r}{\cos\theta_i} \tag{2.4}$$

As displayed in **Fig. 2.5**, n_a, n_f, and n_s are the refractive indices of air, film, and substrate, respectively. θ_i is the angle between the incident x-rays and the film surface, while θ_r is the angle between the refracted x-rays and the film surface.

Since n is always less than 1 for x-rays in condensed matter, total external reflection occurs when the x-ray incident angle is below the critical angle θ_c.

$$\theta_c = \cos^{-1}\left(\frac{n_f}{n_a}\right) \tag{2.5}$$

The critical angle is a fingerprint to determine the density of a film as the refractive index of a material for hard x-rays is related to the density of electrons. Above the critical angle, the intensity of the reflected beam decreases exponentially towards the background level of the instrument. The intensity decays faster with larger surface or interfacial roughness due to the increased degree of diffuse scattering. An XRR curve of an LSCO thin film grown on $(LaAlO_3)_{0.3}(Sr_2TaAlO_6)_{0.7}$ (LSAT) substrate is shown in **Fig. 2.6**.

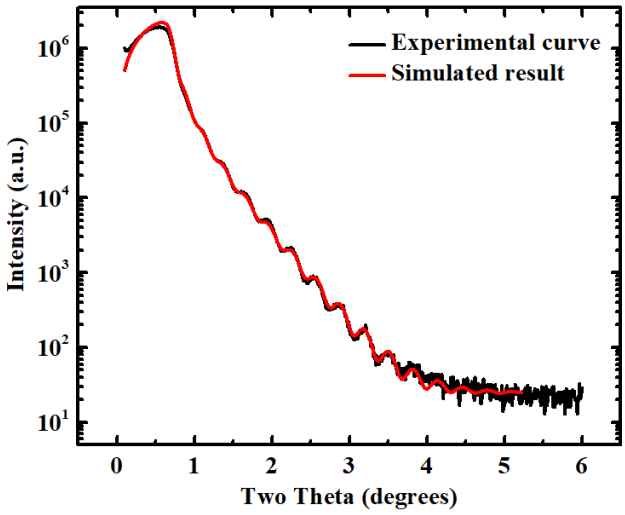

***Fig. 2.6**. Experimental and simulated XRR curves of a LSCO thin film with a thickness of 27.4 nm, roughness of 0.8 nm, and density of 6.79 g/cm^3.*

The oscillations in the XRR curve arise from the interference of the x-rays due to their wave nature. The intensity of the signals reflected from the film surface and from the film-substrate interface can add constructively or destructively, depending on the difference in the path length

which leads to a phase difference. This interference is primarily related to the x-ray incidence angle as well as the thickness and density of the film. In an XRR curve, the thickness is inversely related to the periodicity, and the density contrast between the film and the substrate can affect the amplitude of the oscillations. The amplitude of the oscillations can further be influenced by the roughness at film or film-substrate interfaces as rougher interfaces create more diffuse scattering.

Using synchrotron radiation with tunable energy, XRR profiles may be performed at energies near the absorption edges of atoms in each individual layer to obtain resonant XRR (RXRR) spectra. RXRR spectra takes into consideration both the real and imaginary parts of the dispersion correction factor, f' and f'', respectively. The f' depends strongly on x-ray energy which decreases abruptly at absorption edges [57]; in contrast, the f'' increases sharply at the absorption energy. The RXRR technique therefore provides increased sensitivity to the chemical contrast between thin films and substrates which have similar density. As shown in **Fig. 2.7**, the energy dependence of Co/Mn dispersion correction factors reveals that their differences are large enough to distinguish Co- and Mn-containing sublayers at their corresponding resonance edges, however, the contrast of f' and f'' between Co and Mn is much weaker at off-resonance energy such as 8000 eV (black dash line).

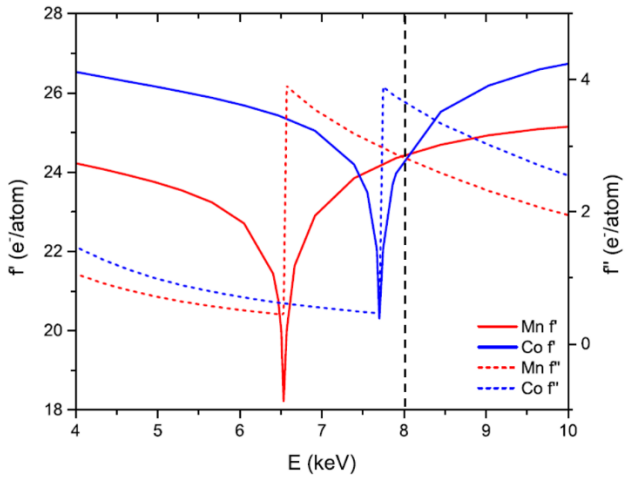

Fig. 2.7*. Dispersion correction factors, f' and f'', as a function of energy for metallic Mn and Co [58].*

2.2.2 High Resolution X-ray Diffraction

X-ray diffraction (XRD) is a non-destructive technique utilizing coherent scattering from atomic planes of a periodically-ordered crystal. The repeating units in the crystal can scatter the beam and diffract the x-rays into certain directions. The x-rays are diffracted in the same direction when they elastically scatter off electrons in a crystalline material, but the scattered x-rays add destructively at most combinations of incident angles and detector positions so no reflected signals can be detected. At specific conditions, however, the scattered beam can interact constructively and produce a sharp signal. These conditions can be described by Bragg's Law shown in **Eqn. 2.6**.

$$2d_{hkl}\sin\theta = n\lambda \tag{2.6}$$

where d_{hkl} is the atomic spacing between the *(hkl)* crystal planes in the lattice, θ is the incidence angle between the x-rays and the crystal plane, n is an integer, λ is the wavelength of the incoming x-ray beams. **Fig. 2.8** shows the simple geometry used to derive the diffraction condition described by Bragg's Law.

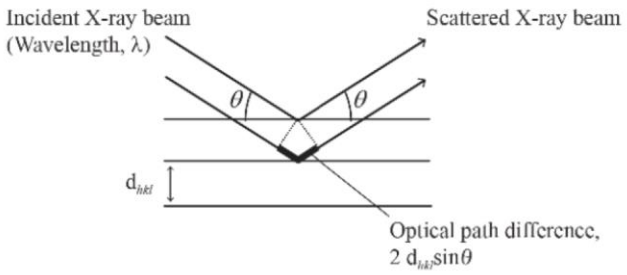

***Fig. 2.8**. A planar illustration of the Bragg x-ray diffraction condition [59]. The horizontal solid lines represent the (hkl) crystal planes in the lattice.*

Compared with powder diffraction measurements, high (angular) resolution XRD (HRXRD) is often used to measure the diffraction peaks from epitaxial films grown on single crystal substrates. The high resolution enables the x-rays to detect the subtle *d*-spacing variations between the epitaxial film and substrate. **Fig. 2.9** presents the HRXRD scan around the (002) peaks from an LSCO film grown on a LSAT substrate. Determined by the perovskite structural

factor and the theta dependence of the atomic scattering factor, the diffraction peak from (002) planes has the highest signal intensity compared to (001), (003) or (004) planes reachable by the Bruker D8 Discover diffractometer.

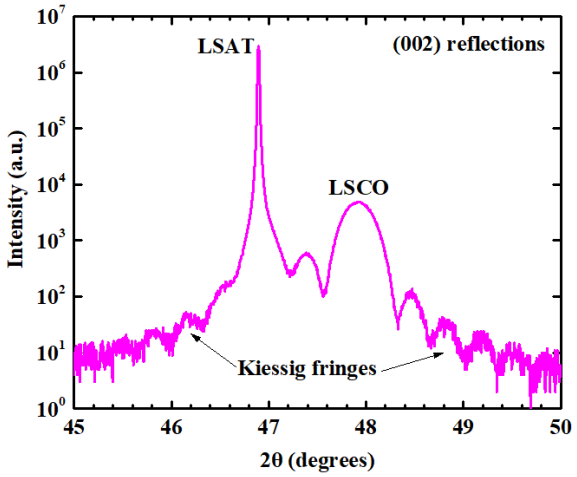

***Fig. 2.9**. HRXRD scan around the (002) peaks from an LSCO film grown on a LSAT substrate.*

As shown in **Fig. 2.9**, the sharp and most intense peak around $2\theta = 47^{o}$ results from diffraction from the substrate (002) planes, while the next most intense peak around $2\theta = 48^{o}$ arises from the (002) diffraction of the LSCO film. The sharp substrate peak indicates that it is in a nice crystalline phase with minimal *d*-spacing variations. Due to finite size effects, the LSCO film peak has much lower intensity and greater width compared to the LSAT substrate peak since the probed volume is much smaller in the film than in the substrate. The out-of-plane lattice parameters of the substrate and the film can be calculated using their corresponding 2θ values and the Bragg equation. The oscillations that extend further below/above the 2θ values of the

substrate/film peaks are the Kiessig thickness fringes, which are only present when there are low interfacial roughness and small *d*-spacing variations across the film. Their periodicity can be used to extract the film thickness. The measurement shown in **Fig. 2.9** is capable of determining the crystalline quality of the film and the substrate and providing their out-of-plane lattice parameters, however, in-plane reflections must be observed to identify whether the film is epitaxial.

The reciprocal lattice is the Fourier transform of the real space lattice, and it is extremely helpful in interpreting diffraction conditions and identifying the crystal structures. Moreover, reciprocal space mapping (RSM) of asymmetric reflections can provide strain state information of the film by charactering both the in-plane and out-of-plane components.

As shown in **Fig. 2.10(a)**, a film grown on a substrate can be fully relaxed with its bulk structure when there is a large crystal structure mismatch between the film and the substrate. In this relaxed case with the cubic symmetry of both layers, the reciprocal lattice points of the film lie on the line from the reciprocal lattice origin to each corresponding substrate point. In the other extreme case, a film can be fully and uniformly strained when the lattice mismatch or the film thickness is small. The in-plane lattice parameter of the film would then match perfectly with that of the substrate, while in the meantime the out-of-plane lattice parameter of the film shrinks

or expands depending on whether the film is undergoing tensile or compressive strain, respectively. The change in the lattice parameters is based on Poisson's effect, indicating the volume of the film does not stay constant when it is strained. The reciprocal lattice points of the film and the substrate are then located on a vertical line along the out-of-plane direction in this strained case. Apart from the two extremes, a partially relaxed film will show a peak in between the vertical line and the line connecting the substrate and the origin reciprocal lattice points.

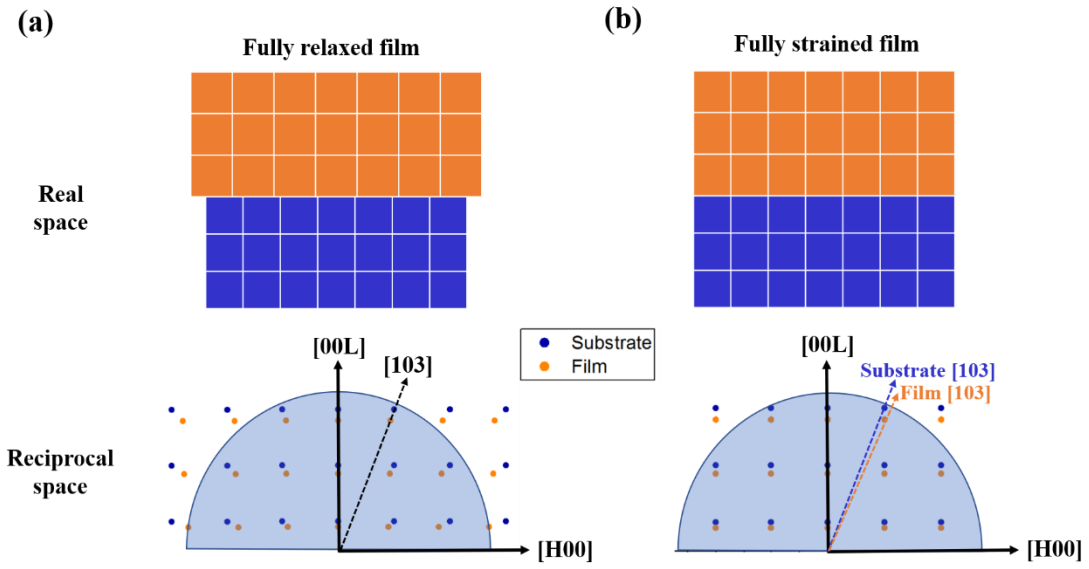

***Fig. 2.10**. Fully (a) relaxed and (b) strained cases of a film grown on top of a substrate, where the lattice parameter of the film is larger than that of the substrate. In both panels, the real space lattice is shown at the top and the reciprocal space lattice is at the bottom.*

As shown in **Fig. 2.11**, a two-dimensional RSM can capture both the substrate and the film reflections. Compared to the substrate, the larger out-of-plane reciprocal lattice unit from the film indicates that the film has a smaller out-of-plane lattice parameter in real space. The film and the substrate reciprocal lattice points lie along a vertical line in the out-of-plane direction, suggesting that the LSCO film is fully strained on the LSAT substrate.

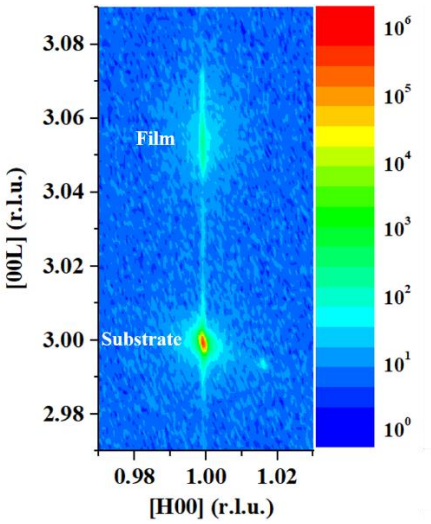

***Fig. 2.11**. RSM of the (103) peaks for an epitaxial LSCO film on a LSAT substrate.*

2.3 Bulk Magnetic Characterization

A superconducting quantum interference device (SQUID) magnetometer is an instrument that is extremely sensitive to magnetic fields and is thus indispensable for magnetic measurements. A schematic for an early version of the instrument is shown in **Fig. 2.12**. The measured magnetization of a SQUID magnetometer arises from the detection coils that include two back-

to-back Josephson junctions, where those junctions are consisted of an insulating material inserted between two superconductors. According to Lenz's Law, an electrical current can be induced in a conductor by changing the magnetic field to oppose the magnetic induction from the sample. In a standard SQUID measurement, the magnetic field around the detection coil changes as a ferromagnetic sample passes through, and the change in magnetic field can induce a current that tunnels between the two Josephson junctions separated by the insulator. This induced current can be precisely converted into a measured voltage which allows the SQUID magnetometer to be capable of detecting magnetic field changes as small as 10^{-15} T [60]. This sensitivity is extraordinarily helpful in quantifying the magnetic properties and measuring the magnetic moments of epitaxial oxide thin films as they typically do not possess large magnetization.

Two standard measurements are typically performed with a SQUID magnetometer, *i.e.*, magnetization *vs.* temperature (*M vs. T*), and magnetization *vs.* magnetic field (also known as magnetic hysteresis loops, *M vs. H*). The *M vs. T* curve is capable of capturing the magnetic transitions of a sample as function of temperature. During the measurement, a small field must be applied to align the ferromagnetic moments. The measured magnetization will encounter an abrupt change at the Curie temperature (T_C), which is typically defined as the maximum of $|dM/dT|$. As a result, the small applied field during an *M vs. T* measurement must be selected

carefully since a large field may yield inaccurate T_C. The other common measurement is the magnetic hysteresis loops, which measure the response of a sample with respect to an applied magnetic field.

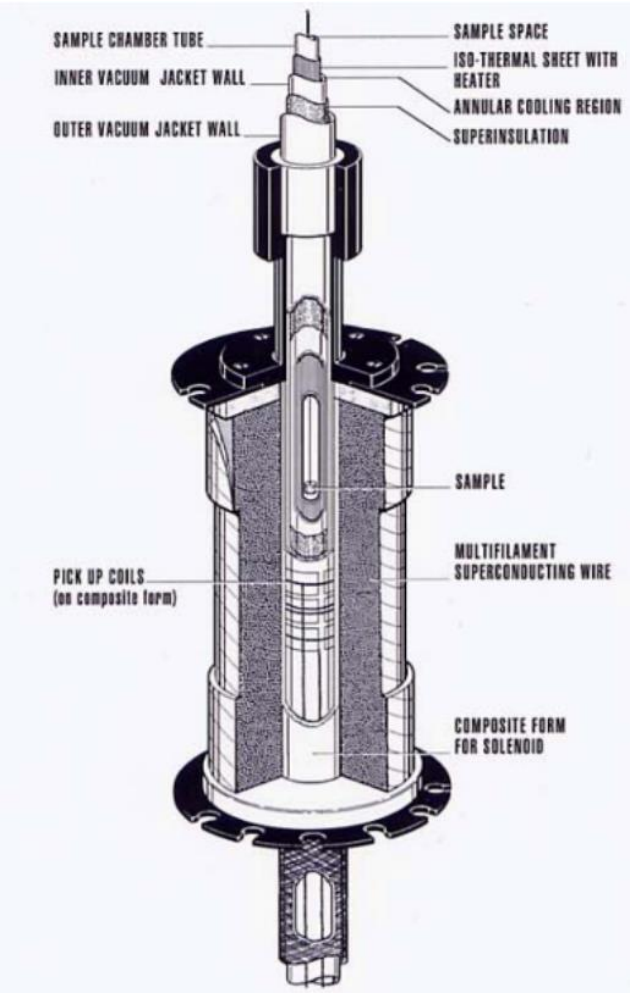

***Fig. 2.12**. A schematic of a SQUID magnetometer from a Quantum Design Magnetic Properties Measurement System [60].*

In terms of SQUID operation, the magnetometer has to be kept under low temperature (*e.g.*, at

liquid helium temperature ~ 4.2 K) as there are superconducting materials included in the system. In the conventional design, chambers are typically equipped with vacuum thermal insulation layers.

2.4 Electrical Transport Characterization

For perovskite oxides, the electrical properties are often linked with their magnetic and structural properties and are thereby highly sensitive to external stimuli such as magnetic fields and temperature. According to Ohm's Law, the sheet resistance of a thin film can be related to its resistivity and film thickness.

$$R = \rho \frac{l}{A} = \rho \frac{l}{wt} = \frac{\rho}{t} \frac{l}{w} = R_S \frac{l}{w} \tag{2.7}$$

where R is the resistance, ρ is the resistivity, l is the length, A is the cross-sectional area. The cross-sectional area is calculated by multiplying the film width (w) by the film thickness (t).

The sheet resistance (R_S) of a film can be related to resistivity by multiplying by the film thickness. Using the van der Pauw method, resistance measurements can be made by applying a voltage across two adjacent contacts (A-D) and measuring the current between the other two contacts (B-C), as shown in **Fig. 2.13**. The calculated resistance can be expressed as follows:

$$R_{AD-BC} = \frac{V_{AD}}{I_{BC}} \tag{2.8}$$

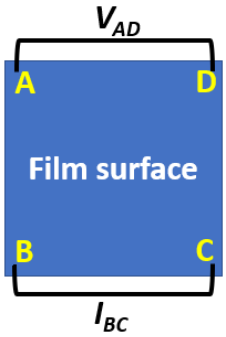

***Fig. 2.13**. Schematic of the van der Pauw measurement.*

Similarly, $R_{AB\text{-}DC}$ can also be measured. Accurate values can be obtained using **Eqn. 2.9** by taking the average of the resistance across the two edges.

$$R_1 = \frac{R_{AD-BC} + R_{BC-AD}}{2} \quad , \quad R_2 = \frac{R_{AB-DC} + R_{DC-AB}}{2} \tag{2.9}$$

Finally, the van der Pauw formula can be used to determine the sheet resistance R_S:

$$e^{-\pi \frac{R1}{Rs}} + e^{-\pi \frac{R2}{Rs}} = 1 \tag{2.10}$$

2.5 Soft X-Ray Absorption Spectroscopy

X-ray absorption (XA) describes the phenomenon of electrons being excited from the core levels to the valence state. The electrons in the inner shell can absorb the incoming x-rays or

photoelectrons and be promoted to an excited state above the Fermi level (**Fig. 2.14(a)**). An electron hole is then created in the inner shell, and an outer-shell electron will drop down to fill that hole. To obey the energy conservation, the energy difference between the outer and inner shell (**Fig. 2.15**) will then be emitted in the form of a characteristic x-ray or Auger electrons. The Auger electron is created by ejecting another electron out of the atom using the excess energy between the outer and inner shell. Furthermore, the cascade process of the Auger decay electrons can produce the secondary electrons.

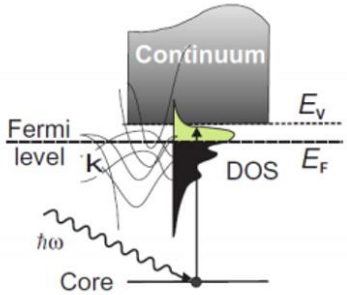

***Fig. 2.14**. Illustration of a core electron being excited by an x-ray and then reaching the state above the Fermi level [61].*

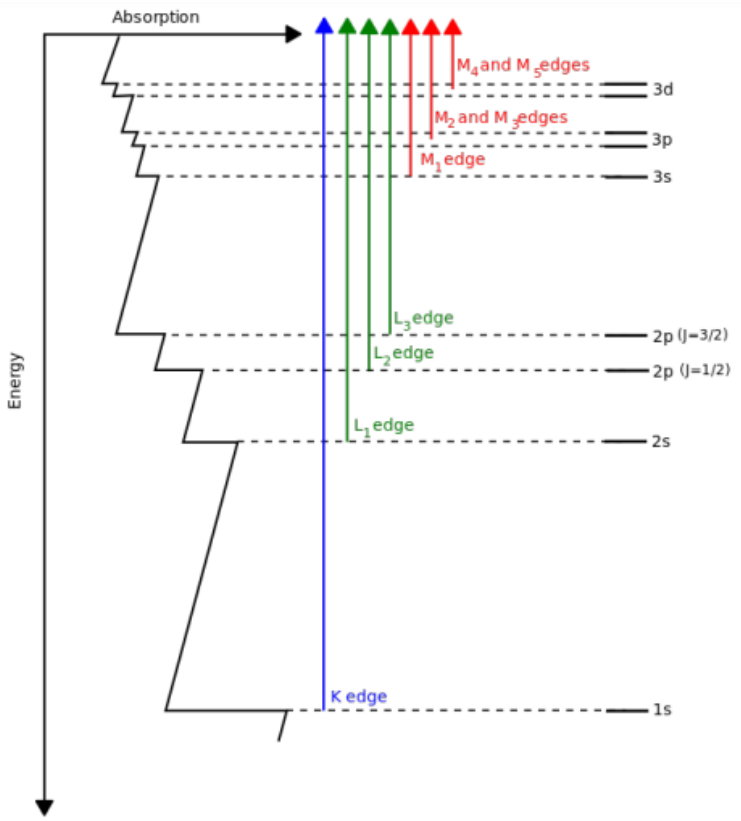

***Fig. 2.15**. The electronic transitions within different orbitals in transition metals [65].*

The total electron yield (TEY) mode, which is the detection of the neutralization current needed to replenish the emitted Auger and secondary electrons, provides the surface sensitivity to the top ~ 5–10 nm [62] of the sample due to the short mean free path of electrons. To probe the full film thickness, the luminescence yield (LY) detection mode measures visible light photons converted from the incident x-rays by the luminescent substrate [63]. As shown in **Fig. 2.14(b)**, the absorption intensity of an XA spectra is determined by the atomic cross-section in addition to the density of states above the Fermi level [61].

For the first-row transition metals, the *L*-edge electron transition from the *2p* core orbitals to the unfilled *3d* states above the Fermi level requires soft x-rays with energies between 400–1000 eV [64]. Synchrotron radiation with an intense source of photons is often involved in the generation of soft x-rays with tunable energies. By varying the photon energy to the absorption edge of a specific element, the XA spectrum can provide the detailed information of the local electronic structure, bonding environment, and valence states for that certain element in individual layers. **Fig. 2.15** shows the different absorption edges within a transition metal.

For magnetic materials, the polarization of x-rays can affect the spectral shape of their XA spectra (known as dichroism) and can thus be used to determine their magnetic properties. Two types of dichroism are discussed below, x-ray magnetic circular dichroism (XMCD) and x-ray magnetic linear dichroism (XMLD).

2.5.1 X-Ray Magnetic Circular Dichroism

For perovskite oxides with the first-row transition metals on the *B*-site, the magnetic properties are determined by the *3d* band structure. In a ferromagnetic material, the exchange energy shifts the relative energy bands of the spin-up and spin-down electrons so their density of states and orbital filling at the Fermi level are unbalanced, as shown in **Fig. 2.16(a)** for metallic Co. Since the photon absorption from circularly polarized x-rays follows conservation of angular

momentum and prohibits spin flip of electrons, the number of electrons excited from the core level to the empty states above the Fermi level will be unequal depending on whether a right or left circularly polarized x-ray is used.

As shown in **Fig. 2.16(b)**, XMCD is defined as the difference between two XA spectra acquired using right/left circular polarizations (RCP/LCP). During the measurement, an applied field is necessary to saturate the sample to prevent the case of zero net dichroism due to multiple magnetic domains with opposite spin directions. Alternatively, XMCD can also be calculated as the difference between spectra captured with opposite applied magnetic field. Ideally, this applied magnetic field saturates the magnetization of the sample. In this measurement setting, the circular polarization is fixed at a certain direction, either RCP or LCP. The XMCD effect originates from the parallel spin alignment in a ferromagnetic material [61], and its magnitude can reflect the net ferromagnetic moments presented in a sample. In addition, the spectral line shape of XMCD can provide complementary information of the corresponding magnetically active ion.

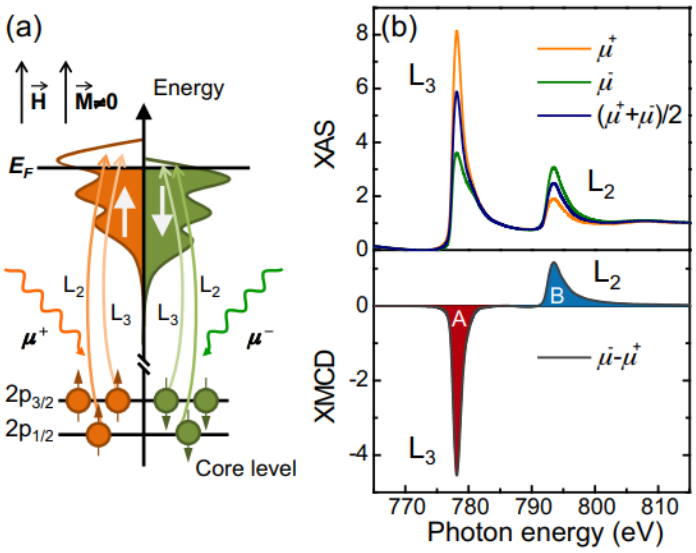

***Fig. 2.16**. (a) Schematic diagram of the relative energy levels and the x-ray photon absorption with RCP and LCP in Co metal. (b) The XA spectra at the Co-edge taken with right (μ^+, orange) and left (μ^-, green) circular polarization (top) and the difference between the two XA spectra, XMCD (bottom) [66].*

2.5.2 X-Ray Magnetic Linear Dichroism

XMLD spectroscopy [67] and neutron diffraction are two of the few techniques capable of probing antiferromagnetic ordering in a material. However, the low flux and high penetration of neutron sources prevent them from probing thin films as their film volume is too low. Alternatively, an x-ray beam with linear polarization can probe the elongation and non-spherical distortion of the charge density around the nucleus along the antiferromagnetic spin axis. As shown in **Fig. 2.17**, the absorption varies depending on whether the linear polarization vector (*E*-vector) of the x-ray is parallel (*p*-polarized) or perpendicular (*s*-polarized) to the

plane of incidence. In general, XMLD spectra are sensitive to any asymmetry in a sample such as crystal-field effects, ferromagnetic anisotropy, orbital ordering ($d_{x^2-y^2}$ *vs.* d_{z^2} orbitals), and the electronic distribution around the antiferromagnetic moments [68,69]. Therefore, careful design of the experimental geometry is needed to identify the true source(s) of the dichroism. In order to only probe the antiferromagnetic asymmetries, the two polarization vectors can be chosen along equivalent crystallographic directions where one is aligned along the AFM spin axis and the other is perpendicular.

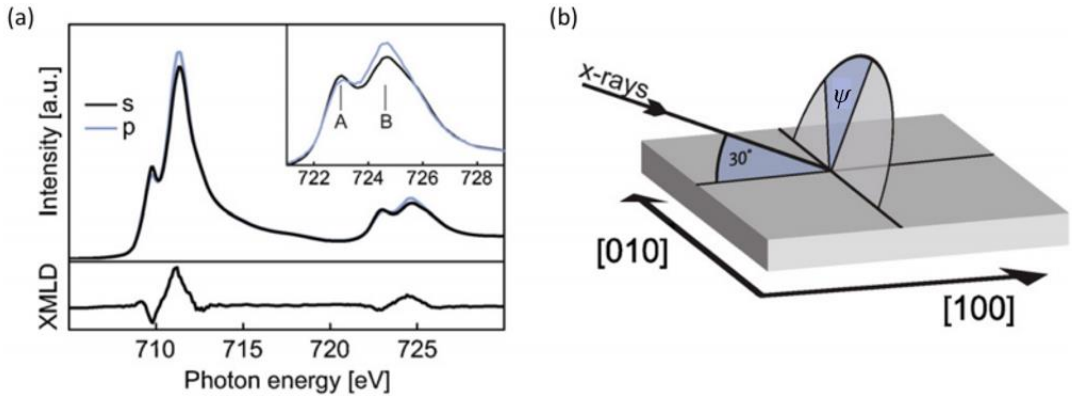

Fig. 2.17*. (a) XA spectra of $LaFeO_3$ taken with s- and p- linearly polarized x-rays and the corresponding XMLD spectrum. (b) The geometry of an XMLD experiment. The angle ψ can be any angles between 0° (p-polarized x-rays) and 90° (s-polarized x-rays) [70].*

2.6 X-Ray Photoemission Electron Microscopy

With the aid of XA/XMCD/XMLD spectroscopy measurements, x-ray photoemission electron

microscopy (X-PEEM) has the ability to image magnetic domains. Similar to TEY detection mode in an XA spectrum, the signals collected in X-PEEM are directly related to the photoemitted electrons from the sample surface; however, in X-PEEM these electrons are then collected by a charge-coupled device (CCD) camera through an electron microscope column to produce the domain images [71], as shown in **Fig. 2.18**. In the measurement, it is crucial to ensure that the emitted secondary electrons travel into the optics positioned directly above. Therefore, a large negative voltage (~ 15-20 kV) is typically maintained on the sample surface and the image intensity benefits from a conductive sample. The spatial resolution of the x-ray absorption intensity in an X-PEEM microscope is limited by the energy distribution of the emitted photoelectrons through chromatic aberration.

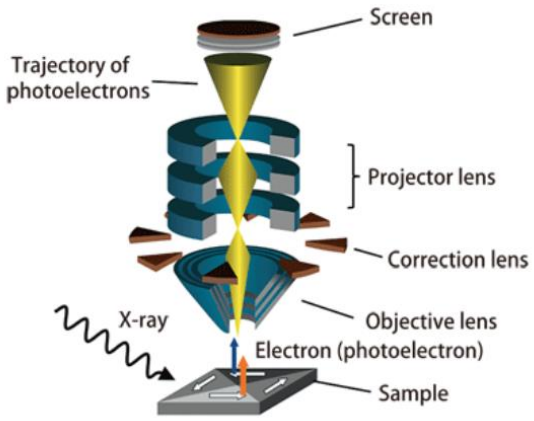

***Fig. 2.18**. Schematic of an X-PEEM microscope [72].*

To image ferromagnetic domains, the x-ray photon energy is tuned to the energy corresponding

to the maximum XMCD signal in the XA/XMCD spectroscopy measurements. The XMCD-PEEM images can then be obtained using RCP and LCP x-ray beams. To remove topographic contributions and work function differences from the domain images [61], an asymmetry calculation is performed between the RCP/LCP collected images, $I_{FM} = (I_{RCP} - I_{LCP})/(I_{RCP} + I_{LCP})$. The calculated images solely reflect the magnetic domain contrast, where their intensity has a cosine dependence to the angle between the incident x-ray helicity vector and the local magnetic moments. The intensity contrast is also proportional to the magnitude of the magnetization.

For imaging antiferromagnetic domains in the oxides discussed in the following chapters, the linear polarization angle of the x-ray beam is first tuned to a specific angle (*i.e.*, *E*-vector of the x-ray is fixed), and the XMLD-PEEM images can then be acquired at the photon energies corresponding to the negative and positive features of the L_2 XMLD spectra. The similar asymmetry equation is performed for the two photon energies to enhance the magnetic contrast, $I_{AFM} = (I_{L_2^+} - I_{L_2^-})/(I_{L_2^+} + I_{L_2^-})$. The images taken with a full polarization series rotating from *p*- to *s*-polarized x-rays are necessary to identify the orientation of the spin axis in antiferromagnetic domains, as the intensity contrast of XMLD follows the cosine-squared dependence of the angle between the *E*-vector and the antiferromagnetic spin axis. Shown in **Fig. 2.19** are the XMCD- and XMLD- PEEM images from an $Nd_{0.5}Sr_{0.5}MnO_3$ thin film grown

on a $SrTiO_3$ substrate.

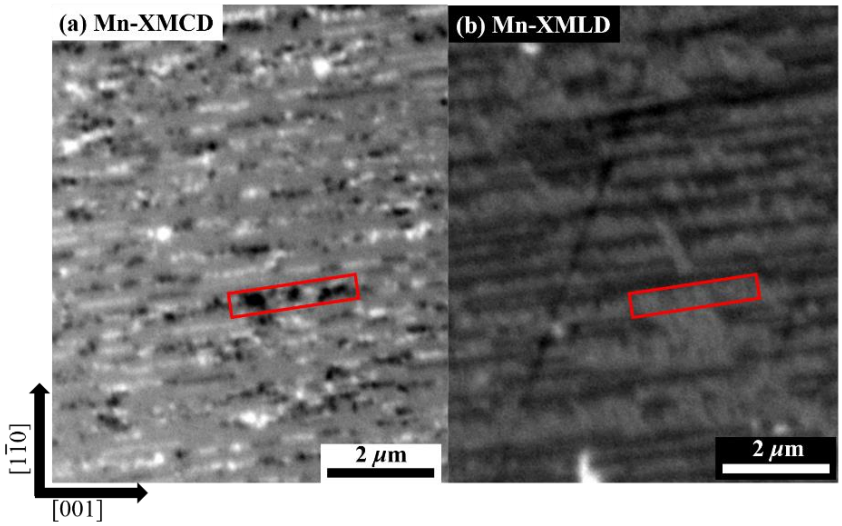

***Fig. 2.19**. Mn (a) XMCD- and (b) XMLD- PEEM images taken from the same location. The red rectangle highlights a region with small FM domains which correlates to a gray region in the XMLD-PEEM image.*

2.7 Conclusion

This chapter is a summary of the thin film synthesis and characterization techniques that were used in this work. Sample synthesis was performed via a PLD growth system. Structural quality of the films was characterized by x-ray diffraction experiments to determine the thickness, roughness, density, and lattice parameters of the thin films. Electrical transport behavior was studied using a Lakeshore low temperature probe station. The bulk magnetic properties were measured using a Quantum Design VersaLab VSM or SQUID magnetometer. Soft x-ray

magnetic spectroscopy measured at the Advanced Light Source of Lawrence Berkeley National Laboratory provides element-specific electronic/magnetic information for the oxide films.

Chapter 3 : Phase Transitions and Magnetic Domain Coexistence in $Nd_{0.5}Sr_{0.5}MnO_3$ Thin Films

3.1 Introduction

In order to maintain the current pace of innovation in memory and logic devices, novel classes of materials and alternative device designs are imperative for further breakthroughs [1]. Among the candidate materials, complex metal oxides (CMOs) are promising due to their diverse functional properties such as colossal magnetoresistance, abrupt metal-to-insulator transitions, and a high degree of spin polarization at the Fermi level [2-9]. Within the family of CMOs, perovskite oxides with the chemical formula ABO_3 have received a great deal of interest because of the wide range of functional properties which can be controlled through chemical substitutions on the A and B sites, as well as the oxygen stoichiometry [12-15]. In addition, modern thin film synthesis techniques have enabled fine control of structural parameters such as the epitaxial strain state, strain symmetry, and film thickness such that artificial composite materials with emergent functional properties at interfaces can be investigated [73-75].

For example, the hole-doped manganite $Nd_{1-x}Sr_xMnO_3$ displays a rich phase diagram of different magnetic and electronic phases depending on the Sr doping level (**Fig. 1.7**). For a small range of compositions from $0.48 < x < 0.51$ for $Nd_{0.5}Sr_{0.5}MnO_3$ (NSMO), two coupled magnetic and electronic transitions are observed as a function of temperature, involving a first

transition upon cooling from the paramagnetic (PM)/insulating phase to a ferromagnetic (FM)/metallic phase at ~197 K, followed by a transition to an antiferromagnetic (AFM)/charge-ordered insulating phase at ~150 K [34]. Over a range of applied magnetic field and temperatures, first order phase transitions can lead to coexistence of the FM and AFM phases [76-78]. Recent studies show that this magnetic phase coexistence can lead to large magnetoresistance effects which can be applied in hard disk drives and magnetoresistive spintronic device applications [79-83].

In NSMO thin films, it has been reported that stabilizing the AFM/insulator phase requires an anisotropic strain state to support Jahn-Teller (JT) distortions of the MnO_6 octahedra and the structural freedom to drive the Mn^{3+} ions into the charge-ordered phase [35,36,84]. Such an anisotropic strain state can be achieved using (110)-oriented substrates such that the *a*- and *b*-axes of the pseudocubic (pc) unit cell are canted 45° out of the (110) surface plane, creating some freedom for the BO_6 octahedral bond directions to distort at temperatures below the Néel temperature (T_N). This substrate orientation presents a rectangular growth surface where the two low-index in-plane directions are the [001] and [$1\bar{1}0$] cubic substrate directions. Bulk NSMO has orthorhombic symmetry with lattice parameters of a = 0.543 nm, b = 0.548 nm, and c = 0.764 nm at room temperature, corresponding to a pseudo-cubic lattice parameter a_{pc} = 0.3840 nm [34,85]. On (110)-oriented $SrTiO_3$ (STO) substrates with cubic symmetry and

a = 3.905 Å, the lattice mismatch between STO and the NSMO film is 0.86% in the [001] substrate direction and 2.23% in [1$\bar{1}$0] substrate direction, which are expected to result in fully strained and partially relaxed strain states, respectively [36]. In contrast, when NSMO films are grown on (001)-oriented substrates where the a- and b-axes of the pseudocubic unit cell are clamped to the substrate, only the FM/metallic phase is observed down to low temperatures [35,36]. Furthermore, prior studies have shown that stabilizing the AFM/insulator phase in NSMO thin films strongly depends on the preparation method or growth conditions, such as the strain induced by the substrate, or the substrate temperature and oxygen pressure during pulsed laser deposition (PLD) [35,36,84,86-88].

In this chapter, a study of the physical properties of NSMO thin films grown on (110)-oriented STO substrates is presented. STO was chosen to minimize the lattice mismatch between the film and the substrate. Resonant x-ray reflectivity (RXRR) and bulk magnetization measurements showed that vertically the NSMO film consists of three layers which differ in terms of their density and magnetic properties. Polarized soft x-ray magnetic spectroscopy, exploiting the x-ray magnetic circular/linear dichroism (XMCD/XMLD) effects, were performed to directly probe both the FM and AFM characteristics, respectively, and to confirm the occurrence of the FM-AFM transition. X-ray photoemission electron microscopy (X-PEEM) was used to image the FM and AFM domains and to demonstrate the lateral

coexistence of FM and AFM domains at 110 K, as expected for a first order phase transition. These characterization techniques demonstrate the multiple magnetic and electronic phase transitions in the NSMO films, and thus the possibility and diversity of functional properties to be applied in next generation devices.

3.2 Experimental Methods

Epitaxial NSMO thin films were deposited on (110)-oriented STO substrates by PLD with a laser pulse frequency of 5 Hz and laser fluence of ~1.5 J cm^{-2}. During the growth, the substrate temperature was held at 750 ºC and the oxygen background pressure was 160 mTorr. The films were cooled slowly to room temperature after the deposition with an oxygen pressure of 100 Torr to ensure proper oxygen stoichiometry. The structural properties of the films were characterized by high-resolution x-ray diffraction (XRD) using a Bruker D8 DISCOVER four-circle diffractometer using Cu $K_{\alpha 1}$ x-rays. RXRR spectra were obtained at Beamline 2-1 at the Stanford Synchrotron Radiation Lightsource using an x-ray energy near the Mn *K* edge (6552 eV). This K-edge absorption energy was obtained by performing the Kramers-Kronig transformation to the x-ray absorption near edge structure energy spectra, where the real part of the x-ray dispersion correction factor, *f'*, is at a minimum. XRR spectra taken at resonant energies provide increased sensitivity to the chemical contrast between thin films and substrates which have similar density [57]. By simulating the RXRR spectra in the GenX

reflectivity simulation software [89], the thickness, roughness, and density values of the films were modeled. A Lakeshore probe station was used to measure the film resistivity upon warming from 80 K with the van der Pauw geometry. The bulk magnetic properties with the magnetic field applied along the in-plane [001] substrate direction was measured using a VersaLab Physical Properties Measurement System from Quantum Design.

Soft x-ray magnetic spectroscopy at the Mn *L*-edge was performed at 80 K and 160 K at beamlines 4.0.2 and 6.3.1 at the Advanced Light Source (ALS) using the total electron yield (TEY) detection mode. For the XMCD measurements, the x-rays were incident upon the sample at a 30° grazing angle along the [001] substrate directions, and the magnetic field was applied parallel to the x-rays. The dichroism was calculated as the difference between spectra captured with applied magnetic field ± 1.4 T; this field was chosen so the film can reach saturation magnetization. The x-ray linear dichroism (XLD) spectra were acquired with an x-ray incidence angle of 45 ° along the $[1\bar{1}0]$ substrate directions using *s*- and *p*-polarized x-rays so that the ***E***-vector was oriented parallel to the [001] and [100] substrate directions, respectively. The XLD spectra were calculated as the difference of the XA spectra obtained with the two linear polarizations. The X-PEEM images were acquired using the PEEM3 microscope at Beamline 11.0.1 at the ALS [90], with the x-ray beam incident along the [001] substrate direction at a 30 ° grazing incidence angle. XMCD-PEEM images were obtained

using right/left circularly polarized (RCP/LCP) x-rays at the photon energy corresponding to the maximum XMCD signal at the Mn L_3 edge. XLD-PEEM images were acquired at the photon energies corresponding to the negative and positive features of the Mn L_2 XLD spectra with the polarization rotating from *p*- to *s*-polarized x-rays. In all cases, the domain images were obtained using an asymmetry equation, $I = (I_{RCP} - I_{LCP})/(I_{RCP} + I_{LCP})$, to remove topographic contributions and work function differences from the domain images.

3.3 Results and Discussion

RXRR and XRD ω-2θ scans (**Fig. 3.1**) display a well-defined film peak and Kiessig fringes indicative of a highly crystalline film with smooth interfaces. From the XRD data, a_{pc}(NSMO) is determined to be 0.3825 nm, consistent with a film under substrate-induced tensile strain. The periodicity of the Kiessig fringes in the RXRR spectrum (**Fig. 3.1(a)**) corresponds to a total film thickness of 16.5 nm, however, an envelope of a longer period oscillation indicates that the NSMO film is best represented as three layers which differ by their density due to changes in their composition, electronic properties, and/or optical constants. **Table 3.1** lists the full structural characteristics of these three layers. Similar three-layer models have been used for other oxide thin films [86,91]. Due to the exposure of the samples to atmosphere between deposition and x-ray measurements, a thin surface carbon-containing layer was added to refine the simulation [92]. The error bars were determined by the range that produces a ± 5% change

in the figure of merit (FOM, a quantity used to characterize the performance of the fitting results). The lower density in the layer at the NSMO/STO interface may result from the tensile strain induced by the STO substrate, while the thin surface layer may be slightly oxygen or cation deficient [91,93,94]. The main NSMO layer (thickness ~14.7 nm) has the same density as bulk NSMO and is sandwiched between the surface and interface layers. Compared to simpler two-layer models with only the surface and the main layer, or the main and substrate interface layers (see **Fig. 3.2**, **Tables 3.2 and 3.3**), the logarithmic FOM of the three-layer model is decreased by 59% and 46%, respectively (FOM = 0.05378). The surface and interface layers are not detectable in the ω-2θ scan due to their small thickness (< 1 nm).

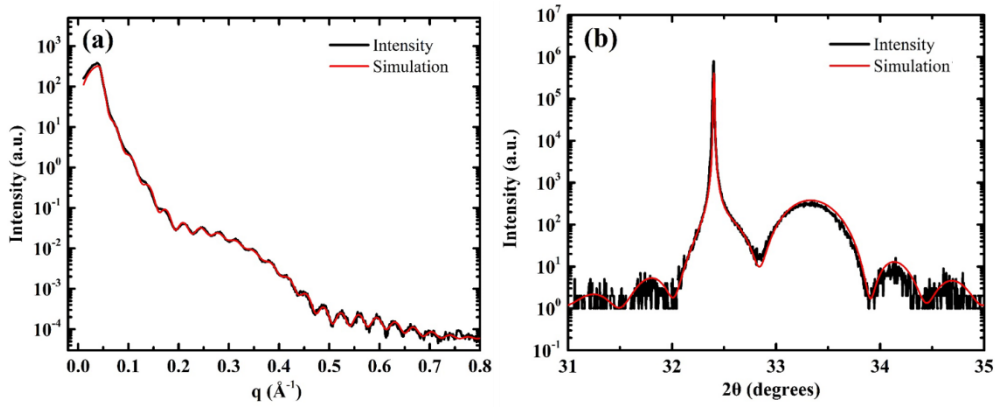

Fig. 3.1*. (a) RXRR spectrum and (b) XRD ω-2θ scan around the substrate (110) peak for an NSMO film on (110)-oriented STO substrate. Black and red curves are the raw data and simulations, respectively.*

Table 3.1. *Optimized fit parameters for RXRR spectra*

	Thickness (nm)	Roughness (nm)	Density (g cm^{-3})
Carbon layer	1.00 ± 0.32	0.31 ± 0.03	2.36 ± 0.06
NSMO_surface	0.84 ± 0.01	0.80 ± 0.10	6.30 ± 0.04
NSMO_main	14.74 ± 0.11	0.57 ± 0.04	6.40 ± 0.03
NSMO_interface	0.93 ± 0.02	0.66 ± 0.05	6.32 ± 0.02
STO substrate	–	0.27 ± 0.02	5.12 ± 0.00

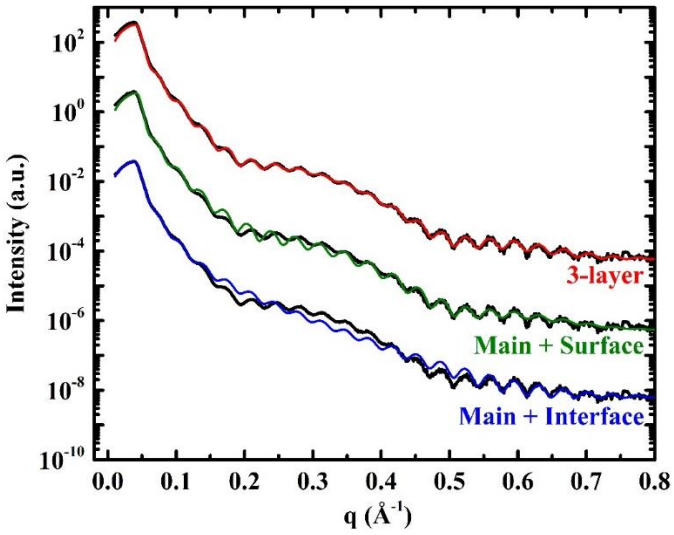

Fig. 3.2. *Fitting results of the three-layer (red) and the two-layer models. The two-layer model with only the surface and main layers are denoted in green, while that with only the interface and main layers are presented in blue. Due to the exposure of the samples to atmosphere between deposition and x-ray measurements, a thin surface carbon-containing layer was added to refine the simulation [92]. The black curves are experimental data, and the colored curves are simulation results. The envelope of a longer period oscillation (prominent between* ***q*** *= 0.2~0.5 Å^{-1}), indicates that the film has at least two layers, one of which is much thinner than the main layer. Compared to a three-layer model, the logarithmic FOM of the two-layer*

model with only the surface and the main layer increased by 59% (FOM = 0.08551), while the logarithmic FOM of the two-layer model with only the interface and the main layer increased by 46% (FOM = 0.07851).

Table 3.2. *Two-layer sample model (Main + surface layers)*

	Thickness (nm)	Roughness (nm)	Density (g cm^{-3})
Carbon layer	1.00 ± 0.09	0.31 ± 0.01	2.74 ± 0.09
NSMO_surface	0.80 ± 0.06	0.83 ± 0.09	6.30 ± 0.06
NSMO_main	15.63 ± 0.56	0.23 ± 0.02	6.37 ± 0.01
STO substrate	–	0.30 ± 0.09	5.12 ± 0.00

Table 3.3. *Two-layer sample model (Main + interface layers)*

	Thickness (nm)	Roughness (nm)	Density (g cm^{-3})
Carbon layer	1.00 ± 0.09	0.32 ± 0.02	2.64 ± 0.09
NSMO_main	15.87 ± 0.59	1.31 ± 0.87	6.38 ± 0.06
NSMO_interface	0.68 ± 0.24	0.30 ± 0.00	6.36 ± 0.04
STO substrate	–	0.08 ± 0.02	5.12 ± 0.00

Reciprocal space maps (RSMs) taken around the asymmetric (222) and (310) peaks for the STO substrate are shown in **Fig. 3.3**. As discussed earlier, it has been postulated that the asymmetric strain state of NSMO thin films grown on (110)-oriented STO substrates [35,36] facilitates the observation of the FM-AFM transition. According to this theory, the films need to be strained to the substrate in the in-plane [001] direction (corresponding to the (222) peak)

and partially relaxed in the in-plane [1$\bar{1}$0] direction (corresponding to the (310) peak). As shown in **Fig. 3.3**, the NSMO film adopts this epitaxial strain state, as the weak film peak is shifted to higher values of reciprocal space compared to the substrate peak in the (310) RSM, while the two peaks are exactly vertically aligned in the (222) RSM.

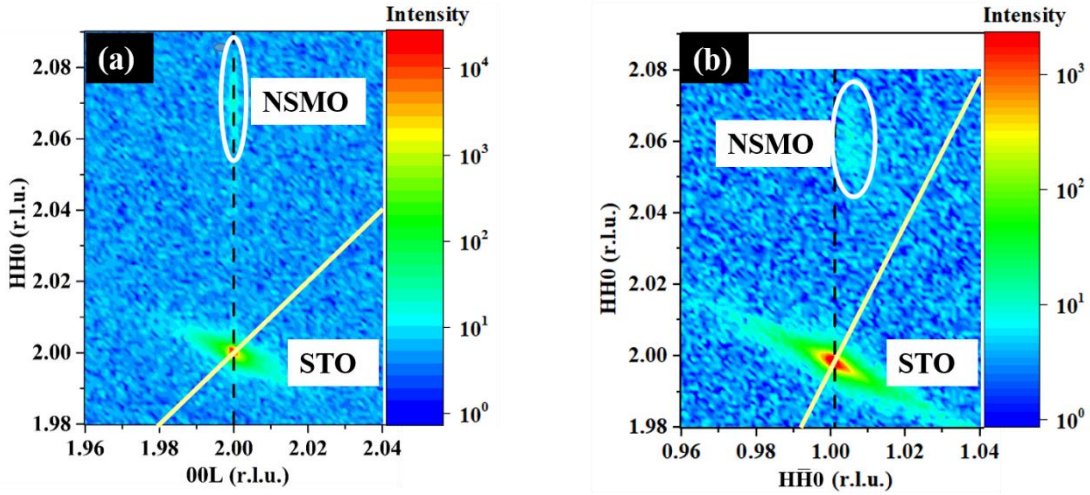

***Fig. 3.3**. RSMs around the (a) (222) peak and (b) (310) substrate peak for an NSMO film on (110)-oriented STO substrate. The dashed vertical line represents a fully-strained film while solid yellow line represents a fully-relaxed film. The circle denotes the location of the film peaks. The film is fully strained in the in-plane [001] direction while partially relaxed in the in-plane [1$\bar{1}$0] direction.*

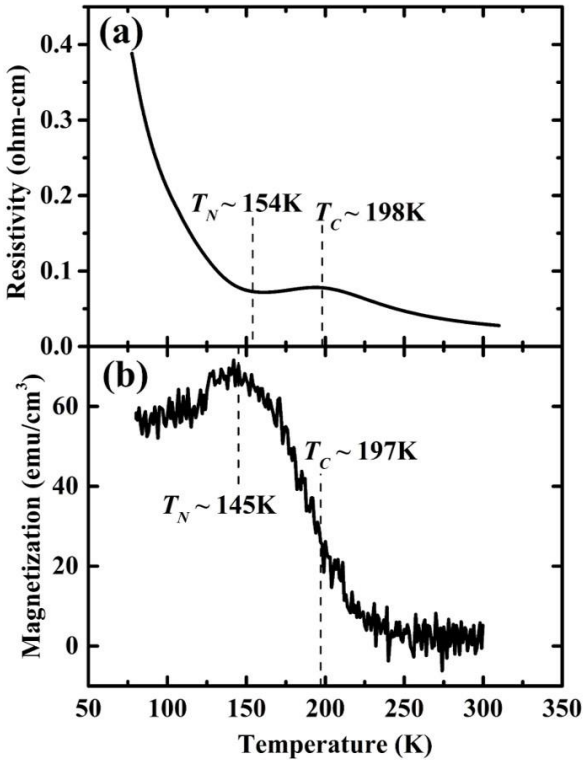

***Fig. 3.4**. (a) Film-averaged resistivity and (b) magnetization as a function of temperature, measured along the [001] substrate direction. A magnetic field of 0.06 T was applied during the magnetization measurement.*

The bulk magnetic properties of the NSMO thin films were probed using resistivity and magnetization measurements as shown in **Fig. 3.4**. These values are normalized to the film volume using the surface area and the total film thickness (16.5 nm) obtained in the RXRR fitting. Upon cooling, the film undergoes two electrical and magnetic phase transitions, *i.e.*, PM/insulator to FM/metal transition at Curie temperature (T_C) ~ 197 K and the FM/metal to AFM/insulator transition at T_N ~ 150 K. In the resistivity measurement, T_C and T_N were determined as the temperature where the curve is a local maximum and minimum, respectively

[95-97]. In the magnetization plot, the transition temperatures were determined as the temperatures where *dM/dT* has the largest magnitude [98]. Using these metrics, the transition temperatures are in good agreement between the two measurements. In the temperature region below T_N, the resistivity exponentially increases with decreasing temperature as expected for an insulating film, however, the magnetization gradually decreases but does not completely drop to zero as would be expected for an AFM phase. This result suggests that instead of displaying complete AFM ordering, the transition at T_N may be associated with a gradual growth of AFM domains with the presence of shrinking FM domains. As the AFM domains grow, they form a percolated network such that they dominate the resistivity measurements leaving small isolated FM domains.

Mn-XMCD measurements provide element specific and surface sensitive magnetic characterization of the NSMO films (**Fig. 3.5(a)-(c)**). The TEY detection mode provides surface sensitivity to the top ~5–10 nm of the sample [99] and therefore probes only the main and surface NSMO layers. The Mn-XMCD spectra confirm FM behavior above and below T_N, however, the magnetic signal is smaller in magnitude at 80 K compared to 160 K, consistent with the formation of AFM domains below T_N. **Fig 3.5(c)** and **3.5(d)** compare the magnetic hysteresis loops acquired by XMCD and bulk magnetometry, respectively at 80 K and 160 K. In both cases, the magnetic field was applied along the [001] substrate direction and the

diamagnetic signal from the STO substrate was subtracted from the bulk magnetometry measurements. The magnetic moment for bulk NSMO is reported to be ~195 emu/cm^3, or 1.18 μ_B/Mn [100,101]; however, the saturation magnetization of the NSMO thin film in **Fig. 3.5(d)** is ~135 emu/cm^3 (or 0.82 μ_B/Mn). This difference suggests that the FM/metallic phase and other insulating phases with lower or no net magnetization coexist at the measurement temperatures. In **Fig. 3.5(d)** a single magnetic transition is observed at 160 K, while two magnetic transitions are observed at 80 K. This magnetic behavior is consistent with the RXRR fitting that shows that the NSMO film consists of three distinct layers, where this low temperature magnetic phase may correspond with the thin, fully strained layer at the STO substrate interface [102-104]. In contrast, the XMCD hysteresis loops (**Fig. 3.5(c)**) display only a single magnetic transition at both temperatures with coercivity values which correspond well with those from the bulk hysteresis loops. Therefore, a model was proposed where the surface NSMO layer corresponds to a non-magnetic layer commonly observed in many perovskite oxide thin films [83,102-104], the main NSMO layer displays both the PM/FM and FM/AFM transitions, while the fully strained layer at the substrate interface displays only a PM/FM transition with a reduced T_C.

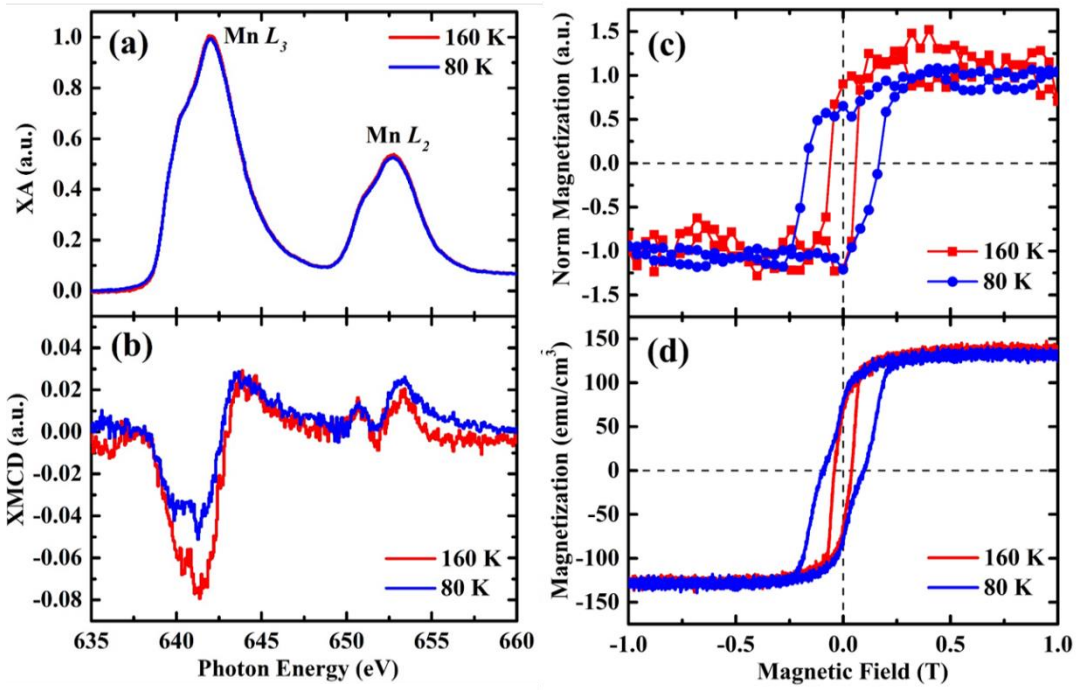

Fig. 3.5*. Mn (a) XA and (b) XMCD spectra taken at 80 K and 160 K with 1.4 T magnetic field in the [001] substrate direction. (c) Mn-XMCD and (d) bulk magnetic hysteresis loops taken at 80 K and 160 K with the magnetic field applied in the [001]-direction.*

XLD spectroscopy [67] is one of the few techniques capable of probing AFM order in thin films. In general, XLD spectra are sensitive to any asymmetry in a sample such as crystal-field effects, ferromagnetic anisotropy, orbital ordering, and the charge distribution around AFM moments [68,69]. Therefore, careful design of the experimental geometry is needed to identify the true source(s) of the dichroism. The measurement geometry for the NSMO thin films on (110)-oriented STO substrates is shown in **Fig. 3.6(a)**. With a 45° incidence angle relative to the sample surface, the *s*- and *p*-polarized x-rays probe the [001] and [100] substrate directions,

respectively, the latter of which is aligned with the JT distortions which occur to induce the FM-AFM transition. The dichroism is calculated as the difference of the XA spectra obtained from those two directions and shown as a function of temperature in **Fig. 3.6(b)**. A pronounced XLD signal is observed at 80 K (blue curve), and while it decreases in magnitude with increasing temperature, it does not completely disappear at 300 K (red curve). This residual XLD signal likely results from the structural asymmetry of the strained film as it possesses a different line shape compared to the low temperature curves [105-107]. By subtracting the 300 K signal from the 80 K and 160 K curves, the pure AFM XLD spectra was obtained at each temperature (brown and green curves). These two subtracted curves maintain the same spectral shape and only differ in their magnitude, indicating that they have the same origin, *i.e.*, the AFM properties. The XLD intensity of the subtracted curve at 160 K only retains 30% compared to the subtracted curve at 80 K. The fact that the XLD signal does not completely vanish at 160 K, supports the persistence of some AFM domains at this elevated temperature.

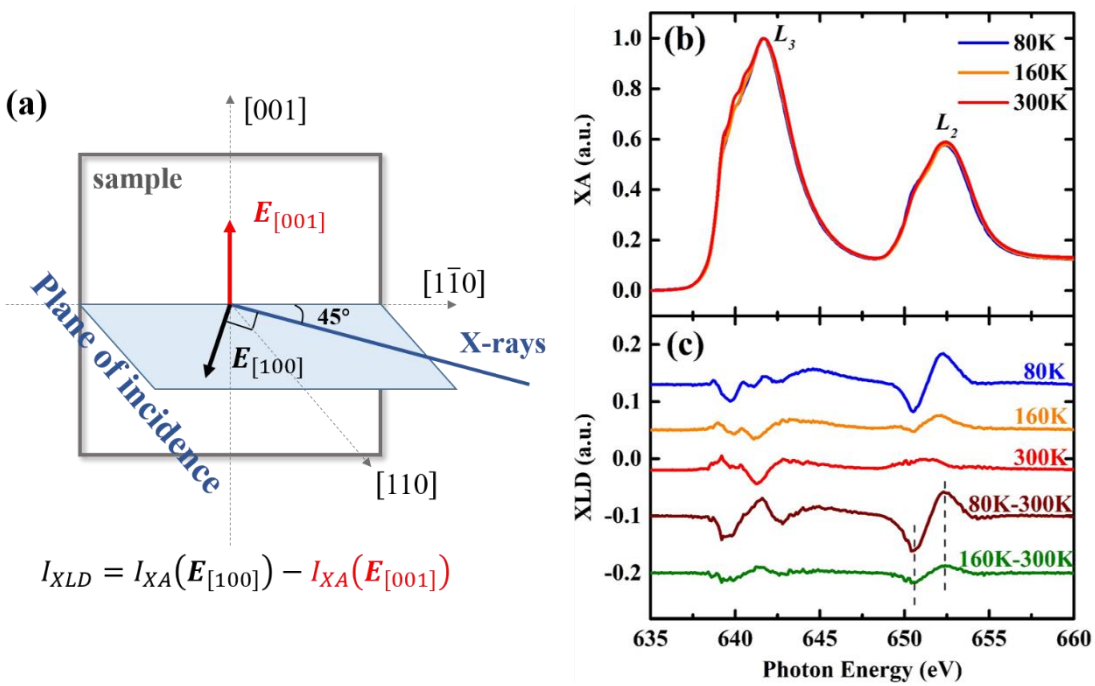

***Fig. 3.6**. (a) XLD measurement geometry and Mn (b) XA and (c) XLD spectra taken at 80 K, 160 K, and 300 K. The brown and green curves were obtained by subtracting the 300 K signal from the 80 K and 160 K curves, respectively, in order to show the pure AFM XLD spectrum at each temperature.*

In order to investigate the coexistence of the FM and AFM domains at low temperature, XMCD- and XLD-PEEM images were acquired from the same location (**Fig. 3.7**) with the incident x-rays oriented along the [001] substrate direction. The sample orientation in the PEEM3 microscope agrees with the XMCD spectroscopy measurements (**Fig. 3.5**), but because of the fixed incidence angle (30°) of the instrument, the geometry must differ from the XLD spectroscopy measurements (**Fig. 3.6**). The local contrast of an XMCD image follows a

cosine dependence between the local magnetization vector and the propagation direction of the incident x-rays. Domains that are aligned parallel/antiparallel to the incident x-ray direction appear with strong white/black contrast. From **Fig. 3.7(a)**, small FM domains (black/white regions) are aligned horizontally in long stripes, separated by long stripes with grey contrast. The approximate size of the FM domains is 0.5-1 μm. The gray regions can either be domains with magnetization oriented perpendicular to the x-ray incidence direction or non-FM regions.

XLD-PEEM images are used to clarify the nature of these gray regions. The local contrast of an XLD-PEEM image can be described as:

$$I_{XLD}(\theta) = a + b\,(3cos^2\theta - 1)\langle \boldsymbol{L}^2 \rangle \tag{3.1}$$

where a and b are material constants, $\boldsymbol{L}$ is the AFM moment, and θ is the angle between $\boldsymbol{L}$ and the $\boldsymbol{E}$-vector of the linearly polarized incident x-rays [108]. In order to fully identify the orientation of the AFM spin axis, images were captured as the orientation of the $\boldsymbol{E}$-vector was varied from *p*- to *s*-polarization, *i.e.*, as the polarization angle, ψ varies from 0 to 90°. At each polarization angle, images were collected at two x-ray energies corresponding to the positive/negative peaks in the L_2 XLD signal (dashed lines in **Fig. 3.6(c)**) and the final asymmetry XLD image was calculated. **Fig. 3.7(b)** shows the XLD-PEEM image acquired at

$\psi = 45^{o}$ where the domain contrast was the strongest. As with the XMCD-PEEM image, long horizontal stripes are also observed in the XLD-PEEM image with alternating black/gray contrast. Comparing the XMCD- and XLD-PEEM images (*e.g.*, region highlighted by the red square), the FM domains (white/black dots) correspond to gray regions in the XLD-PEEM image, while the gray regions in the XMCD-PEEM image correspond to black regions in the XLD-PEEM image. As shown in **Fig. 3.8**, the contrast in the black regions have the expected ψ dependence for AFM domains oriented along the [001] substrate direction while the gray regions do not show a significant ψ dependence as expected for a FM domain. These images conclusively confirm the coexistence of the FM and AFM domains through the formation of elongated domains oriented along the [001] substrate direction. PEEM images from other regions of the sample also show the correspondence between the FM and AFM domains, but the directions of the elongated domains vary from location to location across the sample.

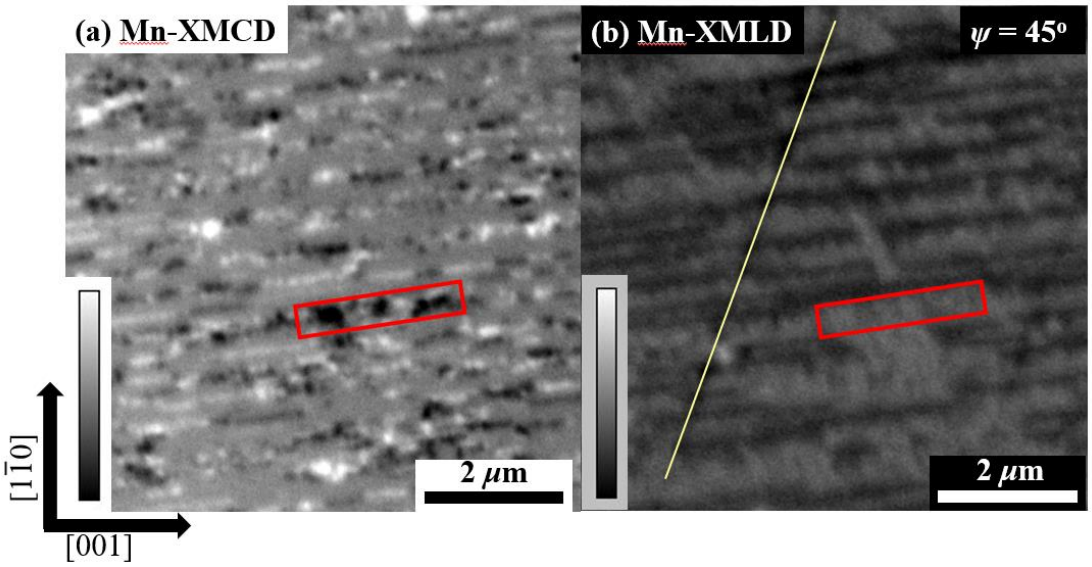

Fig. 3.7*. Mn (a) XMCD- and (b) XLD- PEEM (ψ = 45°) images at 110 K taken from the same location. The red rectangle highlights a region with small FM domains which correlates to a gray region in the XLD-PEEM image. The slashed yellow line in (b) is a scratch on the sample surface.*

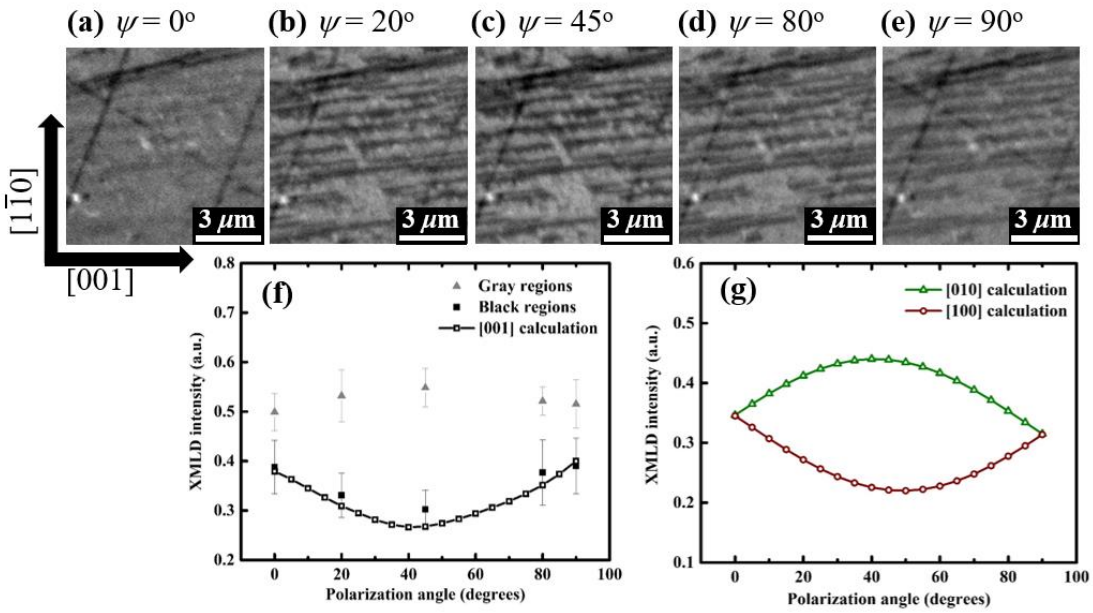

Fig. 3.8*. XLD-PEEM images taken at polarization angle, ψ, equal to (a) 0°, (b) 20°, (c) 45°, (d) 80°, and (e) 90°. (f) XLD intensity as a function of ψ where filled points are experimental data and the open points are calculated data using* ***Eqn. (3.1)****. The black/gray regions are referring to the corresponding contrast in panels (a)-(e). The error bars were determined by the standard deviation of the pixel intensity values in each domain. (g) The calculated fits for* $[100]_{pc}$ *and* $[010]_{pc}$ *orientation of the AFM spin axes. The calculation of* ***Eqn. (3.1)*** *using the measurement geometry and possible orientations of the AFM spin axes showed that the black regions correspond to AFM domains with spins oriented along the* $[001]_{pc}$ *substrate direction.*

3.4 Conclusion

In summary, the electronic and magnetic transitions of NSMO thin films grown on (110)-oriented STO substrates were probed using a combination of bulk and synchrotron radiation-

based characterization techniques. Under optimized growth conditions, the NSMO film showed both lateral and vertical phase separation, where it consisted of three layers with differing density and magnetic properties. The main NSMO layer constitutes the majority (14.7 nm) of the total film thickness (16.5 nm), and displays bulk-like density. This main layer was fully strained in the in-plane [001] direction while partially relaxed in the in-plane $[1\bar{1}0]$ direction. Resistivity and magnetization measurements revealed that with decreasing temperature, this strain state enabled the NSMO film to transform from a PM/insulating to FM/metallic state at ~ 197 K and then to an AFM/charge-ordered insulating phase at ~ 150 K. In order to directly probe the FM and AFM properties of the main NSMO layer, Mn-XMCD/XLD spectroscopy and microscopy were performed as a function of temperature. A carefully designed XLD spectroscopy measurement allowed us to extract the pure AFM signature of the NSMO film. While a clear AFM signature existed below T_N, it is found that a proportion of the FM phase remained for temperatures down to 80 K. The lateral coexistence of the FM and AFM phases was directly imaged by X-PEEM where they form extended domains along the [001] substrate direction. The correspondence between the FM and AFM domains exists across the sample, but the directions of the elongated domains vary from location to location. This understanding of the electronic/magnetic transitions of NSMO in thin film form is necessary to enable its incorporation into next generation memory devices.

Chapter 4: Cation and Anion Topotactic Transformations in Cobaltite Thin Films Leading to Ruddlesden-Popper Phases

4.1 Introduction

Ion migration-induced modification of physical properties is an emerging research direction in the search for tunable materials that can revolutionize the growing field of neuromorphic computing [109-111]. Among the candidate materials, perovskite oxides with the chemical formula ABO_3 are of interest because of their wide range of physical properties, high oxygen ion conductivities, and the multitude of related phases such as the Grenier ($ABO_{2.7}$), brownmillerite (BM, $ABO_{2.5}$), square planar (SP, ABO_2) [112,113], and Ruddlesden-Popper (RP, $A_{n+1}B_nO_{3n+1}$ where n = integer) [50,114] phases (see **Fig. 4.1**). Previous studies on these materials have focused on the impact of the A and B stoichiometry [115,116], however recent studies have turned to the oxygen stoichiometry where topotactic transformations can occur between related structural phases due to a loss or gain of oxygen ions while retaining a relationship in the crystallographic orientation [13-15]. Relative to the parent perovskite phase, oxygen deficiency, δ (where $0 < \delta < 1$), is accommodated by a lowering of the average B-ion valence state and a change in the local coordination environment from corner-shared BO_6 octahedra in the perovskite phase, to alternating layers of BO_6 octahedra and BO_4 tetrahedra in the BM phase (see structural diagrams in **Fig. 4.1(b)** and **Fig. 4.2(k and m)**). Further reduction from the BM phase can lead to an in-plane BO_4 coordination in the SP phase, or even one of

the RP phases, where both *B* and oxygen ions are partially depleted from the parent perovskite phase. As a result, these structural changes lead to substantial modification to the physical properties.

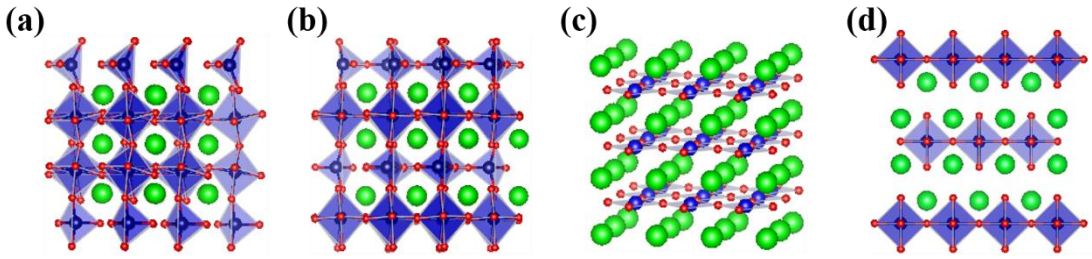

Fig. 4.1. *Structural diagrams of (a) Grenier ($ABO_{2.7}$), (b) brownmillerite (BM, $ABO_{2.5}$), (c) square planar (SP, ABO_2), and (d) Ruddlesden-Popper (RP, $A_{n+1}B_nO_{3n+1}$ where n = 1) phases. The green, blue and red spheres represent the A, B and O ions, respectively. Topotactic transformations can occur between these related structural phases due to a loss or gain of oxygen or perovskite B-site ions while retaining a relationship in the crystallographic orientation. These structural changes lead to substantial modification to the physical properties.*

A gradual progression between the perovskite and BM phases have previously been demonstrated in several complex oxide systems, including $La_{0.7}Sr_{0.3}CoO_3$ [48,49], $La_{0.67}Sr_{0.33}MnO_3$ [117], and $YBa_2Cu_3O_{7-\delta}$ [118], by the deposition of ultrathin Gd layers of varying thickness. The Gd getter layer experienced a spontaneous redox reaction to form GdO_x,

leaching oxygen ions from the underlying complex oxide thin films and resulting in a topotactic transformation, which then leads to a change in the magnetic and electrical properties in these complex oxides. Other studies focused on the $SrFeO_{3-\delta}$ and $SrCoO_{3-\delta}$ systems where a reversible transformation between the stable BM $SrFeO_{2.5}$ ($SrCoO_{2.5}$) phase and the metastable $SrFeO_3$ ($SrCoO_3$) perovskite phase was observed with an applied electrical field or under optimized *oxidizing* annealing conditions [42-47]. With further *reduction*, BM $SrFeO_{2.5}$ films could transform to infinite-layer $SrFeO_2$ SP phase [46,119]. However, in the cobaltite system, further *reduction* of BM $SrCoO_{2.5}$ films led to amorphous films or nano-twinned, tetrahedrally-coordinated phases [47,120] rather than the formation of $SrCoO_2$ SP phase or even the Sr_2CoO_4 [121,122] RP phase. Therefore, this work investigates the mechanisms and the phase stability associated with cobaltite topotactic transformations.

A series of topotactic transformations were initiated in Sr-doped lanthanum cobaltite ($La_{0.7}Sr_{0.3}CoO_{3-\delta}$, LSCO) thin films exposed to anneals under highly reducing conditions. At this Sr-doping level, the perovskite phase is the equilibrium phase, characterized by coincident metal (M)-to-insulator (I) and ferromagnetic (FM)-to-paramagnetic transitions at the Curie temperature, $T_C \sim 240$ K [123], a high oxygen vacancy conductivity, and relatively low oxygen vacancy formation energy [124]. The anneals were performed using either a Mg-trap annealing system [125] or a gas evolution system [126] which enabled the exploration of wide

temperature/pressure phase space ranging from room temperature to 1000 °C and pressures from 10^{-25} to 10^{-1} atm (see **Fig. 4.2(a)**). X-ray absorption (XA) spectroscopy, and scanning transmission electron microscopy (STEM) showed that these structural transformations involved a change of the Co local coordination from a mixture of Co^{3+}/Co^{4+} ions in octahedral coordination in the perovskite phase to Co^{2+} ions in octahedral coordination in a $La_{1.4}Sr_{0.6}Co_{1+\upsilon}O_{4-\delta}$ RP phase (where $0 \leq \upsilon < 1$ and $0 < \delta < 1$) formed under the most reducing conditions. Raman spectroscopy and first principles calculations suggest that the formation of the RP phase involves the loss of both oxygen anions and Co ions through an intermediary BM phase. As a result, the magnetic properties evolved between various FM and antiferromagnetic (AFM) phases, and the room temperature resistivity spanned eight orders of magnitude. Compared to the perovskite and BM phases widely reported in the previous literature, the formation of the RP phase was successfully observed with its own distinct physical and functional properties. Furthermore, the combination of experiment and theory enabled us to elucidate the formation mechanisms for each of the reduced phases.

In this chapter, the LSCO thin films were annealed by Dr. Min-Han Lee at University of California, San Diego, and Dr. Zhen Zhang at Purdue University. The STEM images and Raman spectroscopy were acquired by Dr. Shaobo Cheng at Brookhaven National Laboratory and Larry Heki at University of California, Santa Barbara, respectively. The first principles

calculations were performed by Dr. Shenli Zhang at University of Chicago.

4.2 Experimental and Theoretical Methods

Epitaxial LSCO thin films (thickness of 16~28 nm) were deposited on (001)-oriented $(LaAlO_3)_{0.3}(Sr_2TaAlO_6)_{0.7}$ (LSAT) substrates by pulsed laser deposition with a laser pulse frequency of 1 Hz and laser fluence of ~ 0.8 J cm^{-2}. During the growth, the substrate temperature was held at 700 °C and the oxygen pressure was 300 mTorr. The films were cooled slowly to room temperature after the deposition with an oxygen pressure of 300 Torr to ensure proper oxygen stoichiometry. The LSCO films were annealed for 1 hour either in a gas evolution system which consists of a tube furnace connected to a high vacuum system capable of achieving pressures from 10^{-12} to 0.1 atm and temperatures up to 1000 °C [126], or a Mg-based oxygen trap system capable of achieving pressures down to 10^{-25} atm and temperatures up to 400 °C [125]. In the gas evolution system, the base pressure was maintained at ~10^{-10} atm, and high-purity oxygen (>99.99%) of different pressures ranging from 10^{-12} to 10^{-7} atm was introduced into the annealing chamber using the computer-controlled metal-seated valve [126]. During the Mg-trap annealing experiments, the Mg-based oxygen trap and annealing chamber was maintained at 1 atm total pressure, and the low oxygen partial pressure was generated by flowing ultrahigh purity argon gas through a heated Mg powder bed. The trace amount of oxygen in ultrahigh purity argon reacts with Mg, creating further reduction in the oxygen partial

pressure as it flows into the chamber [125]. All of the pressures quoted in the following sections are referring to the oxygen partial pressures, P_{O_2}.

The structural properties of the films were characterized by x-ray reflectivity (XRR) and high-resolution x-ray diffraction (XRD) using either a Bruker D8 Discover or Rigaku Smartlab four-circle diffractometer using Cu $K_{\alpha 1}$ x-rays. The XRD data for the AG-P LSCO sample was obtained at Beamline 7-2 at the Stanford Synchrotron Radiation Light Source using an x-ray energy of 14 keV. The XRR curves were fit using GenX software to determine the thickness, roughness, and density of the films [89]. A Lakeshore cryogenic probe station was used to measure the film resistivity upon warming from 80 K with the van der Pauw geometry. The bulk magnetic properties were measured using a Quantum Design VersaLab or Physical Property Measurement System vibrating-sample magnetometer (VSM) with the magnetic field applied along the in-plane [100] substrate direction. Soft x-ray magnetic spectroscopy at the Co *L*-edge was performed at 80 K at beamlines 4.0.2 and 6.3.1 at the Advanced Light Source (ALS) using total electron yield detection (TEY, which provides surface sensitive measurements to the top 5-10 nm of the sample), and luminescence yield detection (LY, which probes the full film thickness [63]). The x-rays were incident upon the sample at a 30° grazing angle along the in-plane [100] substrate direction. X-ray magnetic circular dichroism (XMCD) spectra were calculated as the difference between XA spectra acquired using right/left

circularly polarized x-rays with a 1.93 T magnetic field oriented parallel to the propagation direction of the circularly polarized x-rays. The magnetic field of 1.93 T was chosen to saturate the ferromagnetic moments in the film. X-ray linear dichroism (XLD) spectra were calculated as the difference between XA spectra acquired using *s*- and *p*-polarized x-rays such that the x-ray ***E***-vector is respectively parallel to the in-plane [010] substrate direction or 30° away from the [001] substrate direction, due to the grazing-incidence geometry of the measurements.

High angle annular dark field (HAADF) STEM images and electron energy loss spectroscopy (EELS) mappings were acquired by a double corrector JEOL ARM 300F TEM. A 30 μm condenser aperture was selected for EELS acquisition. The convergent and collection semi-angles are 21 μm and 90 μm, respectively. The samples used for TEM characterizations were made by standard focus ion beam (FEI Helios NanoLab) lift-out method. Raman spectra were measured at room temperature using a Horiba Jobin Yvon T64000 Raman spectrometer. The excitation light of 488 nm was focused onto the sample using a 100x objective. The signal was collected in a backscattering geometry and excitation light was blocked by a notch filter. Photoluminescence (PL) spectra were taken using a home-built system coupling an inverted microscope to an imaging spectrometer. The sample was excited with 405 nm light under a 20x objective. Excitation light was rejected by a long pass filter.

First principles calculations were performed using the Quantum Espresso code (v6.4.1) [127,128], which solves the Kohn-Sham equations of DFT using plane waves and pseudopotentials. In particular DFT+U (U = 3 eV as justified in previous calculations) [129] was used, with the generalized gradient approximation of Perdew-Burke-Ernzerhof (PBE) [130] for the exchange-correlation functional and the projected augmented wave pseudopotentials from the PSlibrary [131] (v1.0.0 for La, Sr and O, and v0.3.1 for Co). A previously optimized BM structure [129] was used to calculate the formation energy of Co or O vacancies in the BM phase, which was modeled with a 36-atom orthorhombic cell with the stoichiometry of $La_{0.63}Sr_{0.37}CoO_{2.5}$. The initial RP phase was constructed from the La_2CoO_4 structure (ID: mp-27494) from the Materials Project [132], where 37.5% La was substituted by Sr in this 28-atom orthorhombic cell. Defective BM structures and the RP structure were then optimized within the orthorhombic lattice symmetry, using a plane-wave cutoff of 1224 eV and a Monkhorst-Pack k-point grid [133] with the resolution between 0.02-0.03 $Å^{-1}$. The convergence thresholds for energy, force and pressure were set to 2.0×10^{-4} eV per formula unit (f.u.), 0.02 eV $Å^{-1}$ per f.u. and 0.5 Kbar, respectively.

4.3 Results and Discussion

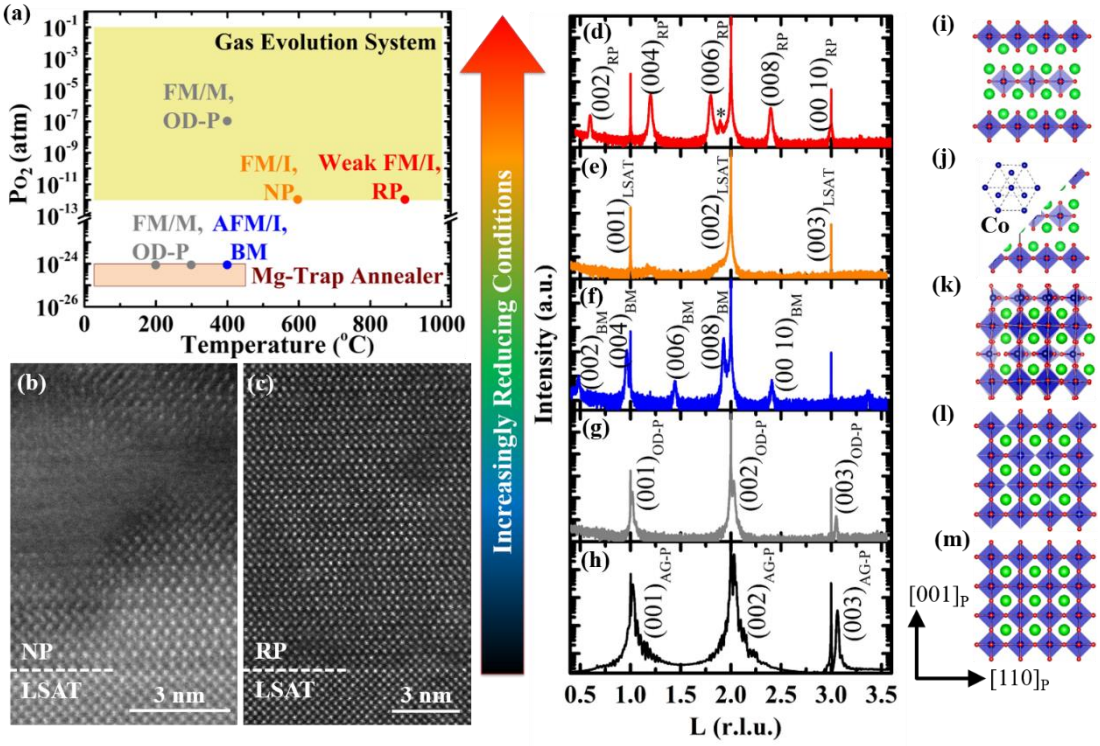

Fig. 4.2. *(a) Phase diagram of the structural, magnetic, and electrical properties of LSCO films exposed to anneals under highly reducing conditions. The same structural phase can be achieved when the film is annealed in different temperature and* P_{O_2} *conditions. (b-c) HAADF STEM images of the nanoparticle (NP) and RP samples, respectively. (d-h) XRD curves, and (i-m) crystal structure diagrams for the annealed LSCO films. The increasingly reducing conditions refer to higher temperatures and/or lower* P_{O_2}*, where the temperature appears to have a larger effect in triggering the phase transformations since the ions need to have enough kinetic energy to move around inside the lattice. The XRD curves show sharp, high intensity peaks arising from the LSAT substrate and weaker film peaks arising from the (00L) planes of the respective structure. In (d), the * peak results from the sample holder. In (i-m), the green*

and red atoms represent La/Sr and oxygen ions, respectively, while Co ions (blue) sit in the center of the octahedra/tetrahedra. As shown in (j), this NP phase consisted of both the polycrystalline grains of the RP phase and metallic Co nanoparticles. The metallic Co nanoparticles are not observed due to their small size, low density, and/or their misalignment relative to the zone axis of the image.

The range of possible annealing conditions available with the gas evolution and Mg-trap annealing systems is indicated by the shaded regions in **Fig. 4.2(a),** while the symbols represent the conditions explored in this work. Upon exposure to increasingly reducing conditions (*i.e.*, lower pressure and/or higher temperature), the LSCO thin films gradually underwent several topotactic transformations as revealed through XRR (**Fig. 4.3**) and XRD measurements (**Fig. 4.2(d)-(h)**). The XRR curves reveal substantial changes in the film thickness, density, and roughness associated with each of these transformations. **Tables 4.1** and **4.2** list the parameters obtained from fitting the XRR curves using GenX software [89]. For anneals up to 600 °C/10^{-12} atm P_{O_2}, a trend of decreasing density and increasing film thickness and roughness can be observed, as expected for perovskite-related materials with increasing oxygen deficiency [134,135]. In particular, the LSCO thin film annealed at 600 °C/10^{-12} atm P_{O_2}, experiences a 50.5% increase in the total film thickness (18.6 nm to 28.0 nm) and 29.9% decrease in the main layer density (6.79 g cm^{-3} to 4.76 g cm^{-3}). Finally, increasing the annealing

temperature to 900 °C/10^{-12} atm P_{O_2} leads to a recovery of the film density to 6.28 g cm^{-3} (22.6% decrease from the as-grown perovskite (AG-P) sample) and roughness, accompanied with a small decrease in thickness to 17.3 nm (5.46% decrease). The recovery of the film density indicates the film annealed at 900 °C/10^{-12} atm P_{O_2} has transitioned to a different structural phase compared to that annealed at 600 °C/10^{-12} atm P_{O_2}. Therefore, the XRR results suggest that these highly reduced films have experienced substantial structural modification upon annealing.

Analysis of ω-2θ XRD curves (**Fig. 4.2(d)-(h)**) enable the identification of the phases present after each reducing anneal. Reciprocal space maps (RSMs, **Fig. 4.4**) show that the thin films remain coherently strained to the underlying LSAT substrate regardless of annealing conditions. **Fig. 4.2(h)** shows the expected series of (00*L*) peaks for the perovskite phase with an out-of-plane lattice parameter of 3.806 Å. The first transformation took place when the film was annealed at 200 °C and 300 °C/10^{-24} atm P_{O_2} as well as 400 °C/10^{-7} atm P_{O_2}. As shown in **Fig. 4.2(g)**, the same series of (00*L*) peaks can be observed, indicating the perovskite phase is maintained. However, the film peaks are shifted to slightly lower 2θ values compared to the AG-P phase, suggesting an increased lattice parameter and corresponding to the transformation from AG-P to oxygen-deficient perovskite (OD-P) phase. For the sample annealed at 400 °C/10^{-7} atm P_{O_2}, the out-of-plane lattice parameter increases to 3.812 Å which is consistent

with the 6.0% decrease in density obtained from the XRR curves, confirming the formation of the OD-P phase [136,137].

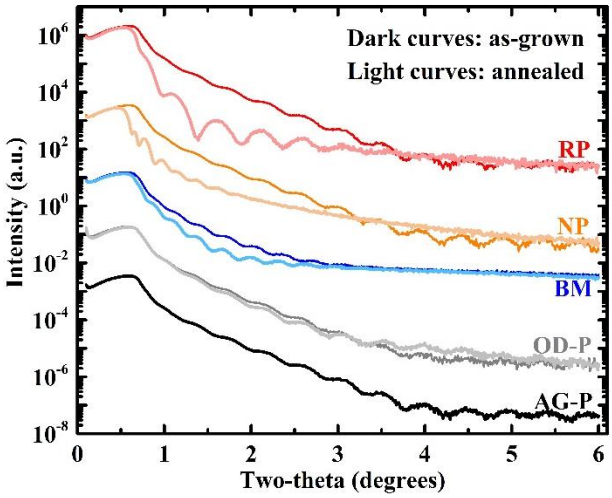

Fig. 4.3. *XRR curves of the LSCO films exposed to anneals under highly reducing conditions. The dark and light lines refer to the initial and annealed samples, respectively. The acronyms of the structural phases are defined as follows: AG-P: as-grown perovskite; OD-P: oxygen-deficient perovskite; NP: nanoparticle. The XRR curves reveal substantial changes in the film thickness, density, and roughness associated with each of the topotactic transformations.* ***Tables 4.1*** *and* ***4.2*** *list the parameters obtained from fitting the XRR curves using GenX software [89]. Due to the exposure of the samples to atmosphere after the annealing and before the x-ray measurements, a thin surface carbon-containing layer was added to refine the simulation [92] for the post-annealed samples.*

Table 4.1. *XRR fitting parameters for the samples before annealing*

Sample	Fitting model	Thickness (nm)	Roughness (nm)	Density (g cm^{-3})
$RP_{initial}$	$La_{0.7}Sr_{0.3}CoO_3$	18.3 ± 0.03	0.52 ± 0.02	6.79 ± 0.01
$NP_{initial}$	$La_{0.7}Sr_{0.3}CoO_3$	18.6 ± 0.02	0.47 ± 0.04	6.79 ± 0.02
$BM_{initial}$	$La_{0.7}Sr_{0.3}CoO_3$	26.0 ± 0.03	0.68 ± 0.02	6.79 ± 0.01
OD-$P_{initial}$	$La_{0.7}Sr_{0.3}CoO_3$	18.6 ± 0.02	0.60 ± 0.02	6.78 ± 0.01
AG-P	$La_{0.7}Sr_{0.3}CoO_3$	18.3 ± 0.03	0.42 ± 0.04	6.79 ± 0.00

Table 4.2. *XRR fitting parameters for the samples after annealing*

Sample	Fitting model	Thickness (nm)	Roughness (nm)	Density (g cm^{-3})
RP	Carbon	0.52 ± 0.02	0.02 ± 0.00	0.99 ± 0.04
	$La_{1.4}Sr_{0.6}Co_{1+\upsilon}O_{4-\delta}$	17.3 ± 0.05	3.04 ± 0.06	6.28 ± 0.02
NP	Carbon	0.45 ± 0.03	0.05 ± 0.01	2.05 ± 0.05
	$La_{1.4}Sr_{0.6}Co_{1+\upsilon}O_{4-\delta}$	28.0 ± 0.08	3.49 ± 0.09	4.76 ± 0.06
BM	Carbon	1.00 ± 0.01	0.08 ± 0.00	1.90 ± 0.02
	$La_{0.7}Sr_{0.3}CoO_{2.5-\delta}$	26.9 ± 0.03	1.62 ± 0.06	6.03 ± 0.04
OD-P	Carbon	1.00 ± 0.02	0.82 ± 0.04	2.95 ± 0.03
	$La_{0.7}Sr_{0.3}CoO_{3-\delta}$	19.9 ± 0.05	0.32 ± 0.01	6.37 ± 0.03

Transformation to BM*:*

Annealing the LSCO thin films at 400 $^oC/10^{-24}$ atm P_{O_2} resulted in the transformation to the BM phase, as characterized by the dramatic shift of the main (00*L*) film peaks to the low angle side of the LSAT substrate peak, as well as the appearance of prominent half-order peaks due to the quadrupling of the unit cell from the alternating octahedral and tetrahedral layers. The lattice parameter for this BM phase is 16.053 Å. The XRR curves indicate a 6.7% increase in

total film thickness and 13% decrease in density accompany the transformation to the BM phase, consistent with prior studies of the perovskite-BM transformation in $SrCoO_{3-\delta}$ [13,42,109] and $La_{0.7}Sr_{0.3}CoO_{3-\delta}$ [48] films. The BM $La_{0.7}Sr_{0.3}CoO_{2.5}$ phase was found to be metastable and slowly transformed back to the perovskite phase over a period of several months at room temperature in air, even when capped with 5 nm Gd/5 nm Au to try to prevent oxygen reincorporation into the film.

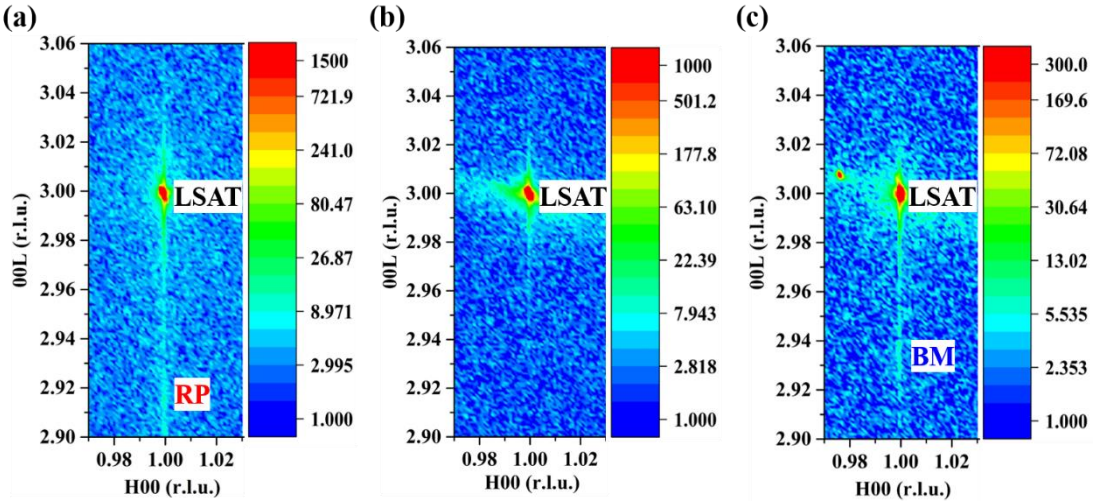

Fig. 4.4*. RSMs around the (103) substrate peak for (a) RP, (b) nanoparticle (NP), and (c) BM films on (001)-oriented LSAT substrates. The film peaks are aligned vertically with the (103) peak from the substrate regardless of the annealing conditions, indicating that the LSCO films remain fully strained in the in-plane <100> directions with their underlying LSAT substrates.*

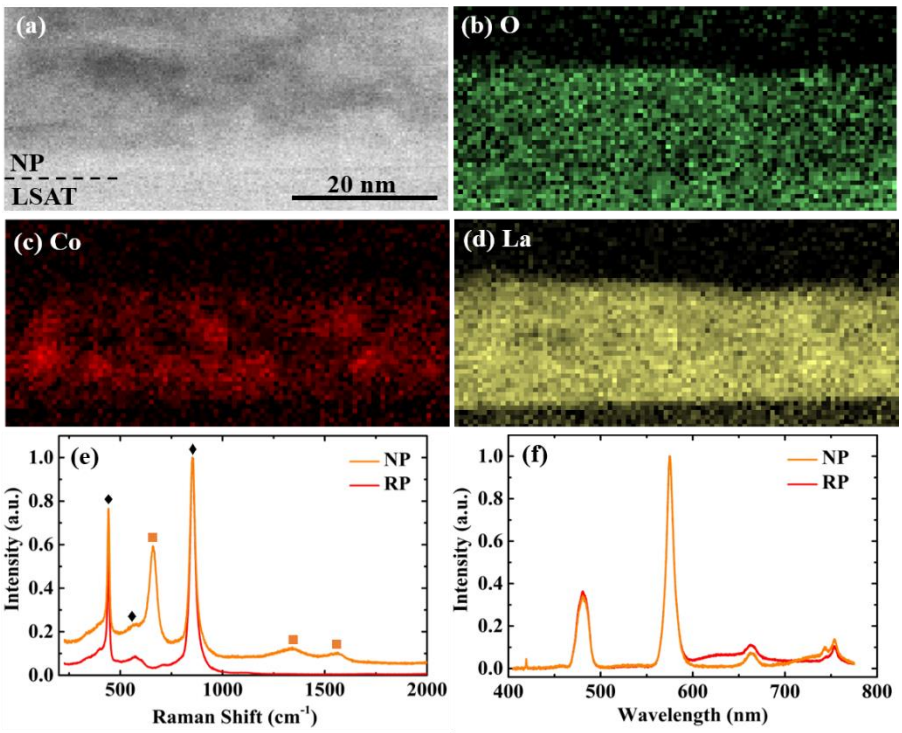

Fig. 4.5*. (a) EELS elemental mapping of the NP sample taken at the substrate-film interface showing maps of the (b) oxygen, (c) cobalt, and (d) lanthanum edges. (e) Raman and (f) PL spectra of the NP (orange) and RP (red) samples. Raman lines from the LSAT substrate [146] are denoted with the black diamond symbols (♦), while those from the cobalt nanoparticles are denoted with the orange squares (■). In (f), all of the PL features arise from the excess Co ions in the NP and RP films.*

Transformation to NP*:*

Upon annealing at 600 ^{o}C/10^{-12} atm P_{O_2}, the film peaks disappear as shown in **Fig. 4.2(e)**. This absence of film peaks could be explained by amorphization of the LSCO thin film or the formation of a nano-textured phase where the film breaks up into small crystalline regions in

which the planes are not oriented parallel to the substrate surface. HAADF STEM images (**Fig. 4.2(b)**) demonstrated that after annealing, this sample consisted primarily of polycrystalline grains of the RP phase separated by amorphous regions/regions of low crystallinity, or regions misaligned to the zone axis of the image. The out-of-plane lattice parameter of this polycrystalline RP structure is 12.25 ± 0.21 Å, where the (001) planes are not perfectly aligned with the underlying LSAT substrate due to the presence of defects and dislocations at the film-substrate interface. Furthermore, EELS elemental mapping in **Fig. 4.5** demonstrates that this thin film has a non-uniform Co distribution while maintaining more uniform distributions of the La and O ions. In **Fig. 4.5(e)**, the Raman spectra showed peaks at 683, 1366, and 1590 cm^{-1}, which can be assigned to the Raman lines of Co nanoparticles [138-140]. Therefore, this sample is referred as the nanoparticle (NP) sample. The formation of the Co nanoparticles accounts for the loss of Co ions needed in order to form the RP phase, however their small size, low density, and/or random orientation precludes their observation in XRD or STEM measurements. Similar effects have been observed in the electrodes of solid oxide fuel cells where nickel particles exsolved from nickel oxides [141,142].

***Transformation to RP**:*

As the LSCO thin films were annealed at 900 $^{o}C/10^{-12}$ atm P_{O_2}, a new epitaxial phase emerged with a pattern of peaks distinct from the perovskite or BM phases. These peaks can be indexed

to an out-of-plane lattice parameter of 12.89 Å. A lack of thickness fringes (**Fig. 4.6**) indicates that compared to the AG-P sample, this phase has large interfacial roughness and *d*-spacing variations, further confirmed by XRR in **Fig. 4.3** and **Table 4.2**. HAADF STEM imaging (**Fig. 4.5(c))** confirmed that this sample consists of a single crystalline $La_{1.4}Sr_{0.6}Co_{1+\upsilon}O_{4-\delta}$ RP structure [50] with an out-of-plane lattice parameter of 12.83 ± 0.05 Å which is coherently strained to the underlying LSAT substrate. Raman spectra showed that the Co nanoparticles were no longer present, however, PL spectra (**Fig. 4.5(f)**) show multi-peaked emission spanning the visible and near-infrared wavelengths (from 480 to 755 nm). Similar spectra have been observed from isolated Co^{2+} ions in a variety of host crystals [143-145], suggesting that these PL features also arise from excess Co ions that are generated when the LSCO thin films are reduced. Unlike the BM phase, this RP phase is stable under ambient conditions for a timeframe of years, as determined through XRD measurements.

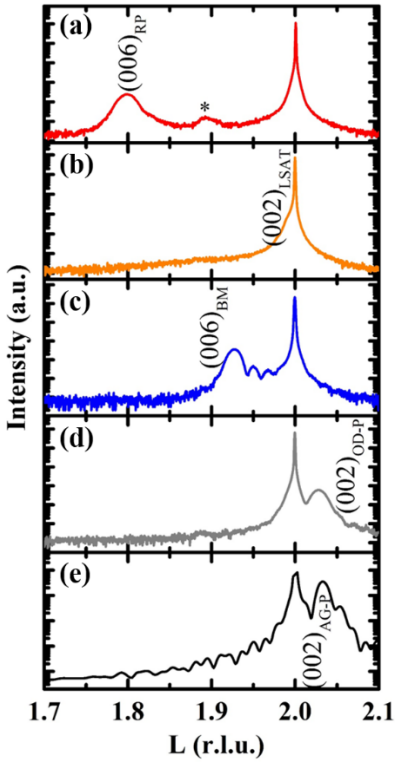

Fig. 4.6*. Zoom-in XRD curves for the LSCO films exposed to anneals under highly reducing conditions (a) 900 ℃/10^{-12} atm P_{O_2}, (b) 600 ℃/10^{-12} atm P_{O_2}, (c) 400 ℃/10^{-12} atm P_{O_2}, (d) 400 ℃/10^{-7} atm P_{O_2}, and (e) AG-P film. In (a), the * peak results from the sample holder. Analysis of ω-2θ XRD curves enable the identification of the phases present after each reducing anneal. This figure showed the zoom-in XRD plot between L=1.7 and L=2.1 reciprocal lattice units (r.l.u.) showing sharp and high intensity peaks from the LSAT substrate and weaker film peaks. The lack of thickness fringes in panels* ***(a)-(d)*** *indicates higher interface roughness and poorer crystallinity compared to the AG-P film.*

Density functional theory (DFT) calculations further support the assignment of the RP phase to the 900 °C annealed sample, as the calculated structural, magnetic and electronic properties

(**Table 4.3** in **Section 4.4**) all showed good agreement with experimental measurements. In particular, the computed out-of-plane lattice parameter decreased by 19.5 % in the transformation from the BM phase (15.86 Å) to the RP phase (12.76 Å), consistent with the experimentally observed 20% change from BM (16.053 Å) to the 900 °C annealed sample (12.83 Å). A G-type AFM ordering with insulating properties was identified in the calculations with a small net magnetic moment ~0.25 μ_B per Co ion, consistent with the high resistivity and weak FM properties identified below 25 K (as further discussed below). Moreover, the calculated formation energy of cobalt and oxygen vacancies in the BM phase (see **Table 4.4** and the related discussion in **Section 4.4**) revealed that the BM to RP phase transition is thermodynamically possible; indeed it was found that the cobalt vacancy requires lower energy to form than the oxygen vacancy in the BM phase, either at the standard condition (27 ^{o}C/1 atm) or at the 600 ^{o}C/10^{-12} atm annealing condition, and their formation energies are comparable at the 900 ^{o}C/10^{-12} atm annealing condition. This result indicates that the loss of cobalt and oxygen ions in the BM phase is likely, which is a necessary step to form the RP phase and justifies the appearance of Co nanoparticles detected in experiments.

4.3.1 Soft XA spectroscopy studies

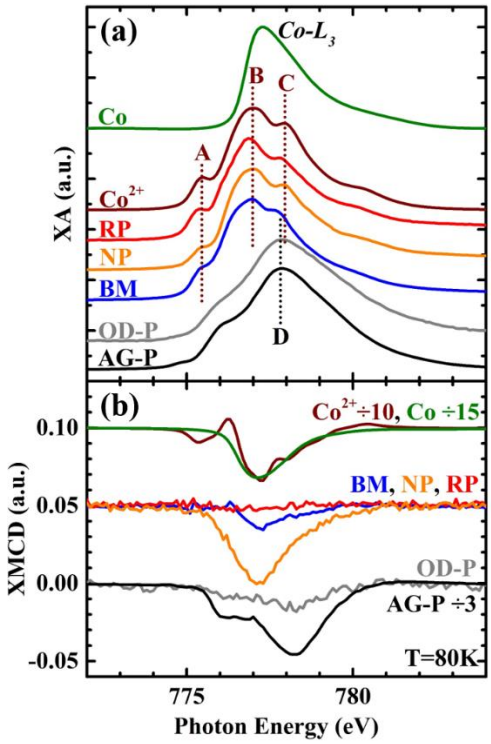

***Fig. 4.7**. Zoomed-in (a) Co $L_{3,2}$ XA and (b) XMCD spectra acquired at 80 K for LSCO thin films after reducing anneals. Reference spectra for Co^{2+} ions in octahedral coordination [147] and metallic Co are also included. The XA spectral features of Co^{2+} ions are denoted with (A-C) dotted lines and the main peak of the Co^{3+}/Co^{4+} ions with a (D) dotted line.*

XA spectra (**Fig. 4.7(a)** and **4.8(a)**) were acquired in order to detect the change in Co valence state and local coordination associated with the topotactic transformations. Reference spectra for Co^{2+} ions in octahedral coordination ($CoFe_2O_4$ [147]) and metallic Co are included for comparison. The AG-P sample agrees with literature data for mixed valence Co^{3+}/Co^{4+} ion in octahedral coordination [148,149]. The OD-P sample shows only subtle changes compared the

AG-P sample in the form of slightly less defined spectral features. On the other hand, the XA spectra of the highly reduced phases (BM, NP, and RP) show clear signatures of Co^{2+} ions in octahedral coordination with subtle differences in the intensities of the three main spectral features denoted with (A)-(C) dotted lines. The decrease in the Co valence state in the highly reduced phases is expected in order to maintain charge neutrality upon increase in oxygen deficiency, δ. The subtle spectral differences for the highly reduced phases likely arise from the fact that the Co ions in the BM sample are in mixed octahedral/tetrahedral coordination, while those in the NP and RP samples also have contributions from the Co nanoparticles and isolated Co ions, respectively. In the ideal RP structure with the chemical formula of $La_{1.4}Sr_{0.6}CoO_4$, the average Co valence state is $Co^{2.6+}$; however, our annealed NP and RP samples are likely Co-rich with stoichiometry of $La_{1.4}Sr_{0.6}Co_{1+\upsilon}O_{4-\delta}$, where $0 \leq \upsilon < 1$, resulting in lower average Co valence state.

XMCD measurements at the Co $L_{3,2}$ absorption edges (**Fig. 4.7(b)** and **4.8(b)**) provide complementary information on the element/coordination specific contributions to the FM properties of the annealed LSCO thin films. Compared to the AG-P sample, the saturation magnetization (M_S) of the OD-P films decreased by 60% as the oxygen vacancies break up the Co^{3+} - O^{2-} - Co^{4+} double exchange network [150,151] and potentially introduces local AFM structures for Co ions near vacancies [129,152]. While the XA spectra for the BM, NP, and RP

samples were similar (**Fig. 4.7(a)**), stark differences exist in the XMCD spectra. No FM signal was detected for the RP sample at 80 K, and the BM sample showed a weak FM signal with spectral features matching that of Co^{2+} ions in octahedral coordination. The XMCD magnitude of the BM sample is only 4.7% of the $CoFe_2O_4$ reference spectra. In contrast, the sample referred to as the NP phase shows a broad negative peak without the multiplet structure typically found in complex oxides and is more reminiscent of metallic Co atoms. Fitting of the XA and XMCD spectra for this sample (**Fig. 4.9**) shows that it can be considered as a mixture consisting of approximately 77% of RP phase and 23% metallic Co, consistent with the Raman spectra. The small size of these Co nanoparticles precludes their detection through XRD or STEM measurements. As shown in **Fig. 4.10**, the hysteresis loops show that this phase has a substantially lower coercivity compared to the AG-P phase (*i.e.*, H_C = 0.1 T compared to H_C ~ 1.25 T, respectively), consistent with Co nanoparticles [153,154].

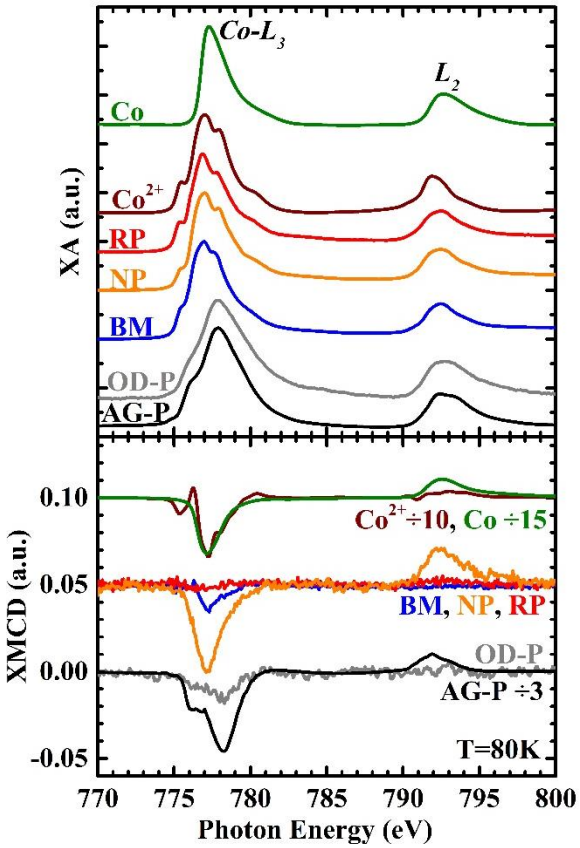

Fig. 4.8*. (a) Co $L_{3,2}$ XA and (b) XMCD spectra acquired at 80 K for LSCO thin films after reducing anneals. Reference spectra for Co^{2+} ions in octahedral coordination [147] (brown) and metallic Co (green) are also included. XA and XMCD spectra provides information about the change in Co valence state, local coordination, and magnetically active ions associated with the topotactic transformations.*

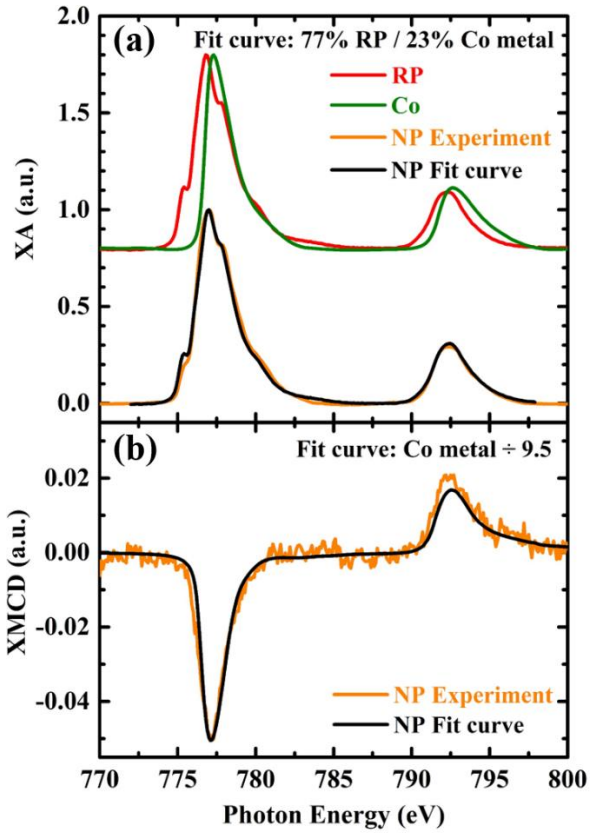

***Fig. 4.9**. Experimental curves (orange) and simulation results (black) of (a) Co $L_{3,2}$ XA and (b) XMCD spectra acquired at 80K for the NP sample. The XA and XMCD spectra of NP phase were fit to reference spectra to quantitatively estimate their valence states. Reference spectra used for the fitting include Co ions in the experimental RP phase (red) and in the metallic Co (green). The fitting results show that the NP sample can be considered as a mixture consisting of ~ 77% RP phase and ~ 23% metallic Co.*

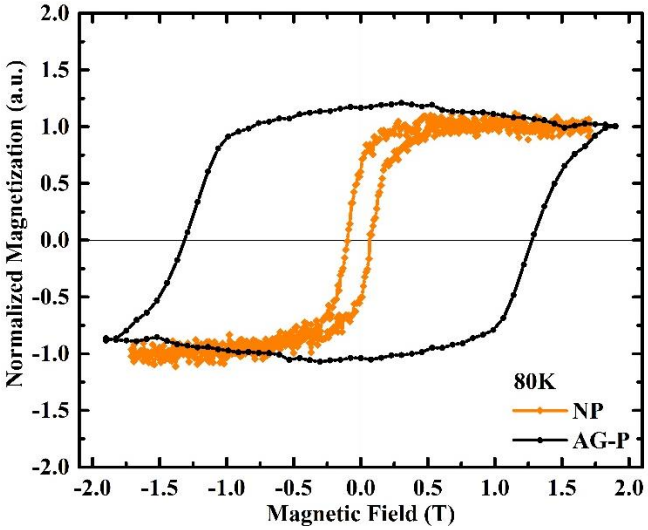

***Fig. 4.10**. Co L_3 XMCD hysteresis loops at 80 K for the NP (orange) and AG-P (black) samples. XMCD hysteresis loops were acquired by tuning the x-ray energy to the photon energy corresponding to the maximum XMCD signal and cycling the applied magnetic field. This figure shows that the NP phase (orange, H_C = 0.1 T) has a substantially lower coercivity compared to the AG-P phase (black, H_C ~ 1.25 T).*

The bulk magnetic and electrical properties of the annealed LSCO thin films are shown in **Fig. 4.11**. The resistivity data was normalized to the thin film volume, while the magnetization data was normalized to 1. In the resistivity measurement, the transition temperature was determined as the temperature where the curve has a local maximum (*i.e.* dR/dT=0) [96,97], while the Curie temperature was determined as the temperature corresponding to the peak in $|dM/dT|$[98]. Using these metrics, the transition temperatures are in good agreement between the two measurements. For the AG-P sample, the M-to-I and FM-to-PM transitions coincide at

T_C~198 K. The oxygen deficiency in the OD-P phase led to a decrease in T_C to 180 K and an increase in resistivity across the entire temperature range studied. The increase in resistivity is most dramatic at low temperatures where an additional insulating phase emerges for temperatures below ~125 K [155,156]. The highly reduced phases (BM, NP, and RP) had room temperature resistivity values several orders of magnitude higher than the perovskite phases. The high resistivity values for the NP and RP phases prevented resistivity measurements at lower temperatures. The BM phase displayed purely insulating temperature dependence and no detectable magnetic signal over the temperature range studied, consistent with the AFM properties reported for BM $SrCoO_{2.5}$ [157]. The weak FM signal from the BM phase measured in the XMCD spectrum (**Fig. 4.7(b)** blue curve) was not detected in the magnetization-temperature plot in **Fig. 4.11(b),** mainly due to the detection sensitivity difference between the two measurements. In addition to the insulating properties, the NP phase displayed FM properties with a nearly constant magnetization value of 847 emu cm^{-3} up to the highest measurement temperature of 370 K. This magnetization value was normalized to the estimated volume of all the Co nanoparticles (*i.e.*, 23% of the total NP film volume, based on XA spectra fitting results), and the measured M_S of these Co nanoparticles corresponds well to the reported value for metallic Co (*i.e.*, M_S = 1352 emu cm^{-3} compared to M_S ~1400 emu cm^{-3} [158,159], respectively). The high T_C value in the NP sample is also consistent with the presence of FM Co nanoparticles embedded within an insulating matrix. The RP phase has a weak FM phase

with low remanent magnetization which appears at temperatures below ~25 K (not shown).

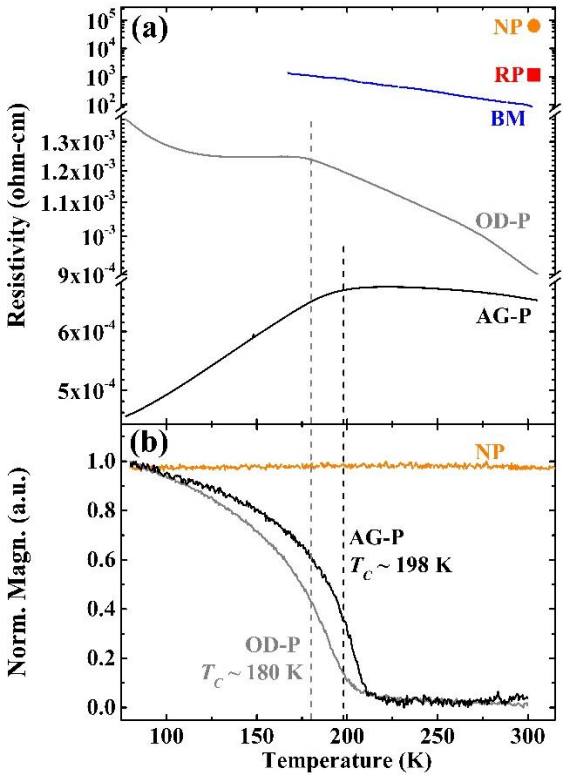

Fig. 4.11*. Film-averaged (a) resistivity and (b) normalized magnetization as a function of temperature for LSCO thin films after reducing anneals. A magnetic field of 0.08 T was applied along the [100] substrate direction during the magnetization measurements. The dashed vertical lines denote the T_C of the AG-P (black, T_C ~ 198 K) and OD-P (gray, T_C ~ 180 K) samples.*

XLD spectroscopy (**Fig. 4.12**) was used to probe the asymmetry between the in-plane <100> and out-of-plane [001] directions in the annealed LSCO thin films, where this asymmetry may

arise from factors such as the charge distribution around the Co ions due to antiferromagnetic (AFM) order, orbital ordering (d_{x2-y2} *vs.* d_{z2} orbitals), and structural asymmetry [67,68]. A structural XLD signal is expected in the BM phase due to the alternating layers of Co ions octahedral/tetrahedral coordination along the *c*-axis. Similarly, a large contribution to the structural asymmetry is expected in the RP phase due to the corner shared CoO_6 octahedra in the *ab*-plane, while they are separated by (La,Sr)O layers along the *c*-axis. While the structural and orbital ordering effects are temperature independent, the identification of the AFM contribution can be made by comparing XLD spectra acquired above and below the Néel temperature (T_N). Pronounced XLD signals were observed on both the RP and BM phases with their own characteristic spectral shapes indicating a potentially different origin in each phase. A much weaker signal was observed for the NP phase, consistent with its polycrystalline nature. While little difference existed in XLD spectra for the RP sample acquired at 300 K and 80 K, a small difference in the spectra for the BM phase enabled a small AFM contribution to be separated from the dominant structural component as shown in **Fig. 4.12**. The AFM XLD spectra show the typical up/down spectral features at the L_3 edge, characteristically found in other AFM perovskite oxides [92,160], and consistent with reports of AFM properties for the BM $SrCoO_{2.5}$ phase [157]. The fact that this BM sample displayed both AFM and FM (**Fig. 4.7(b)**, blue) properties indicates there is a trace of FM Co^{2+} ions embedded in a matrix of the predominant BM coordination.

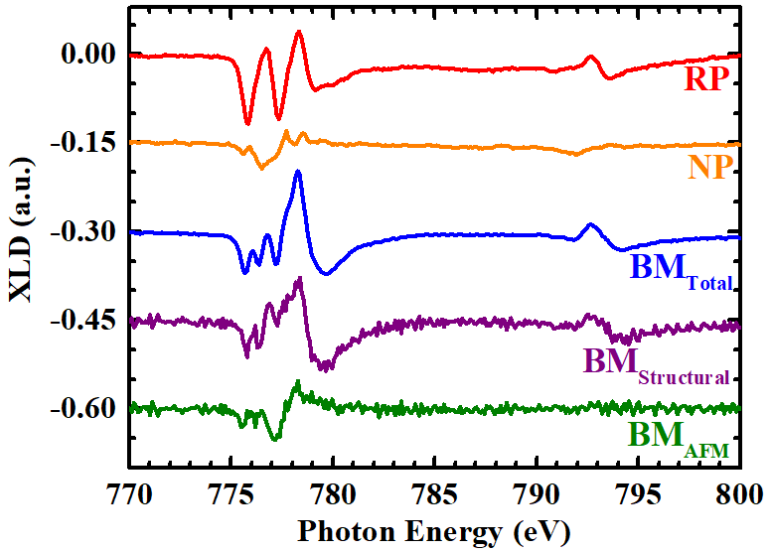

***Fig. 4.12**. Co $L_{3,2}$ XLD spectra for LSCO thin films after reducing anneals. The RP (red), NP (orange) and BM_{Total} (blue) spectra were acquired at 80 K. The structural and AFM dichroism spectra for the BM phase have been separated by comparing spectra acquired at 80 K and 300 K.*

Figure 4.2(a) summarizes the temperature/oxygen partial pressure phase space explored in order to initiate a wide range of topotactic transformations in perovskite LSCO thin films. Under mild reducing conditions ($T \leq 300$°C at 10^{-24} atm P_{O_2}, and 400°C at 10^{-7} atm P_{O_2}), oxygen deficiency resulted in a slight expansion of the perovskite unit cell volume, a change in the magnetic properties (decrease in T_C and M_S), and an increase in the resistivity due to the disruption of the Co^{3+} - O^{2-} - Co^{4+} double exchange network. Increasing the annealing temperature to 400 °C at 10^{-24} atm P_{O_2}, resulted in the formation of the BM phase, which

displayed AFM/I properties with a trace FM signal from Co^{2+} ions. This metastable phase slowly transformed back to the perovskite phase over a period of several months in ambient conditions. Annealing at 600 °C/10^{-12} atm P_{O_2} led to the formation of small Co nanoparticles embedded in a polycrystalline matrix of the RP phase characterized by FM/I properties by low coercivity and an elevated Curie temperature, T_C > 370 K. Notably, this structure was characterized by a dramatic increase in total film thickness (50.5%) and a sharp drop in density (-29.9%) compared to the AG-P thin film. Finally, an epitaxial and homogeneous RP structure ($a = b = 3.868$ Å, $c = 12.89$ Å) was obtained after annealing at the most reducing condition explored (900 °C/10^{-12} atm P_{O_2}). Once formed, this phase remained stable under ambient conditions, and it displayed high resistivity and weak FM properties at temperatures below ~ 25 K with low remanent magnetization.

4.4 Density Functional Theory (DFT) Calculations

4.4.1 Calculations of the RP phase

For the RP phase, two different Sr doping configurations were sampled, each tested with an A-type AFM and G-type AFM ordering. It was found that the doping positions barely influence the results, while G-type AFM is in better agreement with experimental results in terms of lattice parameters and the sample's insulating property. In addition, our first principles phonon

calculations revealed that only the G-type AFM phase is stable at finite temperature. The calculated properties assuming the G-type AFM ordering are shown in **Table 4.3**.

Table 4.3. *Comparison of measured and computed structural, magnetic and electronic properties of the RP phase (with the G-type AFM ordering).*

Structural, magnetic and electronic properties	Experimental RP	Calculated RP (G-type AFM)
Lattice parameters	$a = b = 3.87$ Å* $c = 12.83$ Å	$a = 3.87$ Å $b = 3.89$ Å $c = 12.77$ Å
Net magnetic moment	Weak FM under 25 K	0.25 μB/Co = 24 emu cm^{-3}
Band gap	Insulating	0.37 eV (insulating)

* equivalent to the LSAT substrate lattice parameter, as the film was epitaxially grown.

4.4.2 Calculations of the vacancy formation energy in the BM phase

Either one cobalt or one oxygen atom (neutral charge) from the 36-atom BM cell was removed, and tested two symmetric inequivalent positions for each species. For cobalt, the vacancy positions at both the octahedral site and the tetrahedral site were tested, and it is found that the vacancy formation energy is lower at the octahedral site. For oxygen, two vacancy positions were tested: one that bridges the octahedral and tetrahedral unit, and an additional one between the octahedral units; it is found that the former position leads to a lower vacancy formation energy. The lowest vacancy formation energy obtained for each species is reported in **Table 4.4**.

The vacancy formation energy E_{vac_i} for species i is calculated using the following equation:

$$E_{vac\_i} = E_d - E_p + n_i\mu_i \quad \textbf{(4.1)}$$

where E_d and E_p are the total energies of the defective structure and pristine BM structure, respectively, n_i is the number of removed atoms of species i (equals to 1 in this case), and μ_i is the chemical potential of species i that is in equilibrium with the environment.

$$\mu_O = \frac{1}{2}\mu_{O_2} = E_{O_2}^{total} + kTln(\frac{p}{p^0}) \quad \textbf{(4.2)}$$

where $E_{O_2}^{total}$ is the DFT-calculated energy of an O_2 molecule in the triplet ground state, k is the Boltzmann constant, T and p are the temperature and pressure of the oxygen in the environment and p^0 equals to 1 atm. By changing the annealing condition, μ_{O_2} and the oxygen vacancy formation energy are essentially changed. This gives: $\Delta\mu_{O_2} = -2.072$ eV for the NP sample (annealed at 600 $^oC/10^{-12}$ atm), and $\Delta\mu_{O_2} = -2.791$ eV for the RP sample (annealed at 900 $^oC/10^{-12}$atm), with respect to μ_{O_2}at standard state (25 ^oC/1 atm).

For Co, similarly that $\mu_{Co} = E_{Co}^{total}$, except here μ_{Co} is not influenced by the annealing

conditions. $E_{\mathrm{Co}}^{\mathrm{total}}$ is the DFT-calculated energy of cobalt in the ground-state crystal structure (*P6₃/mmc* space group).

Table 4.4. *Calculated chemical potential change and vacancy formation energy for cobalt and oxygen in the BM phase*

Chemical potential change and vacancy formation energy	Standard state (25 °C/1 atm)	NP sample (600 °C/10^{-12} atm)	RP sample (900 °C/10^{-12} atm)
$\Delta\mu_{O_2}$ (eV)	0	-2.072	-2.791
$E_{\mathrm{vac\_O}}$ (eV)	2.51	1.48	1.12
$E_{\mathrm{vac\_Co}}$ (eV)	1.14	1.14	1.14

4.5 Conclusion

In summary, a series of topotactic transformations involving the loss of both oxygen anions and cobalt cations were observed in $La_{0.7}Sr_{0.3}CoO_{3-\delta}$ thin films upon annealing under highly reducing conditions. First principles calculations were conducted to interpret experiments and characterize the observed phases. These phases not only include the oxygen-deficient perovskite and BM phases, but the RP phase which has been rarely reported in the cobaltite topotactic transformations and requires the loss of cobalt cations. A composite phase consisting of FM Co nanoparticles embedded in an insulating RP matrix was observed at an intermediate annealing condition of 600 °C/10^{-12} atm P_{O_2}. These Co nanoparticle precipitates re-dissolved

into the oxide matrix upon annealing, forming interstitial Co ions in the RP phase under the most reducing condition investigated. DFT calculations further confirmed that the formation of the RP phase and Co nanoparticles is thermodynamically possible, and the calculated structural, magnetic and electronic properties supported the experimental measurements. Each structure possessed its own distinct set of physical properties including FM/M, AFM/I, and two types of FM/I phases. The ability to control the physical properties by movement of ion migration suggest their potential for further exploration into the reversibility and order parameter tuning by electric fields for applications such as neuromorphic devices.

Chapter 5: Quantification of Oxygen Deficiency in Cobaltite Thin Films

5.1 Introduction

Oxygen deficiency within ionic materials is a tunable parameter that can lead to substantial modification to the material's physical and functional properties. As a result, tailoring oxygen vacancy distributions have the potential to enable the design of novel emerging applications such as magnetoionic switches [15,43,44,161-165] and next-generation memory and logic devices [1,166,167]. Among the wide variety of ionic crystals, perovskite oxides with the chemical formula ABO_3 and the related perovskite-like structures are of particular interest because of their wide range of functional properties and high oxygen ion conductivities [42,168]. Previous studies on these materials have focused on the impact of the *A* and *B*-site stoichiometry [115,116], however recent studies have turned to the oxygen stoichiometry/deficiency as an additional degree of freedom for designing the device applications [13-15]. The Sr-doped lanthanum cobaltite $La_{0.7}Sr_{0.3}CoO_{3-\delta}$ (LSCO, where δ is the oxygen deficiency and $0 \leq \delta < 0.5$) is an ideal system for investigating oxygen deficiencies due to its high oxygen conductivity, relatively low oxygen vacancy formation energy [124], and strong coupling of the magnetic and electronic properties to the oxygen deficiency. At this 30% Sr-doping level, the perovskite phase is the equilibrium phase, characterized by coincident metal (M)-to-insulator (I) and ferromagnetic (FM)-to-paramagnetic transitions at the Curie temperature, $T_C \sim 240$ K [123].

Titration methods have been used in the past for quantifying the oxygen stoichiometry/deficiency in bulk perovskite materials [169-171]. For cobaltites, iodometric titration is based on the reduction of Co^{4+} and Co^{3+} ions to Co^{2+} ions in the material. The number of electrons that can be accepted by the material provides the average valence state of Co, and the oxygen stoichiometry can then be indirectly derived by electroneutrality. Other methods used to determine oxygen deficiency in bulk oxides include measuring the out-of-plane lattice parameter of the material. In perovskites, the out-of-plane lattice parameter is assumed to be a key index to oxygen deficiency [172,173], *i.e.*, the lattice parameter is generally larger when oxygen vacancies are present in the material. This chemical expansion was found to be the result of lattice expansion around an oxygen vacancy (primarily due to electrostatic interactions, *i.e.*, the repulsion of the cations of same charge), in addition to the lattice expansion from the change in the cation radius (primarily due to steric effects) [174-176]. For example, oxygen vacancies donate electrons to the empty 3*d*-orbitals of the *B*-site ions, reducing the valence state of the ion and increasing its ionic radius. The correlation between the lattice parameter and the oxygen deficiency in bulk nonstoichiometric compounds have been experimentally investigated [177-179].

Unlike bulk materials, it is difficult to quantify the absolute oxygen deficiency in thin films

since the underlying oxide substrate would affect the titration process and yield inaccurate results. The previously determined relationships between the lattice parameter and the oxygen deficiency in bulk materials are not directly applicable to thin films due to the epitaxial strain induced by the single crystal substrate. For the same amount of oxygen deficiency, the out-of-plane lattice parameters of a thin film material could differ when grown on different substrates where the Poisson's effect should be considered depending on whether the film is experiencing tensile or compressive strain. A limited number of reports exist in the literature combining experimental measurements and theoretical calculations [180] to quantify the oxygen deficiency in thin films, and the resulting impact on the functional properties.

In this chapter, LSCO thin films were annealed under reducing conditions to reach a series of films with the perovskite structure with varying oxygen deficiency. The anneals were performed using either a Mg-trap annealing system [125] or a gas evolution system [126] which enabled the exploration of wide temperature/oxygen pressure phase space ranging from room temperature to 400 °C and oxygen partial pressures (P_{O_2}) from 10^{-26} to 10^{-1} atm. X-ray diffraction (XRD) confirms the out-of-plane lattice parameter increases with increasing annealing time or decreasing annealing P_{O_2}. To quantify the amount of oxygen vacancies, soft x-ray absorption (XA) spectroscopy measurements at the cobalt *L*-edge and oxygen *K*-edge were acquired and density functional theory (DFT) calculations were performed. However, the

small changes in the Co valence states made it difficult to observe any major changes to the Co *L*-edge spectra. Instead, oxygen *K*-edge spectra suggested that peak separation between certain XA spectral features can be used as a fingerprint to quantify the oxygen deficiency. The magnetization and resistivity of the LSCO films decreases and increases with increasing concentration of oxygen vacancies, respectively, due to the expansion of the lattice and the disruption of the double exchange mechanism between the cobalt and oxygen ions [48,129]. The ability to control the physical properties by tuning the oxygen deficiency suggest the potential for future applications such as neuromorphic devices.

Throughout this chapter, the LSCO thin films were annealed by Dr. Min-Han Lee at the University of California, San Diego, and Michael Taejoon Park at Purdue University. The first principles calculations were performed by Dr. Shenli Zhang at the University of Chicago.

5.2 Experimental Methods

Epitaxial LSCO thin films (thickness ~ 23 nm) were deposited on (001)-oriented $(LaAlO_3)_{0.3}(Sr_2TaAlO_6)_{0.7}$ (LSAT) substrates by pulsed laser deposition with a laser pulse frequency of 1 Hz and laser fluence of ~ 0.8 J cm^{-2}. During the oriented growth, the substrate temperature was held at 700 °C and the oxygen pressure was 300 mTorr. The films were cooled slowly to room temperature after the deposition with an oxygen pressure of 300 Torr to ensure

proper oxygen stoichiometry. The LSCO films were annealed either in a gas evolution system which consists of a tube furnace connected to a high vacuum system capable of achieving P_{O_2} from 10^{-12} to 0.1 atm and temperatures up to 1000 ºC [126], or a Mg-based oxygen trap system capable of achieving P_{O_2} down to 10^{-26} atm and temperatures up to 400 ºC [125]. In this system, Mg powder is heated and reacted with trace amount of molecular oxygen in ultrahigh purity argon gas.

The structural properties of the films were characterized by high-resolution XRD using a Bruker D8 Discover four-circle diffractometer with Cu $K_{\alpha 1}$ x-rays. A Lakeshore cryogenic probe station was used to measure the film resistivity upon warming from 80 K with the van der Pauw geometry. The bulk magnetic properties were measured using a Quantum Design VersaLab vibrating sample magnetometer (VSM) with the magnetic field applied along the in-plane [100] substrate direction. XA spectra at the O *K*-edge was performed at 80 K and room temperature at beamline 4.0.2 at the Advanced Light Source (ALS) using total electron yield detection (TEY, which provides surface sensitive measurements to the top 5-10 nm of the sample [63]), total fluorescent yield (TFY, which probes the bulk of the film), and luminescence yield (LY, which probes the full film thickness[63]). Soft x-ray magnetic spectroscopy at the Co *L*-edge was performed at 80 K at beamline 6.3.1 at the ALS using TEY detection mode. For all of the XA spectra measurements, the x-rays were incident upon the sample at a 30° grazing

angle along the in-plane [100] substrate direction.

For DFT calculations, two sets of supercells were used to simulate five δ values, where a $\sqrt{2} \times \sqrt{2} \times 4$ perovskite unit ($La_5Sr_3Co_8O_{24-n}$, $\delta = n/8$) was used for $\delta = 0$, 0.125 and 0.25, and a $2\sqrt{2} \times 2\sqrt{2} \times 4$ perovskite unit ($La_{20}Sr_{12}Co_{32}O_{96-n}$, $\delta = n/32$) was used to obtain smaller δ values of 0.03 and 0.0625. The ground state structure for $\delta = 0$, 0.125 and 0.25 was obtained in previous calculations [129], which have been validated against available experimental data, including structural deformation, magnetic state transition and band gap opening as a function of oxygen vacancy concentrations (V_{Oxy}). The ground state charge density and wavefunctions were obtained with the QUANTUM ESPRESSO (QE) code (V6.4) [127,128], which solves the Kohn-Sham equations of DFT using plane waves and pseudopotentials. In particular, DFT + U ($U = 3$ eV, as justified in previous calculations [129]) was used, with the Perdew-Burke-Ernzerhof (PBE) exchange-correlation functional [130] and projected augmented wave (PAW) pseudopotentials from the PSlibrary [131] (v1.0.0 for La, Sr and O and v0.3.1 for Co). The plane-wave cutoff was set to 90 Ry and Monkhorst-Pack k-point grid was used with resolution ~ 0.03 $Å^{-1}$.

XA spectra were calculated using OCEAN code (V2.9.6.3) [181,182], which utilizes QE for ground-state DFT calculations and then solves Bethe-Salpeter equation (BSE) to obtain the

core-level spectra. Besides the convergence in DFT calculations, the convergence in the core-level spectra calculations was verified with respect to the number of bands and *k*-points used for screening and the final states wave-functions calculations. OCEAN uses optimal projector functions to obtain the core wavefunctions from pseudopotentials. Since the version used here does not allow for PBE core wavefunctions and is not compatible with PAW pseudopotentials, local-density approximations (LDA) core wavefunctions was used and Optimized Norm-Conserving Vanderbilt (ONCV) pseudopotentials (ONCVPSP-PBE-PDv0.4 from PseudoDojo) [183,184] was adopted for spectra calculations. The difference between LDA and PBE core wavefunctions was verified to cause negligible effects on the obtained spectra using a different XAS calculation code Xspectra [185,186] implemented in QE. Core-level binding energy shift was enabled for spectra calculations to obtain a correct alignment among the obtained spectra of various samples.

5.3 Results and Discussion

The as-grown perovskite (AG-P) LSCO samples were annealed in four different reducing conditions to reach the oxygen-deficient perovskite (OD-P) phases. The four samples after anneals are denoted as OD-P-1', OD-P-2', OD-P-3', and OD-P-4', and their corresponding annealing conditions are listed in **Table 5.1**. Analysis of ω-2θ XRD curves (**Fig. 5.1(a)**) provides the structural information of the films after each reducing anneal. The film peaks

shifted to lower 2θ values compared to the AG-P phase, corresponding to an increase in the lattice parameter as summarized in **Table 5.1**.

These OD-P films were not stable in air and gradually reverted back to the equilibrium perovskite phase over a period of several months, presumably by the reincorporation of oxygen ions from the ambient even at room temperature. As a result, XRD measurements were repeated immediately before each subsequent measurement to determine the structural properties at that particular time. The samples denoted as OD-P-1' and OD-P-2' are now referred to as OD-P-1 and OD-P-2, respectively, and their lattice parameters are now only ~ 0.1% larger than that of AG-P, as shown in **Table 5.2**. Similarly, samples OD-P-3' and OD-P-4' are now denoted as OD-P-3 and OD-P-4, where both of their lattice parameters have decreased towards that of the AG-P sample (**Fig. 5.1(b), Table 5.2**). From AG-P to OD-P-4, the increasing lattice parameters indicate the increasing oxygen deficiency (δ) in the films [174-176], where their absolute δ will be further discussed below.

Table 5.1. *The annealing conditions to drive the LSCO films from AG-P to OD-P phase and the resulting lattice parameters of the OD-P phases. The lattice parameter change is calculated compared to the original AG-P sample (not annealed).*

Sample	Annealing conditions	Lattice parameter	Lattice parameter change
AG-P	Not annealed	3.790 Å	0%
OD-P-1'	400°C / 10^{-7} atm P_{O_2} / 1 hr	3.800 Å	0.26%
OD-P-2'	400°C / 10^{-12} atm P_{O_2} / 10 mins	3.840 Å	1.32%
OD-P-3'	300°C / 10^{-24} atm P_{O_2} / 1.5 hrs	3.842 Å	1.37%
OD-P-4'	300°C / 10^{-26} atm P_{O_2} / 1 hr	3.857 Å	1.77%

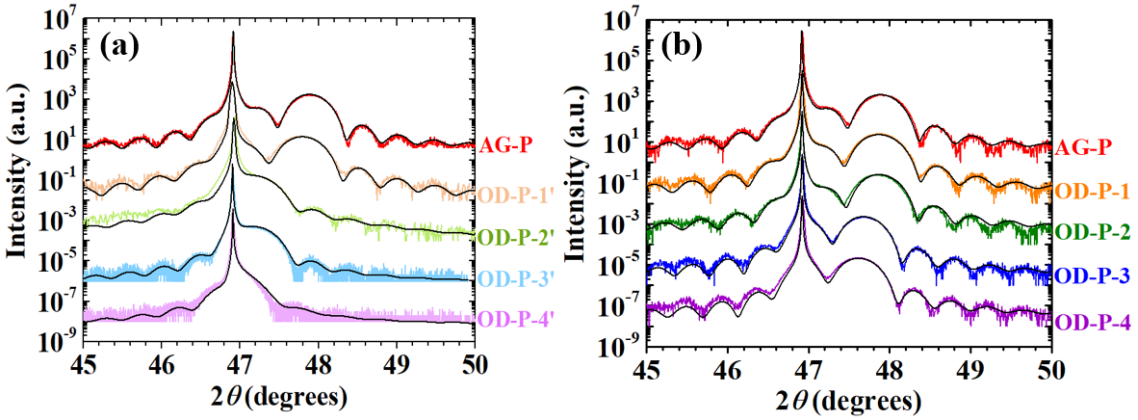

Fig. 5.1. *XRD curves of the AG-P and OD-P LSCO films (a) after the initial reducing anneals and (b) three months after the initial anneals. The thin black curves in both panels are the fitted XRD curves.*

***Table 5.2**. The lattice parameters of the OD-P LSCO films three months after the initial anneals. The lattice parameter change is calculated compared to the original AG-P sample (not annealed). The metal-insulator transition (MIT) temperature for each sample is also included.*

Sample	Lattice parameter	Lattice parameter change	MIT temperature
AG-P	3.790 Å	0%	207 K
OD-P-1	3.793 Å	0.08%	207 K
OD-P-2	3.795 Å	0.13%	206 K
OD-P-3	3.808 Å	0.48%	–
OD-P-4	3.812 Å	0.58%	–

Oxygen deficiency plays a large role in determining the physical properties of the films, such as the resistivity and magnetism. The bulk electrical properties of the annealed LSCO thin films are shown in **Fig. 5.2**. The resistivity data was normalized to the thin film volume, and the metal-insulator transition (MIT) temperature for samples AG-P, OD-P-1 and OD-P-2 (**Table 5.2**) was determined as the temperature where the curve has a local maximum (*i.e.*, $dR/dT = 0$) [96,97]. The AG-P sample has the lowest resistivity compared to the OD-P-1 and OD-P-2 samples, although all three samples show the M-to-I transition at ~ 198 K. On the other hand, the oxygen deficiency in the OD-P-3 and OD-P-4 samples leads to an increase in resistivity (the resistivity of OD-P-4 is four times larger than that of AG-P at room temperature) across the entire temperature range studied, as well as a change in the shape to purely semiconducting behavior with increasing resistivity as temperature decreases. This behavior is ascribed to the oxygen vacancies preventing the electrons from hopping between Co^{3+} and Co^{4+}

ions according to the double-exchange mechanism.

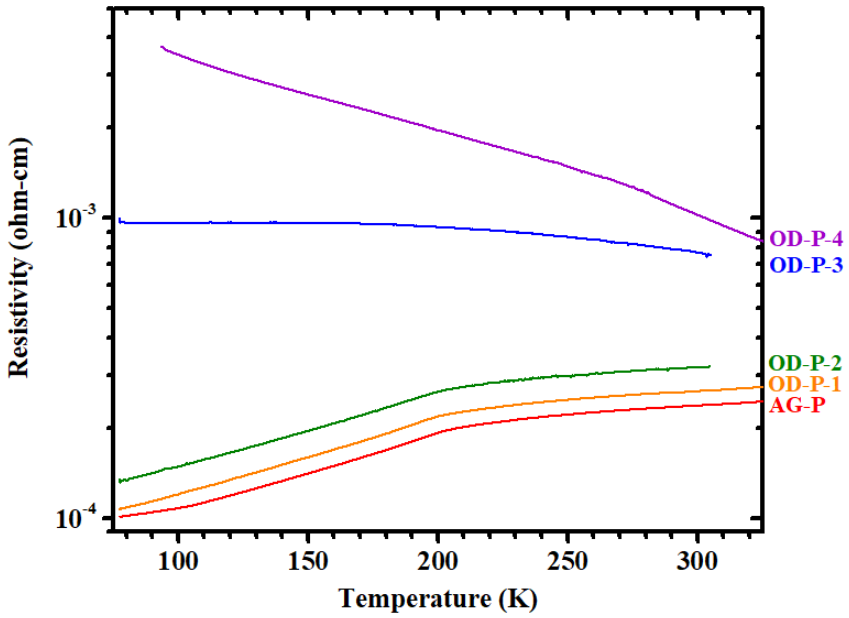

***Fig. 5.2**. Film-averaged resistivity as a function of temperature for LSCO thin films after reducing anneals.*

Co *L*-edge XA spectra (**Fig. 5.3**) were acquired in order to detect any change in Co valence state and local coordination associated with the reducing anneals. The AG-P sample agrees with literature data for mixed valence Co^{3+}/Co^{4+} ions in octahedral coordination [148,149]. The XA spectral shape of the OD-P-1 and OD-P-2 samples shares the same spectral features and peak intensities to that of the AG-P sample due to their similar lattice parameters as indicated by the XRD measurements, confirming that the Co ion ratio is essentially the same between these three samples. In contrast, the OD-P-3 and OD-P-4 samples have slightly less well-defined spectral features at the Co-L_3 edge, indicating more oxygen vacancies are present in these two

samples [187]. Compared to the AG-P sample, the average valence state of OD-P-3 and OD-P-4 is lower as their XA spectral peak shapes are closer to the $LaCoO_3$ spectra (as shown in **Fig. 5.3**), indicating the increased proportion of Co^{3+} ions in the Co^{3+}/Co^{4+} mixed valence states upon annealing. As shown in **Fig. 5.4**, the bulk hysteresis loops show that the saturation magnetization (M_S) decreases with increasing lattice parameter and increasing oxygen deficiency. Compared to AG-P, the M_S value of samples OD-P-3 and 4 decreased by 10% and 22%, respectively, as the oxygen vacancies break up the Co^{3+} - O^{2-} - Co^{4+} double exchange network [150,151]. For samples OD-P-3 and 4, the coercive field (H_C) decreases as the lattice parameter increases (*i.e.*, the oxygen deficiency increases). The slightly larger H_C values for samples OD-P-1 and OD-P-2 compared to the AG-P sample may be attributed to defects in the films pinning the local magnetic moments [188-190], as these two samples underwent oxygen removal and re-introduction processes while the AG-P sample did not. The oxygen vacancies in the films lead to degraded ferromagnetic properties, consistent with the increased resistivity and change in the temperature dependence. In particular, the resistivity behavior shows a much more dramatic impact that the magnetization for samples OD-P-3 and 4.

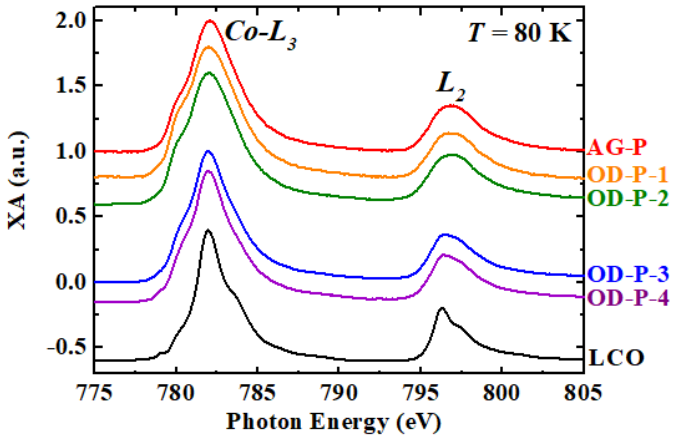

***Fig. 5.3**. Co-$L_{3,2}$ XA acquired at 80 K with TEY detection mode for LSCO thin films after reducing anneals. The reference spectrum for Co^{3+} ions in octahedral coordination ($LaCoO_3$, black) is also included.*

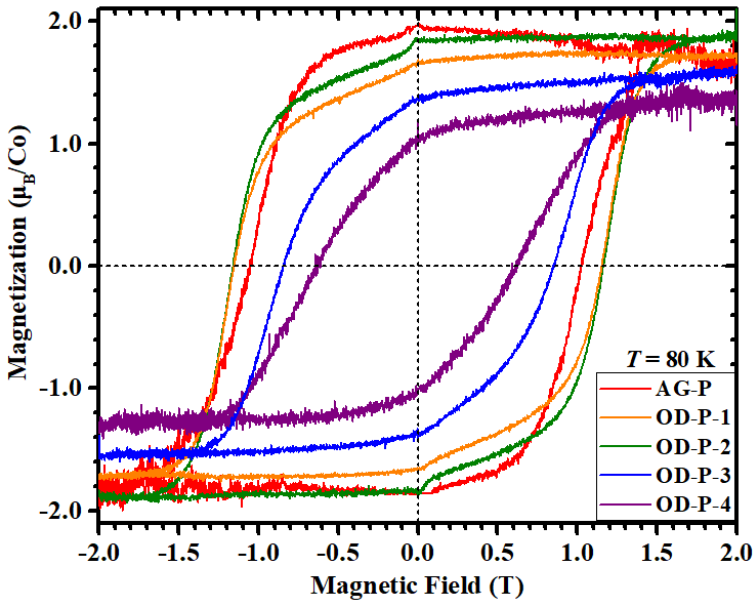

***Fig. 5.4**. Co bulk hysteresis loops acquired at 80 K for LSCO thin films after reducing anneals.*

To effectively quantify the concentration of oxygen vacancies in these oxygen-deficient samples, O *K*-edge XA spectra were experimentally acquired (**Fig. 5.5(a)** dashed lines) and

compared with calculated spectra from DFT simulations (**Fig. 5.5(a)** solid lines) based on the oxygen deficiencies ranging from $\delta = 0$ to $\delta = 0.25$. Two main peaks were identified within the range between 528 and 540 eV for both measured and calculated spectra (marked as peaks 1 and 2 in **Fig. 5.5(a)**). Peak 1 is at ~ 530 eV for both experimental and calculated curves, while peak 2 is at ~ 538 eV for the experimental curves and at ~ 537 eV for the DFT simulated curves. For the simulated spectra, the $\delta = 0$ supercell was aligned to the experimental AG-P sample with respect to peak 1. The absolute peak positions vary between experimental and calculated spectra, likely due to the differences in measurement temperatures and/or the detection modes used in experiments, and the level of theory used to compute the spectra. The energy resolution in the experimental spectra could also affect the peak width and the number of the observed peaks.

The effects of the detection mode (TEY, LY and TFY) and the sample temperature on the features of the XA spectra were investigated. It is noted that under the same incident angle (30°) and at 300 K, the peak at ~531.7 eV only appears for measurements carried out in TFY and LY modes but not in TEY mode (**Fig. 5.6(a)**). This suggests that the feature is a bulk feature, not confined to the surface of the LSCO film. Furthermore, it is verified that this peak does not overlap with any LSAT substrate signal and is thus not expected to originate from the substrate. Instead, it is likely a genuine absorption feature involving hybridized La 5*d*-O 2*p* orbitals. As

the chemical composition at the surface could be different from that of the bulk (Sr segregation has been reported at cobaltite interfaces [191]), the hybridized La 5*d*-O 2*p* orbitals may not contribute significantly in the TEY mode. On the other hand, the measurement temperature could affect the XA spectral shape as a larger number of peaks are observed at 80 K than at room temperature (**Fig. 5.6(b)**). Such temperature effects are more significant for higher values of δ.

As shown in the XA spectra in **Fig. 5.5(a)**, the intensity of peak 1 decreases with increasing oxygen deficiency in both the experimental and simulated O *K*-edge XA spectra. In addition, as δ increases, peak 1 moves to higher energies while peak 2 moves to lower energies, decreasing the energy separation between these two peaks. The change of the peak separation between peaks 1 and 2 for a given sample strongly depends on the oxygen deficiency in the film. In both the experimental and calculated oxygen *K*-edge XA spectra, the peak separation between peaks 1 and 2 decreases with increasing δ value, or equivalently with the increasing annealing time/decreasing annealing P_{O_2}.

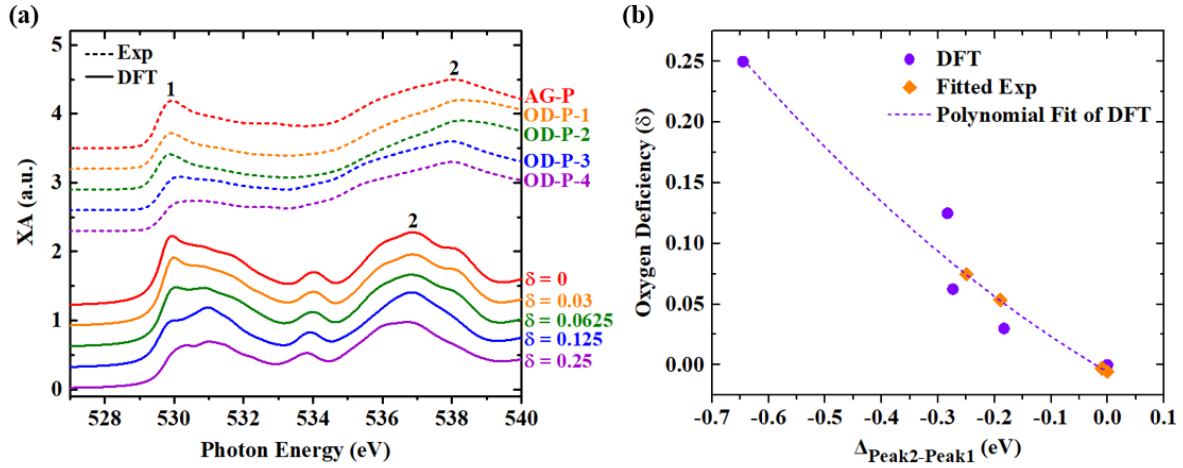

Fig. 5.5*. (a) Experimental (top series, dashed lines) and calculated (bottom series, solid lines) oxygen K-edge spectra at room temperature (300 K). The experimental data was collected using the TEY detection mode. The calculated curves were based on various oxygen deficiency (δ) in the films. The peaks used to calculate the peak separations are denoted as 1 and 2. (b) The change in the peak separation between peaks 1 and 2 ($\Delta_{Peak2\text{-}Peak1}$) from the DFT calculations was plotted as a function of δ (violet data points). These data points were best fit with a second-order polynomial relationship (violet dashed curve). The change in peak separation from the experimental measurements were fit to this polynomial curve to determine the value of δ (orange data points). The fitting range is valid for low δ values ($0 \leq \delta \leq 0.25$) before oxygen deficiency induces structural phase changes in the films.*

Table 5.3. *Fitting parameters of the second-order polynomial curve in* ***Fig. 5.5(b)***

Equation	y = Intercept + $a_1x + a_2x^2$
Intercept	-0.0056
a_1	-0.2714
a_2	0.1974
R^2	0.8804

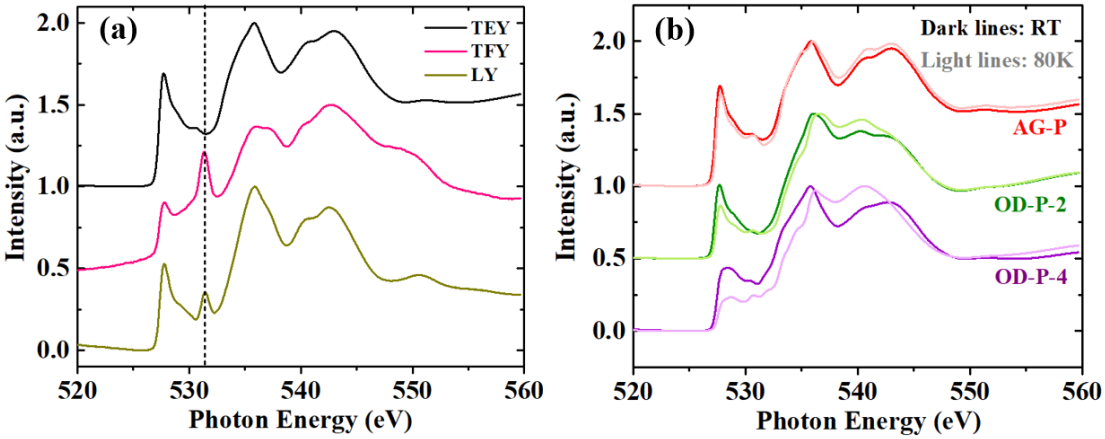

Fig. 5.6. *O K-edge XA spectra of the (a) AG-P sample measured using TEY, TFY, and LY detection modes at room temperature and (b) AG-P, OD-P-2 and OD-P-4 samples measured using TEY detection mode at room temperature (dark lines) and 80 K (light lines). All the spectra in (a) and (b) were measured at 30° grazing incident angle. In (a), the second main peak (denoted by the black line) only appears in TFY and LY mode but not in TEY mode. In (b), finer structures are detected at 80 K than at room temperature, and this effect is more significant in samples with higher oxygen vacancy content.*

The change in the peak separation between peaks 1 and 2 ($\Delta_{Peak2\text{-}Peak1}$) was determined relative

to that of the calculated δ=0 case and plotted as a function of δ (**Fig. 5.5(b)** violet data points). This data was best fit with a second-order polynomial equation (violet dashed curve) with an R^2 value of 0.88. The fitting parameters for the polynomial curve are listed in **Table 5.3**. The change in peak separation from the experimental measurements were fit to this polynomial curve to determine the value of δ, as shown in **Fig. 5.5(b)** orange data points. To check the relationship between δ and out-of-plane lattice parameter, **Fig. 5.7** plots the obtained δ values for the experimental data as a function of the percentage change in the out-of-plane lattice parameter (relative to the AG-P sample). The computational data points are consistent with the experimental data for δ below 0.04, however, when δ is larger than 0.05, a slight deviation is observed with the experimental data showing higher values by 70%, revealing that the out-of-plane lattice parameter and δ may have a non-monotonic dependence.

To understand the relationship between δ and the out-of-plane lattice parameter, two defective bulk structures were created with the same value of δ (= 0.0625): one with two separate pyramidally-coordinated Co atoms and the other one with both tetrahedrally and pyramidally-coordinated Co atoms (**Fig. 5.8**). The δ = 0.0625 is chosen as it corresponds to the minimum oxygen vacancy numbers (*i.e.*, two) required to form different local defect structures in the largest supercell; the largest supercell is chosen to minimize the interaction between an oxygen vacancy and its image due to periodic boundary conditions. Despite the fact that these two

structures possess the same δ value, their lattice parameters vary due to different geometrical arrangement of the oxygen vacancies in the structures. This result suggests the out-of-plane lattice parameter is not a unique function of δ, and is likely to depend on the geometrical arrangements of oxygen vacancies.

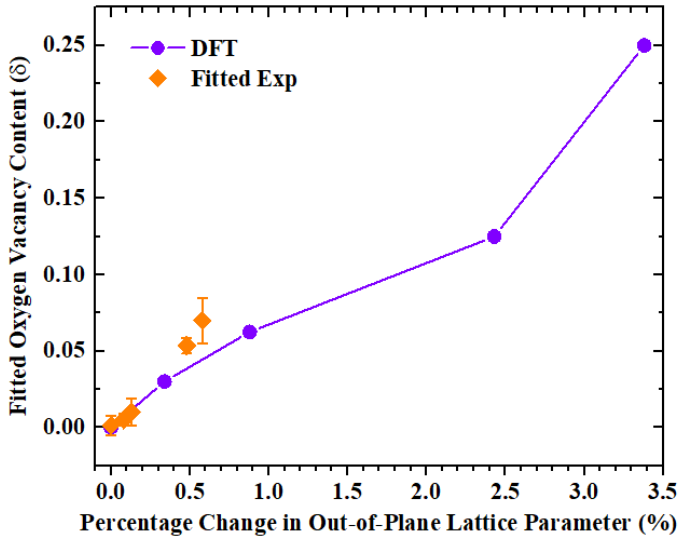

Fig. 5.7. *The estimated δ from* ***Fig. 5.5(b)*** *plotted as a function of the percentage change in out-of-plane lattice parameter (relative to the AG-P phase). The estimated δ from experiment (orange) and the calculated δ from DFT (violet) generally correspond to each other for δ below 0.04.*

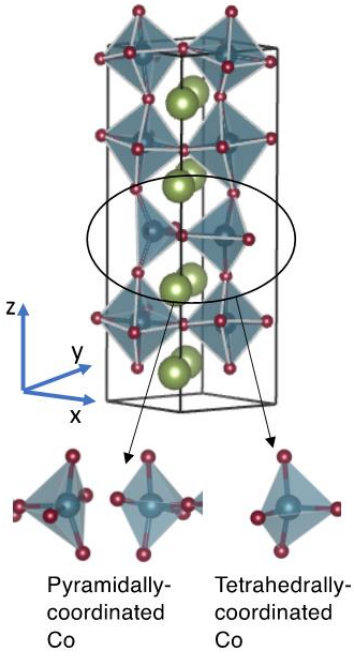

Fig. 5.8*. Example of a defective LSCO model, where the local defect structure can be either composed of pyramidally-coordinated or tetrahedrally-coordinated Co atoms. The blue spheres signify Co ions, red spheres O ions, and green spheres La/Sr ions.*

Compared to the change in the out-of-plane lattice parameter, the peak separations in O *K*-edge XA spectra could be a relatively promising approach of determining the oxygen deficiency in the samples. To test this hypothesis, the magnetization as a function of δ is plotted in **Fig. 5.9**. The experimental curves obtained based on the M_S in the bulk hysteresis loops (**Fig. 5.4**) from samples AG-P, OD-P-1, OD-P-2, OD-P-3 and OD-P-4 were compared with the computed magnetization (**Fig. 5.9** violet) from DFT calculations. The general agreement in the two magnetization curves as a function of δ suggests that the δ estimation based on $\Delta_{Peak2\text{-}Peak1}$ is a reliable method to quantify the oxygen deficiency in the LSCO films.

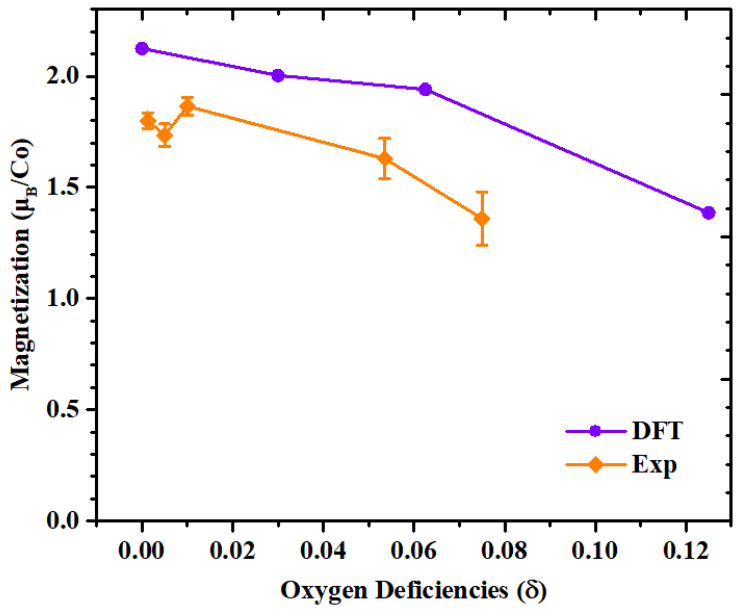

Fig. 5.9. *Magnetization as a function of oxygen deficiency δ. The δ values in the experimental curve (orange) were determined based on the XA spectral feature separation in* ***Fig. 5.5****.*

5.4 Conclusion

Compared to bulk materials, it has been challenging to quantify the oxygen deficiency in thin films grown on single crystal oxide substrates due to the induced epitaxial strain and the difficulty in performing titration measurements on thin films grown on oxide substrates. In this chapter, oxygen *K*-edge XA spectra were acquired to quantify the absolute δ values in $La_{0.7}Sr_{0.3}CoO_{3-\delta}$ thin films with different oxygen deficiency ($0 < \delta < 0.25$) obtained after exposure to anneals under reducing conditions. The combination of experimental results with DFT calculations allowed us to identify that the change in the peak separation between peaks 1 and 2 in the oxygen *K*-edge XA spectra is a reliable feature to determine the δ values

in the LSCO films. With increasing δ, the out-of-plane lattice parameter increases, causing the magnetization and the resistivity of the films to decrease and increase, respectively, as oxygen vacancies break up the Co^{3+} - O^{2-} - Co^{4+} double exchange network. The ability to control the physical properties by tuning the oxygen vacancies suggests the potential for further exploration into the order parameter tuning by electric fields for applications such as neuromorphic devices.

Chapter 6: Cation and Anion Topotactic Transformations in $LaCoO_{3-\delta}$ and $La_{0.7}Sr_{0.3}FeO_{3-\delta}$ Thin Films Leading to Oxygen-Deficient Phases

6.1 Introduction

Although historically antiferromagnetism has been difficult to harness for practical applications, recent developments suggest this may soon be about to change as the antiferromagnets produce no stray fields and are stable to external magnetic field perturbations due to the antiparallel ordering of magnetic moments and zero net magnetization. These advantages make antiferromagnets attractive candidates for future spintronic applications. For example, Wadley *et al.* successfully demonstrated electrical writing and readout between stable configurations in antiferromagnetic (AFM) CuMnAs thin-film devices by applying a current [192]. Furthermore, AFM materials may enable intrinsically faster device operation compared to their ferromagnetic (FM) counterparts due to high-frequency magnons [193-195], and AFM domain walls have been shown theoretically to approach relativistic speeds [196]. The ultrafast spin-dynamics in the THz frequency range offers the prospect of novel non-volatile and rapid memory technologies [196].

For AFM spintronics involving transition metal oxides, their functional properties can be sensitively manipulated by a variety of external stimuli such as lattice strains and applied magnetic/electric fields [197]. For instance, bulk lanthanum cobaltites ($LaCoO_{3-\delta}$, or LCO,

where δ is the oxygen deficiencies) are stable as high-spin state G-type AFM insulators [198]; when grown under tensile strain, the LCO single-crystalline thin film is a rare undoped perovskite with ferromagnetic (FM)/insulating (I) properties and a Curie temperature (T_C) of up to 90 K [198-200].

The family of Sr-doped lanthanum ferrites (*i.e.*, $La_{1-x}Sr_xFeO_{3-\delta}$) are another G-type AFM insulator with the Néel temperature (T_N) decreasing with increasing Sr-doping level, x. The AFM spin axis in bulk LSFO lies along the crystallographic a axis [201] while its orientation in thin films is sensitive to factors such as the film thickness, strain state, substrate orientation, and growth method [92,160,202,203]. When grown epitaxially on $SrTiO_3$ (STO) substrates, $La_{1-x}Sr_xFeO_{3-\delta}$ thin films experience a small compressive strain and exhibit four types of AFM domains, where their spin axes cant out-of-plane by ~ 30° with an in-plane projection along the <100> substrate directions [70,204]. Other studies show that the locations of AFM domains in LSFO thin films are strongly influenced by the presence of local defects which pin the domain walls [205].

The perovskite LCO and LSFO are also ideal systems for investigating phase transformations due to the high oxygen vacancy conductivity (the ionic conductivity of LCO is 0.32 S/cm at 1115 K (842°C) [206] and that of LSFO is 0.20 S/cm at 1223 K (950°C) [207]). In addition,

both LCO and LSFO have relatively low oxygen vacancy formation energy and the multitude of related phases such as the Grenier (GN, $ABO_{2.7}$), brownmillerite (BM, $ABO_{2.5}$), and Ruddlesden-Popper (RP, $A_{n+1}B_nO_{3n+1}$ where n = integer) [50,114] phases (**Fig. 6.1**). This chapter investigates the evolution of the physical properties of LCO and LSFO thin films upon exposure to highly reducing environments, where the anneals were performed using a gas evolution system [126], enabling the exploration of wide temperature/pressure phase space ranging from room temperature to 900 °C and oxygen partial pressures from 10^{-12} to 0.1 atm. X-ray diffraction (XRD) and x-ray reflectivity (XRR) results suggest that the films have experienced substantial structural modifications upon annealing in reducing environments. The LCO thin films experienced transformations from GN, BM, and RP phases while the LSFO merely stayed in the form of oxygen-deficient perovskite phases. As a result, the magnetic property of LCO changed from AFM to FM while that of LSFO remained AFM after the annealing treatments. The x-ray absorption (XA) spectroscopy showed a change of the Co (Fe) local coordination from octahedrally-coordinated Co^{3+} (Fe^{3+}/Fe^{4+}) ions in the perovskite phase to Co^{2+}/Co^{3+} (Fe^{3+}) ions in the reduced phases. In both systems, the room temperature resistivity spanned multiple orders of magnitude upon annealing. The strong correlation of the magnetic and electronic properties to the crystal structure highlights the potential of utilizing ion migration as a basis for emerging applications.

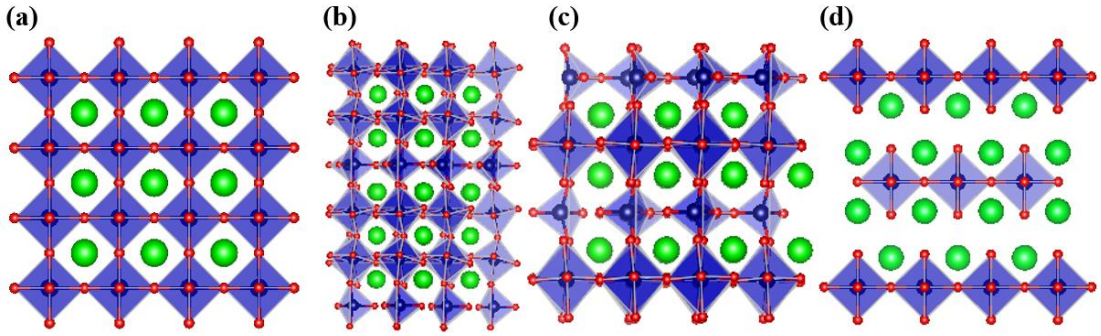

***Fig. 6.1**. Structural diagrams of (a) as-grown perovskite (AG-P, ABO_3), (b) Grenier (GN, $ABO_{2.7}$), (c) brownmillerite (BM, $ABO_{2.5}$) and (d) Ruddlesden-Popper (RP, $A_{n+1}B_nO_{3n+1}$ where n = 1) phases. The green, blue and red spheres represent the A, B and O ions, respectively.*

6.2 Experimental Methods

Epitaxial LCO thin films (thickness of 16~18 nm) were deposited on (001)-oriented $(LaAlO_3)_{0.3}(Sr_2TaAlO_6)_{0.7}$ (LSAT) substrates by pulsed laser deposition (PLD) with a laser pulse frequency of 1 Hz and laser fluence of ~ 0.8 J cm^{-2}. Epitaxial LSFO thin films (thickness of ~ 20nm) were deposited on (001)-oriented $SrTiO_3$ substrates by PLD with a laser pulse frequency of 10 Hz and laser fluence of ~ 0.7 J cm^{-2}. During the growth of both films, the substrate temperature was held at 700 ºC and the oxygen pressure was 300 mTorr. The films were cooled slowly to room temperature after the deposition with an oxygen pressure of 300 Torr to ensure proper oxygen stoichiometry. The LCO and LSFO films were then annealed in a gas evolution system which consists of a tube furnace connected to a high vacuum system capable of achieving oxygen partial pressures from 10^{-12} to 0.1 atm and temperatures up to

900 °C [126]. In the gas evolution system, the base pressure was maintained at ~10^{-10} atm, and high-purity oxygen (>99.99%) of different pressures ranging from 10^{-12} to 10^{-7} atm was introduced into the annealing chamber using the computer-controlled metal-seated valve [126]. All of the pressures quoted in the following sections are referring to the oxygen partial pressures, P_{O_2}.

The structural properties of the films were characterized by XRR and high-resolution XRD using a Bruker D8 Discover with Cu $K_{\alpha 1}$ x-rays. The XRR curves were fit using GenX software to determine the thickness, roughness, and density of the films [89,92]. A Lakeshore cryogenic probe station was used to measure the film resistivity upon warming from 80 K with the van der Pauw geometry. The bulk magnetic properties were measured using a Quantum Design VersaLab vibrating-sample magnetometer (VSM) with the magnetic field applied along the in-plane [100] substrate direction. Soft x-ray magnetic spectroscopy at the Co *L*-edge was performed at 80 K at beamline 6.3.1 at the Advanced Light Source (ALS) using luminescence yield (LY) detection, which probes the full film thickness [63]. The x-rays were incident upon the sample at a 30° grazing angle along the in-plane [100] substrate direction. X-ray magnetic circular dichroism (XMCD) spectra were calculated as the difference between XA spectra acquired with positive/negative 1.93 T magnetic fields oriented parallel to the propagation direction of the circularly polarized x-rays. X-ray magnetic linear dichroism (XMLD) spectra

at the Fe *L*-edge were calculated as the difference between XA spectra acquired using *s*- and *p*-polarized x-rays such that the x-ray ***E***-vector is respectively parallel to the in-plane [010] substrate direction or 30° away from the [001] substrate direction, due to the grazing-incidence geometry of the measurements. Both the XA spectra used to calculate Fe XMLD and the O *K*-edge XA spectra were performed at room temperature at beamline 4.0.2 at the ALS using total electron yield detection (TEY, which provides surface sensitive measurements to the top 5-10 nm of the sample).

6.3 Results and Discussion

6.3.1 $LaCoO_3$

Table 6.1*. The annealing conditions to initiate the phase transformations in LCO films.*

Sample	Annealing conditions
LCO-900	900ºC / 10^{-12} atm P_{O_2} / 1 hr
LCO-600	600ºC / 10^{-12} atm P_{O_2} / 1 hr
LCO-400	400ºC / 10^{-12} atm P_{O_2} / 1 hr

To initiate the phase transformations, the as-grown perovskite $LaCoO_3$ (AG-P LCO) samples were annealed in three different reducing conditions as listed in **Table 6.1**. The three samples after anneals are denoted as LCO-900, LCO-600, and LCO-400 based on their annealing temperatures.

Analysis of ω-2θ XRD curves (**Fig. 6.2** and **6.3**) enable the identification of the phases present after each reducing anneal. Annealing the LCO thin films at 400 ^{o}C/10^{-12} atm P_{O_2} resulted in the transformation to a mixed phase with both the GN ($LaCoO_{2.7}$, **Fig. 6.1(b)**) and BM ($LaCoO_{2.5}$, **Fig. 6.1(c)**) phases. These phases were identified by their prominent third-order and half-order peaks due to the integer-multiplied unit cell size of the GN and BM phases compared to the parent perovskite. The lattice parameters for the GN and the BM phases are 23.599 Å and 16.068 Å, respectively. The set of peaks for the BM phase have higher intensity than that for the GN phase, suggesting the majority of the film volume consisted of the BM phase. The fitting of the XRR curves (**Fig. 6.5**) indicate the film consisted of 20 nm of the $LaCoO_{2.6}$. The oxygen stoichiometry of 2.6 could be an average oxygen content between the BM and GN phases. The overall density decreased 5% upon transformation from the perovskite phase to the mixture of the BM and GN phases, which is comparable with the 13% decrease observed in the LSCO topotactic transformation where it formed pure BM phase. The smaller density decrease in LCO is expected due to the formation of the GN phase which has higher density than BM. As shown in **Fig. 6.4**, both of the BM and GN phases were metastable and slowly transformed back to the perovskite phase over a period of several weeks at room temperature in air.

Upon annealing at 600 ^{o}C/10^{-12} atm P_{O_2}, the film peaks disappear as shown in **Fig. 6.2** (orange

curves). XRR curves indicate a 10% decrease in density while the film thickness remained almost the same. This absence of XRD film peaks could be explained by amorphization of the LCO thin film or the formation of a nano-textured phase where the film breaks up into small crystalline regions in which the planes are not oriented parallel to the substrate surface [47,120]. As discussed in Chapter 4, $La_{0.7}Sr_{0.3}CoO_3$ (LSCO) thin films also demonstrated that after annealing, the sample could consist primarily of polycrystalline grains of the Ruddlesden-Popper (RP) phase (**Fig. 6.1(d)**) separated by amorphous regions/regions of low crystallinity, or crystalline planes not perfectly aligned with the underlying substrate due to the presence of defects and dislocations at the film-substrate interface [187].

After the LCO thin films were annealed at 900 ^{o}C/10^{-12} atm P_{O_2}, broad and weak XRD film peaks emerged which are consistent with a mixture of an RP phase and an unidentified phase (denoted in purple diamonds in **Fig. 6.3(b)).** The lack of thickness fringes in the zoom-in XRD curves (**Fig. 6.2(b)**) indicates that compared to the AG-P LCO sample, the crystalline lattice of the LCO-900 sample has high interface roughness, various defects and *d*-spacing variations due to strain gradients. The RP phase can be indexed to an out-of-plane lattice parameter of 12.78 ± 0.31 Å, and has broader film peaks compared to the unidentified phase. The unassigned peaks phase do not correspond to the diffraction patterns of metallic Co or common Co-containing oxides such as CoO, CoO_2, Co_2O_3 or Co_3O_4 [132,208-211], however, they are

structurally from the same family of planes as their *d*-spacing corresponds to 1.81 and 3.60 Å. The RP phase was formed after the parent perovskite phase lost both oxygen anions and cobalt cations upon annealing under highly reducing conditions [187]. XRR (**Fig. 6.5** pink curves) show that the LCO-900 sample experiences a quadrupled increase in roughness (0.46 nm to 2.02 nm), a 7% increase in the total film thickness (18.0 nm to 19.3 nm), and a dramatic 22% decrease in density (7.25 g cm^{-3} to 5.66 g cm^{-3}), suggesting a substantial structural modification upon annealing. These changes in film thickness and density are comparable with the LSCO topotactic transformation where a single-crystalline RP phase was formed (5% decrease in film thickness and 23% decrease in density).

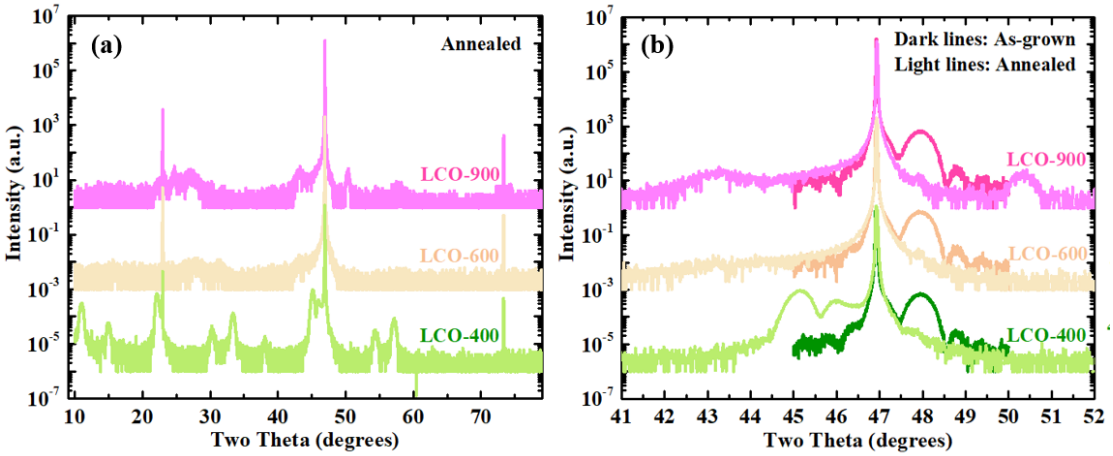

***Fig. 6.2**. (a) Full-range and (b) zoom-in XRD curves of the LCO films after the reducing anneals. Annealing conditions are listed in **Table 6.1**. The dark and light lines refer to the initial and annealed samples, respectively.*

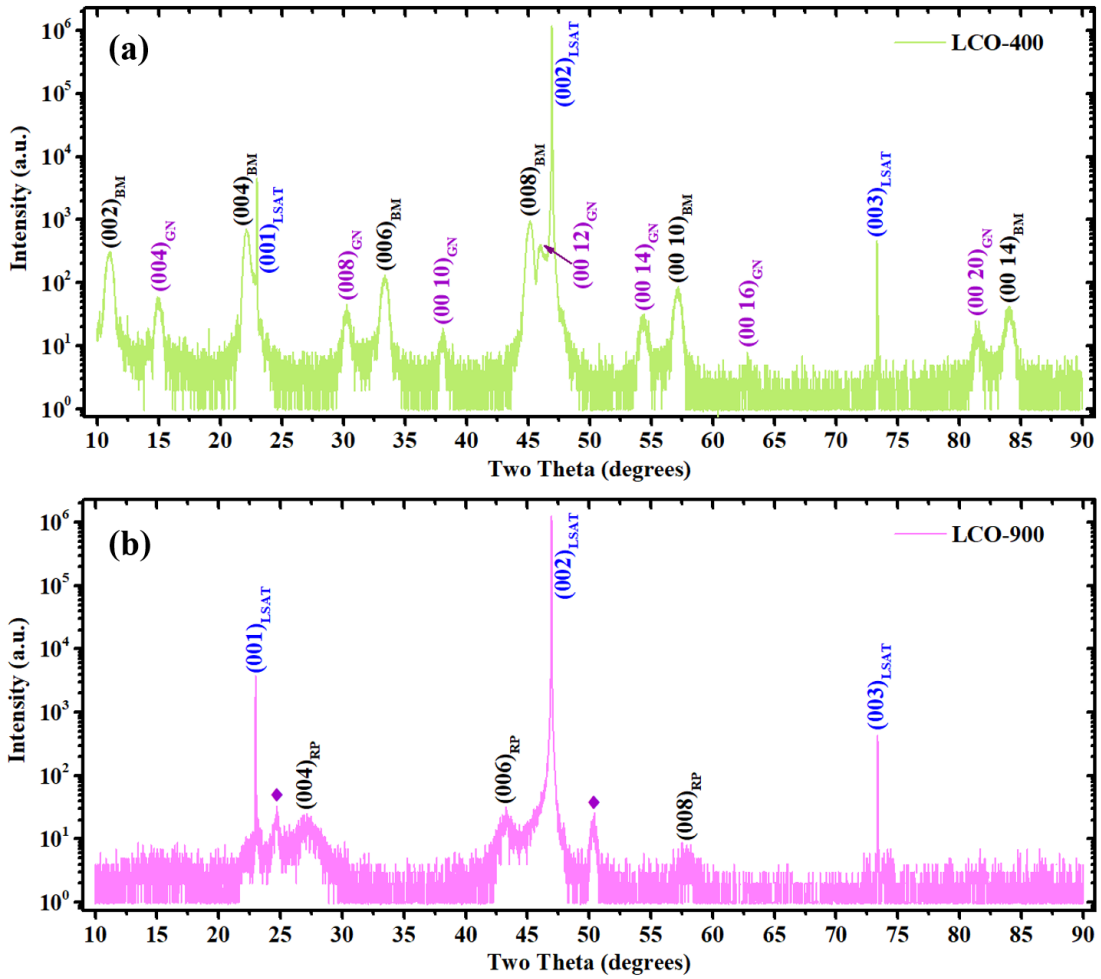

***Fig. 6.3**. Full-range XRD pattern of (a) LCO-400 and (b) LCO-900 samples. The purple diamonds in (b) represents an unidentified phase.*

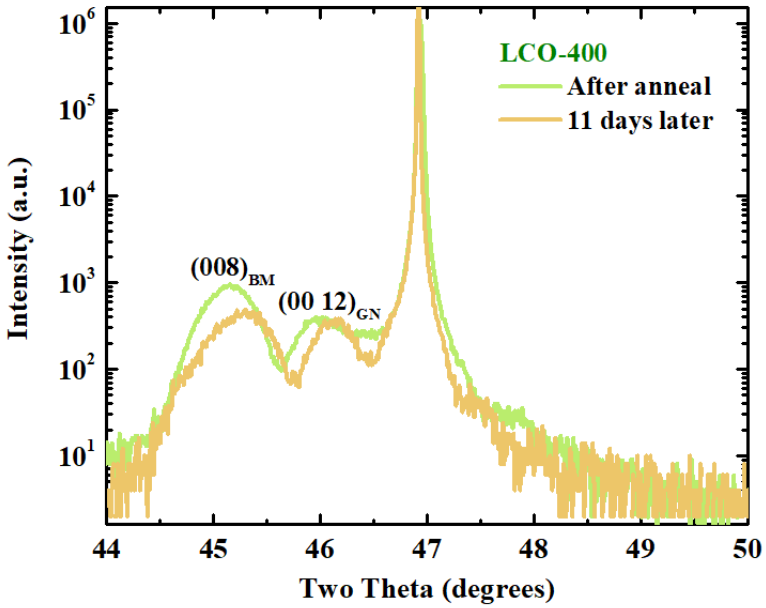

Fig. 6.4. *When held in air at room temperature, both of the BM and GN phases slowly transformed back to the perovskite phase. The green curve was measured immediately after the anneal, while the yellow curve was measured 11 days after the anneal. Both of the peaks shifted to higher two-theta values, indicating the lattice parameters of both the BM and GN phases have decreased towards that of the perovskite phase.*

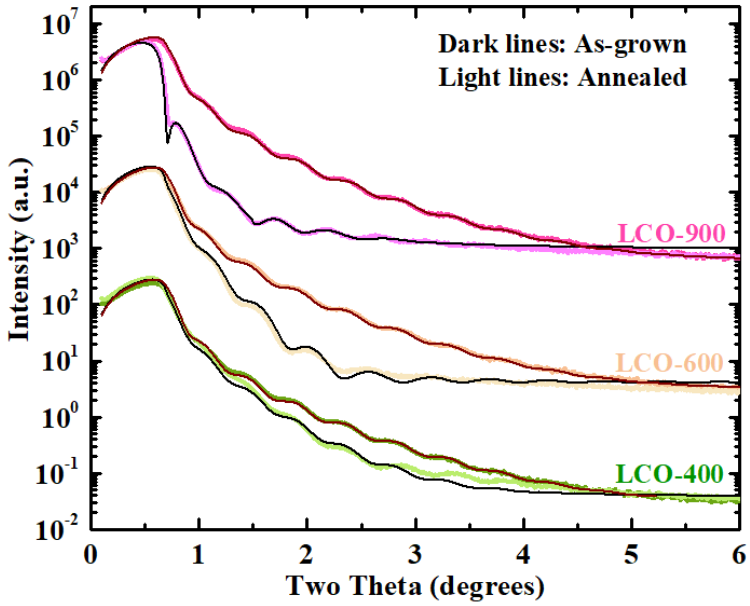

***Fig. 6.5**. XRR curves of the LCO films exposed to anneals under highly reducing conditions. The dark and light lines refer to the initial and annealed samples, respectively. The black thin curves on top of the colored lines are the fitting curves.*

***Table 6.2**. XRR fitting parameters for the samples before annealing*

Sample	Fitting model	Thickness (nm)	Roughness (nm)	Density (g cm^{-3})
$LCO\text{-}900_{initial}$	$LaCoO_3$	18.0 ± 0.03	0.46 ± 0.03	7.25 ± 0.02
$LCO\text{-}600_{initial}$	$LaCoO_3$	17.7 ± 0.01	0.52 ± 0.05	7.25 ± 0.01
$LCO\text{-}400_{initial}$	$LaCoO_3$	18.1 ± 0.03	0.23 ± 0.01	7.25 ± 0.01

***Table 6.3**. XRR fitting parameters for the samples after annealing*

Sample	Fitting model	Thickness (nm)	Roughness (nm)	Density (g cm^{-3})
LCO-900	$La_2Co_{1-\upsilon}O_{4-\delta}$	19.3 ± 0.02	2.02 ± 0.04	5.66 ± 0.03
LCO-600	$La_2Co_{1-\upsilon}O_{4-\delta}$	17.5 ± 0.03	1.39 ± 0.04	6.53 ± 0.02
LCO-400	$LaCoO_{2.6-\delta}$	20.0 ± 0.04	1.02 ± 0.02	6.85 ± 0.04

XA spectra (**Figs. 6.6(a) and 6.7(a)**) were acquired in order to detect the change in Co valence state and local coordination associated with the phase transformations. The AG-P sample agrees with literature data for Co^{3+} valence state in octahedral coordination [212]. The XA spectra of the reduced phases (samples LCO-400, LCO-600 and LCO-900) show drastic differences compared to that of the AG-P phase. To quantitatively estimate their valence states, these XA spectra were fit to reference spectra, *i.e.*, metallic Co (**Fig. 6.7(a)** brown), Co^{3+} ions ($LaCoO_3$ in the experimental AG-P phase, **Fig. 6.7(a)** gray) and Co^{2+} ions ($CoFe_2O_4$ [147], **Fig. 6.7(a)** violet) in octahedral coordination. According to the fitting results shown in **Fig. 6.7(a)**, samples LCO-400 (green curves) and LCO-900 (pink curves) consisted of approximately 22~25% of AG-P phase and 75%~78% of Co^{2+} ions in octahedral coordination. The decrease in the Co valence state from Co^{3+} in AG-P phase to Co^{2+}/Co^{3+} mixture in samples LCO-400 and LCO-900 is expected in order to maintain charge neutrality upon increase in oxygen deficiency (δ) after annealing. On the other hand, sample LCO-600 possesses a unique XA spectral shape compared to all the other samples. Fitting of the XA spectra (**Fig. 6.7(a)** orange) shows that this sample can be considered as a mixture consisting of 46% of Co^{2+} ions in octahedral coordination and 54% metallic Co.

XMCD measurements at the Co $L_{3,2}$ absorption edges (**Fig. 6.6(b)**) provide complementary

information on the element/coordination specific contributions to the FM properties of the annealed LCO thin films. No FM signal was detected for the AG-P sample at 80 K, which agrees with literature data that the LCO is an insulating antiferromagnet [198]. Samples LCO-400 and LCO-900 also show no FM response in their XMCD spectra, while sample LCO-600 shows a stark negative peak without the multiplet structure typically found in complex oxides and is more reminiscent of metallic Co atoms. Fitting of the XMCD spectra (**Fig. 6.7(b)**) for this sample shows that it can be considered as a mixture consisting of approximately 41% of Co^{2+} ions in octahedral coordination and 59% metallic Co, consistent with the XA spectra fitting results (*i.e.*, 46% of Co^{2+} ions and 54% metallic Co). As shown in **Fig. 6.8**, the hysteresis loops and bulk magnetization measurement show that this phase has a low coercivity (*i.e.*, H_C ~ 0.1 T) and a high T_C value, consistent with the presence of FM Co nanoparticles [153,154]. The measured M_S of these Co nanoparticles (M_S = 1358 emu cm^{-3}) corresponds well to the reported values for metallic Co (M_S ~ 1400 emu cm^{-3} [158,159]) and the Co nanoparticles exsolved from the *LSCO* sample annealed under the same reducing condition (M_S = 1352 emu cm^{-3} [187]). The small size, low density, and/or random orientation of the Co nanoparticles preclude their observation in XRD measurements. Based on the work reported in Chapter 4, annealing LSCO thin films also leads to the exsolvation of metallic Co nanoparticles [187]. Similar effects have also been observed in the electrodes of solid oxide fuel cells where nickel particles exsolved from nickel oxides [141,142].

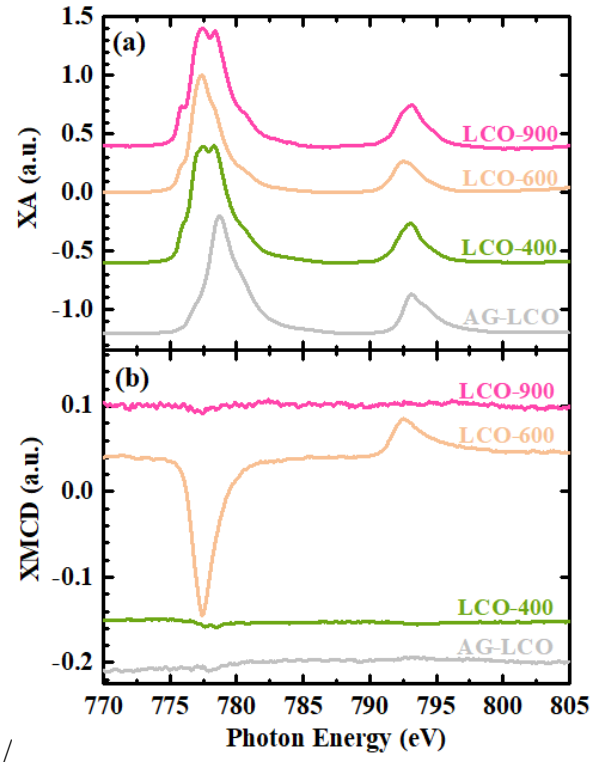

Fig. 6.6*. (a) Co $L_{3,2}$ XA and (b) XMCD spectra acquired at 80 K for LCO thin films after reducing anneals.*

Compared to LSCO, the GN phase is more stable and the RP phase less stable in LCO. There are also a lot more exsolved Co metallic nanoparticles in LCO than LSCO (~56.5% Co in LCO *vs.* 23% Co in LSCO). To explain the difference between them, we need to first acknowledge the BM structure in LCO ($LaCoO_{2.5}$) is highly unstable, indicating the pure Co^{2+} ions are the unfavorable valence state for LCO. Based on this theory, the GN phase is more stable in LCO since it has the average valence state of $Co^{2.4+}$, suggesting it is not pure Co^{2+} ions but a mixture of Co^{2+} and Co^{3+} ions. The RP phase LCO is less stable due to its chemical formula of La_2CoO_4,

which again contains the undesirable Co^{2+} ions. The larger amount of exsolved Co metallic nanoparticles in LCO is also expected in order to reduce the amount of Co^{2+} ions in the LCO lattice.

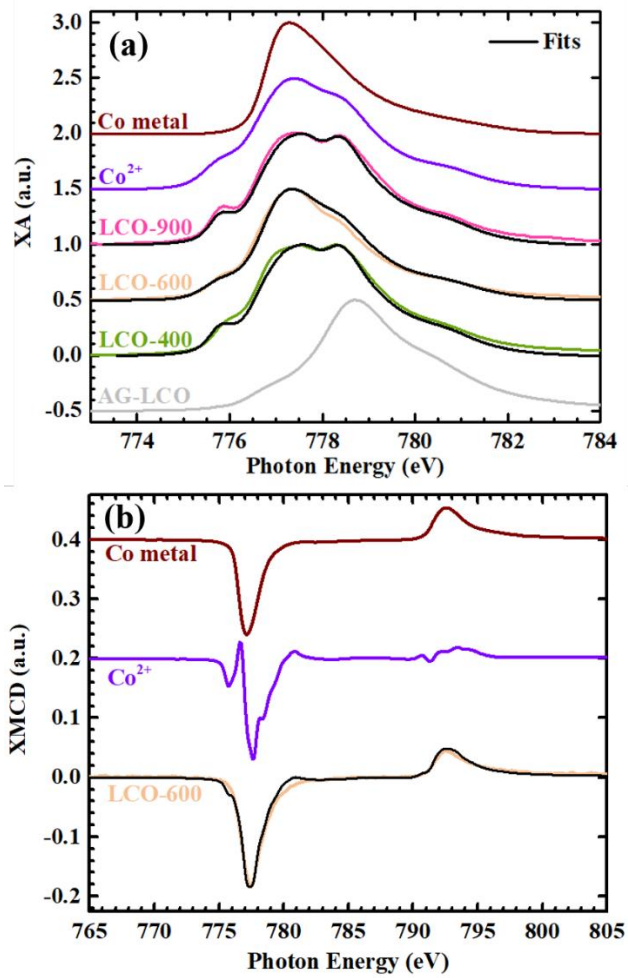

Fig. 6.7*. Experimental curves (colored) and fitting results (black) of Co $L_{3,2}$ (a) XA and (b) XMCD spectra acquired at 80 K for the reduced samples. Reference spectra used for the fitting include metallic Co (brown), Co^{3+} ions ($LaCoO_3$ in the experimental AG-P phase, gray) and Co^{2+} ions ($CoFe_2O_4$ [147], violet) in octahedral coordination.*

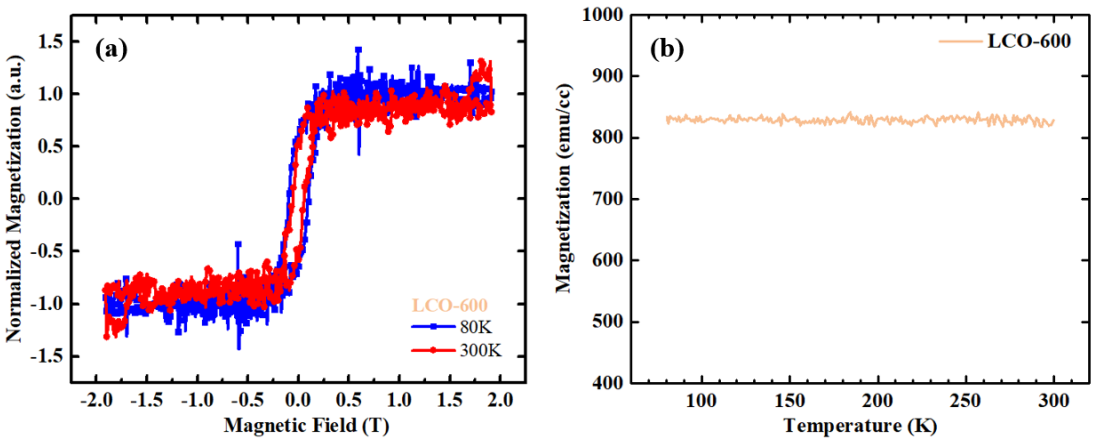

***Fig. 6.8**. (a) Co L_3 XMCD hysteresis loops at 80 K (blue) and 300 K (red) and (b) Film-averaged magnetization as a function of temperature for the LCO-600 sample. The bulk magnetization data was normalized to the estimated volume of all the Co nanoparticles (i.e., ~ 57% of the total LCO-600 film volume, based on XA spectra fitting results). A magnetic field of 0.08 T was applied along the [100] substrate direction during the magnetization measurements.*

6.3.2 $La_{0.7}Sr_{0.3}FeO_3$

The reducing anneals under highly reducing conditions were also carried out on Sr-doped lanthanum ferrite ($La_{0.7}Sr_{0.3}FeO_{3-\delta}$, LSFO) thin films. At this Sr-doping level, the perovskite phase is the equilibrium phase with T_N ~ 360 K [213,214]. The as-grown perovskite (AG-P) LSFO samples were annealed in four different reducing conditions, as summarized in **Table 6.4**. The samples after anneals are denoted based on their annealing conditions.

The LSFO thin films gradually underwent phase transformations as revealed through XRR (**Fig. 6.9(a)**) and XRD measurements (**Fig. 6.9(b)**). **Table 6.5** and **6.6** list the parameters obtained from fitting the XRR curves using GenX software [89]. The XRR curves reveal changes in the film thickness, density, and roughness associated with the phase transformations. For increasingly reducing annealing conditions, a trend of decreasing density and increasing film thickness and roughness can be observed, as expected for perovskite-related materials with increasing oxygen deficiency [134,135] associated with the reducing anneals. At the most reducing annealing condition (900 °C/10^{-12} atm P_{O_2}), the LSFO thin film experiences a slight increase in the total film thickness (21.1 nm to 21.5 nm, 1.9% increase) and roughness, accompanied with a small decrease in the main layer density (6.31 g cm^{-3} to 6.12 g cm^{-3}, 3.0% decrease).

Table 6.4*. The annealing conditions applied to the LSFO films.*

Sample	Annealing conditions
LSFO-900-12	900°C / 10^{-12} atm P_{O_2} / 1 hr
LSFO-600-12	600°C / 10^{-12} atm P_{O_2} / 1 hr
LSFO-400-12	400°C / 10^{-12} atm P_{O_2} / 1 hr
LSFO-400-7	400°C / 10^{-7} atm P_{O_2} / 1 hr

Analysis of ω-2θ XRD curves (**Fig. 6.9(b)**) enable the identification of the phases present after each reducing anneal. **Fig. 6.9(b)** black curve shows the expected *(002)* peak for the perovskite phase with an out-of-plane lattice parameter of 3.892 Å. Upon annealing up to 900 °C/10^{-12}

atm P_{O_2}, the same *(002)* peaks can be observed (**Fig. 6.9(b)** color curves), indicating that the perovskite phase is maintained. However, the film peaks are shifted to the low angle side of the STO substrate peak compared to the AG-P phase, suggesting the lattice parameters of the annealed phases have expanded as listed in **Table 6.7**. The increase of the lattice parameter did not suggest the structural transformation from perovskite to BM occurred, as no half-order peaks were observed in the XRD curves for any of the annealed samples. Compared to the AG-P phase, the reduced phases have larger interfacial roughness and *d*-spacing variations, as confirmed by XRR in **Fig. 6.9(a)**, **Fig. 6.10**, and **Table 6.6**. These oxygen-deficient phases are stable under ambient conditions for a timeframe of months, as determined through XRD measurements.

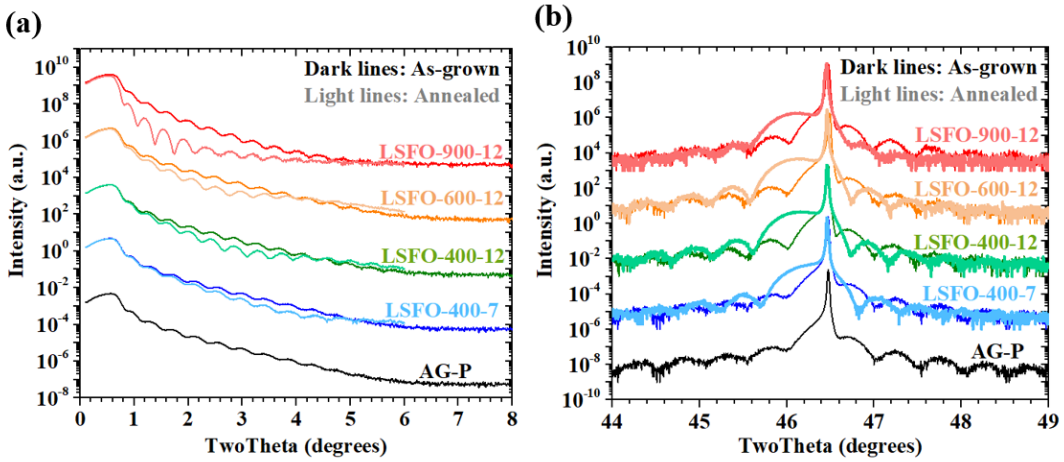

***Fig. 6.9**. (a) XRR and (b) XRD curves of the LSFO films exposed to anneals under highly reducing conditions. The dark and light lines refer to the initial and annealed samples, respectively.*

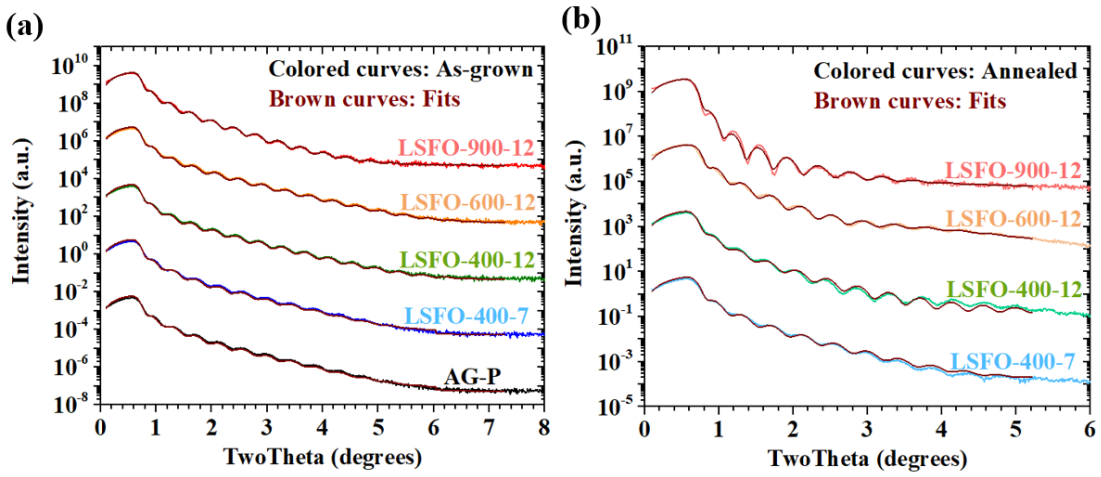

***Fig. 6.10**. XRR curves of the (a) as grown and (b) annealed LSFO films. The colored lines refer to the (a) as-grown and (b) annealed samples, while the brown thin curves on top of the colored lines are the fitting results.*

***Table 6.5.** XRR fitting parameters for the LSFO samples before annealing*

Sample	Fitting model	Thickness (nm)	Roughness (nm)	Density (g cm^{-3})
LSFO-900-$12_{initial}$	$La_{0.7}Sr_{0.3}FeO_3$	21.1 ± 0.04	0.55 ± 0.04	6.31 ± 0.01
LSFO-600-$12_{initial}$	$La_{0.7}Sr_{0.3}FeO_3$	20.0 ± 0.03	0.41 ± 0.03	6.30 ± 0.01
LSFO-400-$12_{initial}$	$La_{0.7}Sr_{0.3}FeO_3$	20.5 ± 0.02	0.43 ± 0.02	6.32 ± 0.02
LSFO-400-$7_{initial}$	$La_{0.7}Sr_{0.3}FeO_3$	19.6 ± 0.03	0.30 ± 0.03	6.31 ± 0.01
AG-P	$La_{0.7}Sr_{0.3}FeO_3$	19.2 ± 0.01	0.51 ± 0.02	6.31 ± 0.00

Table 6.6. *XRR fitting parameters for the LSFO samples after annealing*

Sample	Fitting model	Thickness (nm)	Roughness (nm)	Density (g cm^{-3})
LSFO-900-12	$La_{0.7}Sr_{0.3}FeO_{3-\delta}$	21.5 ± 0.04	1.10 ± 0.05	6.12 ± 0.04
LSFO-600-12	$La_{0.7}Sr_{0.3}FeO_{3-\delta}$	20.2 ± 0.02	0.56 ± 0.04	6.17 ± 0.01
LSFO-400-12	$La_{0.7}Sr_{0.3}FeO_{3-\delta}$	20.7 ± 0.03	0.51 ± 0.04	6.21 ± 0.02
LSFO-400-7	$La_{0.7}Sr_{0.3}FeO_{3-\delta}$	19.7 ± 0.01	0.49 ± 0.03	6.25 ± 0.03

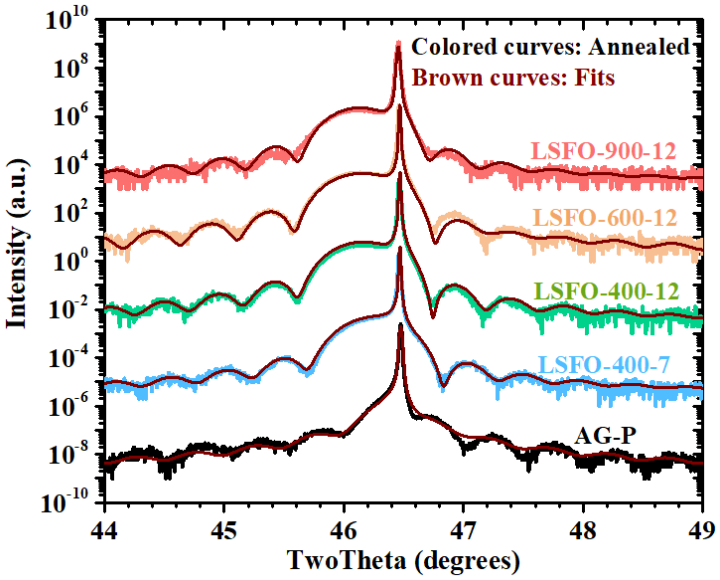

Fig. 6.11*. XRD curves of the as-grown (black) and annealed (colored) LSFO films. The brown thin curves on top of the black/colored XRD curves are the fitting results. These oxygen-deficient phases are stable under ambient conditions for a timeframe of months.*

Table 6.7*. The film thickness and out-of-plane lattice parameters of the annealed LSFO films, extracted from the XRD fitting results. The thickness is consistent with the XRR fitting results, nominally within ± 1 nm for every sample.*

Sample name	Film thickness (nm)	Lattice parameter (nm)
LSFO-900-12	21.7 ± 0.02	0.3939 ± 0.0002
LSFO-600-12	19.9 ± 0.03	0.3938 ± 0.0003
LSFO-400-12	21.0 ± 0.04	0.3938 ± 0.0002
LSFO-400-7	20.5 ± 0.03	0.3931 ± 0.0003
AG-P	19.5 ± 0.01	0.3908 ± 0.0001

The bulk electrical properties of the annealed LSFO thin films are shown in **Fig. 6.12**. The resistivity data was normalized to the thin film volume. The AG-P sample has the highest resistivity among all of the samples due to the antiferromagnetic/insulating nature of the perovskite LSFO. The high resistivity at room temperature prevents low temperature measurements. The room temperature resistivity of all of the annealed samples is lower than that of the AG-P phase. While the resistivity of samples LSFO-400-7 and LSFO-400-12 increases as the temperature decreases (consistent with the insulating behavior observed in LSFO), the resistivity of LSFO-600-12 remains constant within the temperature range of 210 and 330 K and has an insulating behavior between 130 and 210 K. Below 130 K, the resistivity is too high to be measured. In contrast, LSFO-900-12 behaves the most differently as its resistivity is 3~7 orders of magnitude lower than the other reduced phases. The resistivity increases as temperature increases in the entire range studied, consistent with the metallic

behavior. Despite the annealed samples were structurally similar (*i.e.*, the lattice parameters, thicknesses, and densities were close to one another), the resistivity spanned across 7 orders of magnitude and the metal-insulator transition have changed, potentially indicating the electrical transformations associated with the anneals.

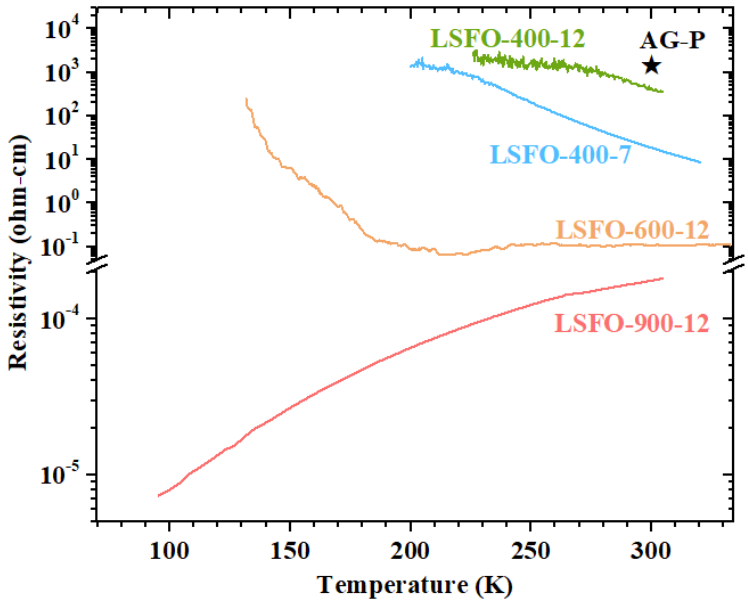

***Fig. 6.12**. Film-averaged resistivity as a function of temperature for LSFO thin films after reducing anneals.*

XA spectra (**Fig. 6.13(a)**) were acquired in order to detect the change in Fe valence state and local coordination associated with the phase transformations. The AG-P sample agrees with literature data for mixed valence Fe^{3+}/Fe^{4+} ions in octahedral coordination [92,202,213]. While the XA spectra are similar between the AG-P and annealed samples, an intensity change in the

L_2 features (denoted as features A/B in **Fig. 6.13(a)**) can be observed. As shown in **Table 6.8**, the intensity ratio of features A and B increases as the LSFO films were annealed under increasingly reducing conditions, indicating the increased proportion of Fe^{3+} ions in the Fe^{3+}/Fe^{4+} mixed valence states [215]. The decrease in the Fe valence state in the reduced phases is expected in order to maintain charge neutrality upon increase in oxygen deficiency (δ) in the films.

XMLD spectroscopy (**Fig. 6.13(b)**) was used to probe the asymmetry between the in-plane <100> and out-of-plane [001] directions in the annealed LSFO thin films, where this asymmetry may arise from factors such as the charge distribution around the Fe ions due to antiferromagnetic (AFM) order, orbital ordering (d_{x2-y2} *vs.* d_{z2} orbitals), and structural asymmetry [67,68]. While the structural and orbital ordering effects should largely be temperature independent, the identification of the AFM contribution can be made by acquiring XMLD spectra below T_N. At room temperature, the sign of the Fe XMLD spectra (**Fig. 6.13(b)**) is reversed for the AG-P sample compared to all the annealed samples. The analysis of XMLD spectra as described in the literature [213,216] indicates an out-of-plane canting of the AFM spin axis in the AG-P LSFO film and conversely an in-plane alignment of the AFM spin axis in the annealed samples. Compared to single-layer LSFO thin films, it has been shown that the AFM spin axis could reorient in the LSFO ultrathin films in $La_{0.7}Sr_{0.3}MnO_3$/LSFO superlattices

[92,202,213]. The azimuthal angular dependence of the XMLD spectra could help identify their exact magnetic phases and AFM spin orientations.

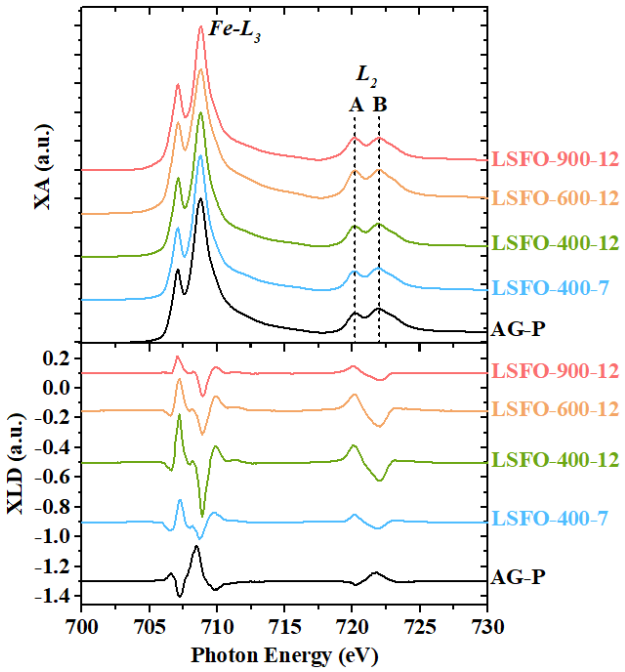

Fig. 6.13. *Fe $L_{3,2}$ (a) XA and (b) XMLD spectra for LSFO thin films after reducing anneals. The dashed lines (A and B) denote the multiplet features at the Fe-L_2 edge.*

Table 6.8. *The intensity of features A and B (denoted in the XA spectra in* ***Fig. 6.13****) and their ratio.*

Sample name	*A* intensity	*B* intensity	*A/B* ratio
LSFO-900-12	0.2224	0.2226	0.9991
LSFO-600-12	0.2970	0.3005	0.9884
LSFO-400-12	0.2101	0.2246	0.9354
LSFO-400-7	0.1970	0.2190	0.8995
AG-P	0.2060	0.2370	0.8692

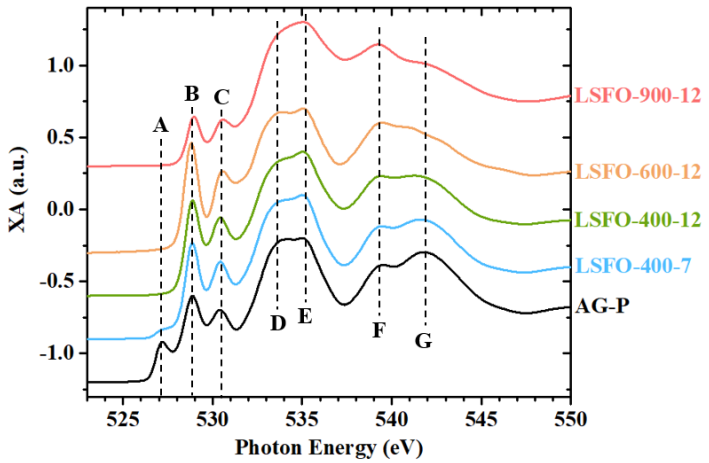

***Fig. 6.14**. Oxygen K-edge XA spectra acquired at 300 K for LSFO thin films after reducing anneals. The dashed lines A-G denote the XA spectral features.*

To further confirm the decrease in Fe valence state associated with the reducing anneals, XA spectra at the oxygen *K*-edge were acquired. As shown in **Fig. 6.14**, seven spectral features (denoted as A-G) can be identified. Going from samples AG-P to LSFO-900-12, the decreased intensity in features A, D, and G indicates the increased proportion of Fe^{3+} ions [215], consistent with the observation in Fe XA spectra. Spectral features B and C denote Fe *3d* characters, while features F and G are attributed to high energy metal states such as Fe *4sp* or La *6sp* orbitals. These assignments are consistent with previous XA and electron energy-loss spectroscopy (EELS) studies of transition-metal compounds [217-222] with preliminary band-structure calculations for $LaTiO_3$ [223].

6.4 Conclusion

In summary, phase transformations involving the loss of oxygen anions were observed in LCO and LSFO thin films upon annealing under highly reducing conditions. In both systems, the valence state of the Co/Fe ions was reduced to maintain charge neutrality upon increase in oxygen deficiency (δ) in the films. In terms of the structural properties, the LCO reduced phases include GN, BM, and also the RP phases. A composite phase consisting of FM Co nanoparticles embedded in an insulating matrix was observed when the LCO film was annealed at 600 °C/10^{-12} atm P_{O_2}, thus the film experienced a magnetic property change from AFM to FM. The room temperature resistivity also spanned multiple orders of magnitude in LCO films upon annealing. In contrast, the LSFO films remained in the oxygen-deficient perovskite phase and did not transform to other structural phases even when annealed at the most reducing condition explored in this work. However, the oxygen deficiency in LSFO films did increase upon annealing in the increasingly reducing environment, as confirmed in the *Fe* and *O* XA spectra. It was also shown that both the AFM spin axes of the LSFO films and the magnitude of the XMLD signals changed with the annealing conditions. Despite annealed in the same reducing conditions, the difference in ionic conductivity between Co and Fe ions could contribute to the different topotactic transformations in these two systems. The fact that each structure possessed its own distinct set of physical properties and the ability to control these properties by movement of ion migration suggest their potential for further exploration into the reversibility and for discovery of attractive candidates for future spintronic applications.

Chapter 7: Conclusions and Future Works

This dissertation advances our understanding of the functional capabilities of magnetic perovskite oxide thin films, with a particular focus towards the growth and characterization of perovskite and perovskite-related phases. Perovskite oxides such as cobaltites $La_{1-x}Sr_xCoO_{3-\delta}$ and manganites $Nd_{1-x}Sr_xMnO_{3-\delta}$ (NSMO) are promising materials to realize low-power neuromorphic devices, since they display a unique metal-to-insulator transition (MIT) under the action of physical stimuli and they offer the opportunity of designing desirable resistive switching states. Studies such as those included here can provide insight towards the sensitive relationship between the structure and functional properties of complex oxides as well as expand our knowledge on controlling fundamental magnetic and electrical parameters, which is a critical step toward future development of oxide-based magnetic/electronic applications and neuromorphic devices.

Synchrotron soft x-ray spectroscopy experiments have been invaluable in unveiling the chemical, magnetic, and electronic properties of the perovskite and perovskite-related phases. The work of Chapter 3 applied x-ray absorption (XA)/x-ray magnetic circular dichroism (XMCD)/x-ray linear dichroism (XLD) spectroscopy to NSMO thin films grown on (110)-oriented STO substrates and studied the electronic and magnetic transitions. A pure antiferromagnetic (AFM) signature of the NSMO film was extracted below T_N, however, a

proportion of the ferromagnetic (FM) phase remained for temperatures down to 80 K. The lateral coexistence of the FM and AFM phases was directly imaged by x-ray photoemission electron microscopy (X-PEEM), where they form extended domains along the [001] substrate direction. This understanding of the electronic/magnetic transitions of NSMO in thin film form is necessary to enable its incorporation into next generation memory devices.

The topotactic transformations introduced in Chapter 4 show the ability to control the physical properties of $La_{0.7}Sr_{0.3}CoO_{3-\delta}$ (LSCO) thin films by movement of ion migration. Upon annealing the films under highly reducing conditions, the loss of both oxygen anions and cobalt cations in the films leads to phase transformations involving not only the oxygen-deficient perovskite and brownmillerite (BM) phases, but the Ruddlesden-Popper (RP) phase which has been rarely reported in the cobaltite topotactic transformations. A composite phase consisting of FM Co nanoparticles embedded in an insulating RP matrix was observed at an intermediate annealing condition investigated in this work. Density functional theory (DFT) calculations further confirmed that the formation of the RP phase and Co nanoparticles is thermodynamically possible, and the calculated structural, magnetic and electronic properties supported the experimental measurements. Each structure possessed its own distinct set of physical properties and suggest their potential for future applications such as neuromorphic devices tuned by electric fields.

Chapter 5 combined experiments and theory to identify fingerprints of oxygen vacancies in LSCO thin films. To quantify the absolute δ values in $La_{0.7}Sr_{0.3}CoO_{3-\delta}$ thin films obtained after exposure to reducing anneals, oxygen *K*-edge x-ray absorption (XA) spectra were acquired and it is shown that the change in the peak separation is a reliable feature to determine the δ values in the LSCO films. With increasing δ, the out-of-plane lattice parameter increases, causing the magnetization and the resistivity of the films to decrease and increase, respectively. The resistivity of LSCO thin films can be finely tuned as a function of oxygen vacancies (from 10^{-3} to 10^{5} ohm-cm), facilitating the design of neuromorphic devices which requires precise control of material properties.

Finally, Chapter 6 continued on the topotactic transformations induced by exposure to highly reducing anneals, but now in $LaCoO_{3-\delta}$ (LCO) and $La_{0.7}Sr_{0.3}FeO_{3-\delta}$ (LSFO) thin films instead of LSCO discussed in Chapters 4 and 5. In both LCO and LSFO films after the reducing anneals, the valence state of the Co/Fe ions was decreased to maintain charge neutrality upon increase in oxygen deficiency (δ). The LCO films transformed into Grenier, BM, and RP phases, and a composite phase consisting of FM Co nanoparticles embedded in an insulating matrix; while the LSFO films only reached the oxygen-deficient perovskite phase regardless of the annealing conditions used. Despite annealed in the same reducing conditions, the difference in ionic

conductivity between Co and Fe ions could contribute to the different topotactic transformations in these two systems. The fact that each structure possessed its own distinct set of physical properties and the ability to control these properties by movement of ion migration suggest their potential for further exploration into the reversibility and for discovery of attractive candidates for future spintronic applications.

7.1 Future Work

7.1.1 Reversibility in Topotactic Transformations

The recurring theme of this dissertation is topotactic transformations in magnetic perovskite oxides induced by high temperature/low oxygen pressure anneals. In order to be considered for practical device applications, the reversibility of these topotactic transformations has to be studied. As shown in **Fig. 7.1**, the BM phase of LSCO ($La_{0.7}Sr_{0.3}CoO_{2.5}$) was found to be metastable and slowly transformed back to the perovskite phase over a period of several months at room temperature in air, even when capped with 5 nm Gd/5 nm Au to try to prevent oxygen reincorporation into the film. This inferred the reversible chemical reactions between the perovskite and BM phases in LSCO. Future work should focus on the reversibility between the RP/nanoparticle (NP) and perovskite phases and the investigation of the optimized annealing conditions for film re-oxidation and for the Co nanoparticles to re-dissolve back to the crystal. The precise control of LSCO structural reversibility is critical for the design of emerging

applications due to the strong correlation of the magnetic and electronic properties to the crystal structures.

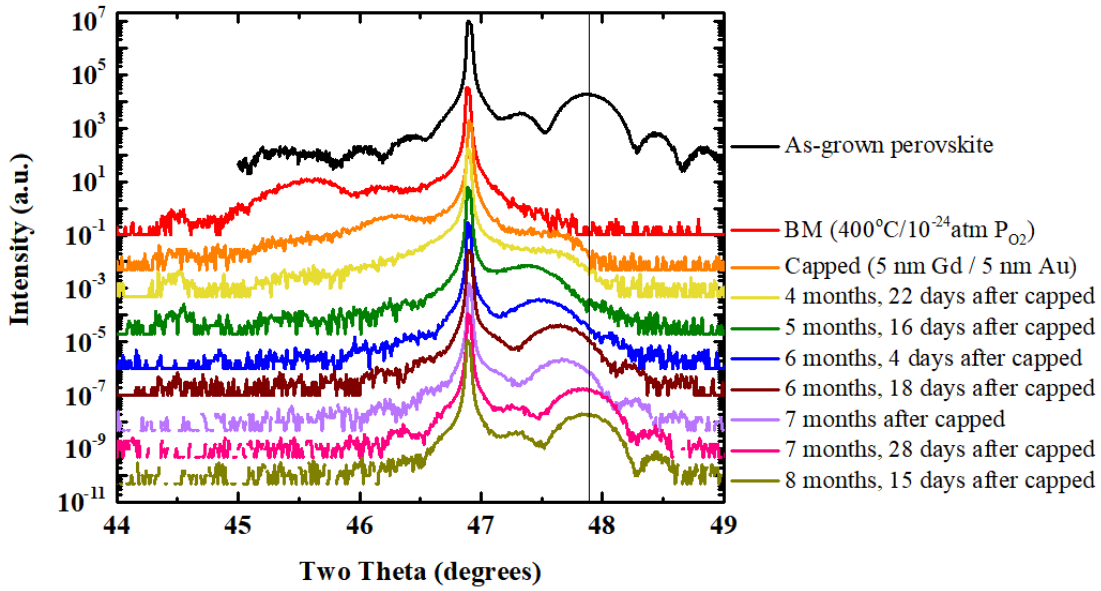

***Fig. 7.1**. The BM phase of LSCO ($La_{0.7}Sr_{0.3}CoO_{2.5}$) was found to be metastable and slowly transformed back to the perovskite phase over a period of several months at room temperature in air, even when capped with 5 nm Gd/5 nm Au to try to prevent oxygen reincorporation into the film.*

7.1.2 Voltage-Controlled Topotactic Transformations

Apart from annealing the magnetic perovskite oxides in reducing environment, the investigation of other stimuli to drive the topotactic transformations is another direction of the future work. It was reported in $SrFeO_{3-\delta}$ and $SrCoO_{3-\delta}$ systems where a reversible

transformation between the stable BM $SrFeO_{2.5}$ ($SrCoO_{2.5}$) phase and the metastable $SrFeO_3$ ($SrCoO_3$) perovskite phase was observed with an applied electrical field [42-47]. With further *reduction*, BM $SrFeO_{2.5}$ films could transform to the infinite-layer $SrFeO_2$ square planar phase [46,119]. Similar studies should be carried out on the LSCO thin films, to investigate whether an applied electric field can trigger the topotactic transformations and further provide strategies to minimize the required electrical bias to drive such a transition [224,225]. Since these topotactic transformations involve the movement of oxygen anions, it is expected that the applied voltages (where the driving force is the applied electric field) should direct the movement of these charged particles.

7.1.3 Topotactic Transformations in Bilayer Perovskite Oxides

The topotactic transformations in single layer LSCO, LCO and LSFO were discussed in Chapters 4 and 6. It is shown that at the same annealing conditions, each material can result in different structural phases, and each phase possesses its own distinct magnetic and electrical properties. One of the future directions for this work could be growing bilayer thin films and investigating their coupling behavior at the interfaces. For instance, a bilayer stack of LSFO and LSCO could be an interesting combination, since LSFO is AFM below the Neél temperature and LSCO is FM below the Curie temperature. According to the results from the single-layer films, the LSFO would stay in an oxygen-deficient phase and remain AFM but

become metallic after the reducing anneal at 900°C/10^{-12} atm P_{O_2}, while LSCO would transform to a RP phase and become FM and insulating. The AFM/metallic and FM/insulating properties can couple with each other at the interface, leading to a novel and unprecedented magnetic and electrical behavior. On the other hand, if the surface reaction is the rate-determining step in the annealing process, the topotactic transformations in LSFO could occur more readily in the LSCO/LSFO bilayer system when the LSCO is deposited as the surface layer.

7.1.4 Topotactic Transformations in Other Magnetic Perovskite Oxides

This dissertation covers the topotactic transformations in cobaltites and ferrites, but other magnetic perovskite oxides can also be explored. Several literature reports have focused on the gradual progression between the perovskite and BM phases demonstrated in $La_{0.67}Sr_{0.33}MnO_3$ (LSMO) [117] and $YBa_2Cu_3O_{7-\delta}$ (YBCO) [118], by the deposition of ultrathin Gd layers of varying thickness. The Gd getter layer experienced a spontaneous redox reaction to form GdO_x, leaching oxygen ions from the underlying complex oxide thin films and resulting in a topotactic transformation, which then leads to a change in the magnetic and electrical properties in these complex oxides. Alternatively, the annealing method discussed in this dissertation could also be conducted on LSMO and YBCO, or on other magnetic perovskite systems such as 50% Sr doping of LSCO ($La_{0.5}Sr_{0.5}CoO_3$) and LSFO ($La_{0.5}Sr_{0.5}FeO_3$), or $LaFeO_3$. It can further be

discussed how the *A*-site doping would affect the topotactic transformations in an ABO_3 perovskite oxide.

Bibliography

[1] S. Parkin and S.-H. Yang, Nature Nanotechnology **10**, 195 (2015).

[2] A. M. Goforth, P. Klavins, J. C. Fettinger, and S. M. Kauzlarich, Inorganic Chemistry **47**, 11048 (2008).

[3] K. Kuepper *et al.*, Journal of Physics: Condensed Matter **24**, 435602 (2012).

[4] C. Şen, G. Alvarez, and E. Dagotto, Physical Review Letters **105**, 097203 (2010).

[5] E. J. Wildman, J. M. S. Skakle, N. Emery, and A. C. McLaughlin, Journal of the American Chemical Society **134**, 8766 (2012).

[6] J.-C. Lin *et al.*, Advanced Materials **28**, 764 (2016).

[7] J.-H. Sim, S. Ryee, H. Lee, and M. J. Han, Physical Review B **98**, 165114 (2018).

[8] J. P. Velev, P. A. Dowben, E. Y. Tsymbal, S. J. Jenkins, and A. N. Caruso, Surface Science Reports **63**, 400 (2008).

[9] Z. Sun *et al.*, Scientific Reports **3**, 3167 (2013).

[10] M. De Graef and M. E. McHenry, *Structure of Materials: An Introduction to Crystallography, Diffraction and Symmetry* (Cambridge University Press, Cambridge, 2012), 2 edn.

[11] K. S. Knight, Journal of Alloys and Compounds **693**, 1305 (2017).

[12] D. G. Schlom, L.-Q. Chen, X. Pan, A. Schmehl, and M. A. Zurbuchen, Journal of the American Ceramic Society **91**, 2429 (2008).

[13] H. Jeen, W. S. Choi, J. W. Freeland, H. Ohta, C. U. Jung, and H. N. Lee, Advanced Materials **25**, 3651 (2013).

[14] H. Jeen *et al.*, Nature Materials **12**, 1057 (2013).

[15] J. Walter, H. Wang, B. Luo, C. D. Frisbie, and C. Leighton, ACS Nano **10**, 7799 (2016).

[16] J. M. Rondinelli and C. J. Fennie, Advanced Materials **24**, 1961 (2012).

[17] J. M. Rondinelli and N. A. Spaldin, Advanced Materials **23**, 3363 (2011).

[18] M. Singh, B. C. Yadav, A. Ranjan, M. Kaur, and S. K. Gupta, Sensors and Actuators B: Chemical **241**, 1170 (2017).

[19] G. H. N., B. B., S. G.-Q., S. C. P., and S. K. Verma, Materials Science-Poland **33**, 301 (2015).

[20] P. S. Halasyamani, in *Comprehensive Inorganic Chemistry II (Second Edition)*, edited by J. Reedijk, and K. Poeppelmeier (Elsevier, Amsterdam, 2013), pp. 41.

[21] A. Karaphun, S. Hunpratub, S. Phokha, T. Putjuso, and E. Swatsitang, Physica B: Condensed Matter **504**, 31 (2017).

[22] S. Ravi and C. Senthilkumar, Journal of Alloys and Compounds **699**, 463 (2017).

[23] P. F. K. Theopold, L. Richard, and et al., 2019).

[24] M. A. Korotin, S. Y. Ezhov, I. V. Solovyev, V. I. Anisimov, D. I. Khomskii, and G. A. Sawatzky, Physical Review B **54**, 5309 (1996).

[25] M. A. Halcrow, Chemical Society Reviews **42**, 1784 (2013).
[26] P. W. Anderson, Physical Review **79**, 350 (1950).
[27] J. Kanamori, Journal of Physics and Chemistry of Solids **10**, 87 (1959).
[28] A. Weiss, Berichte der Bunsengesellschaft für physikalische Chemie **68**, 996 (1964).
[29] P. W. Anderson and H. Hasegawa, Physical Review **100**, 675 (1955).
[30] R. I. Dass and J. B. Goodenough, Physical Review B **67**, 014401 (2003).
[31] M. Opel, Journal of Physics D: Applied Physics **45**, 033001 (2011).
[32] H. Onishi and T. Hotta, New Journal of Physics **6**, 193 (2004).
[33] E. O. Wollan and W. C. Koehler, Physical Review **100**, 545 (1955).
[34] R. Kajimoto, H. Yoshizawa, H. Kawano, H. Kuwahara, Y. Tokura, K. Ohoyama, and M. Ohashi, Physical Review B **60**, 9506 (1999).
[35] S. Y. Jang, N. Nakagawa, S. J. Moon, T. Susaki, K. W. Kim, Y. S. Lee, H. Y. Hwang, and K. Myung-Whun, Solid State Communications **149**, 1760 (2009).
[36] M. Nakamura, Y. Ogimoto, H. Tamaru, M. Izumi, and K. Miyano, Applied Physics Letters **86**, 182504 (2005).
[37] J. E. Davies, J. Wu, C. Leighton, and K. Liu, Physical Review B **72**, 134419 (2005).
[38] P. L. Kuhns, M. J. R. Hoch, W. G. Moulton, A. P. Reyes, J. Wu, and C. Leighton, Physical Review Letters **91**, 127202 (2003).
[39] J. Wu and C. Leighton, Physical Review B **67**, 174408 (2003).
[40] S. Yamaguchi, Y. Okimoto, H. Taniguchi, and Y. Tokura, Physical Review B **53**, R2926 (1996).
[41] C. Sun, R. Hui, and J. Roller, Journal of Solid State Electrochemistry **14**, 1125 (2010).
[42] H. Jeen *et al.*, Nature Materials **12**, 1057 (2013).
[43] Q. Lu and B. Yildiz, Nano Letters **16**, 1186 (2016).
[44] N. Lu *et al.*, Nature **546**, 124 (2017).
[45] V. R. Nallagatla *et al.*, Advanced Materials **31**, 1903391 (2019).
[46] C. Tassel and H. Kageyama, Chemical Society Reviews **41**, 2025 (2012).
[47] N. Ichikawa, M. Iwanowska, M. Kawai, C. Calers, W. Paulus, and Y. Shimakawa, Dalton Transactions **41**, 10507 (2012).
[48] D. A. Gilbert *et al.*, Physical Review Materials **2**, 104402 (2018).
[49] G. Rippy *et al.*, Physical Review Materials **3**, 082001 (2019).
[50] J. Li *et al.*, Nano Energy **78**, 105215 (2020).
[51] A. Rockett, *The Materials Science of Semiconductors* (Springer US, 2008).
[52] R. Eason, *Pulsed laser deposition of thin films: applications-led growth of functional materials* (Wiley-Interscience, 2006).
[53] M. Aliofkhazraei, *Advances in Graphene Science* (InTech, 2013).

[54] T. F. Kuech, in *Comprehensive Semiconductor Science and Technology*, edited by P. Bhattacharya, R. Fornari, and H. Kamimura (Elsevier, Amsterdam, 2011), pp. 1.
[55] L. W. Martin, Y. H. Chu, and R. Ramesh, Materials Science and Engineering: R: Reports **68**, 89 (2010).
[56] B. Jones and M. Zimmermann, *Good Diffraction Practice Webinar Series* (Bruker AXS Inc., 2012).
[57] N. Kemik *et al.*, Applied Physics Letters **99**, 201908 (2011).
[58] National Institutes of Standards and Technology, NIST X-Ray Form Factor, Attenuation, and Scattering Tables Form Page at <https://physics.nist.gov/PhysRefData/FFast/html/form.html>.
[59] Rigaku, The Bridge **8**, 17 (2014).
[60] M. McElfresh, Quantun Design (1994).
[61] S. Joachim and S. Hans Christoph, *Magnetism* (Springer US, 2006).
[62] J. S. Lee *et al.*, Physical Review Letters **105**, 257204 (2010).
[63] A. Bianconi, D. Jackson, and K. Monahan, Physical Review B **17**, 2021 (1978).
[64] G. v. d. Laan and I. W. Kirkman, J. Phys.: Condens. Matter **4**, 4189 (1992).
[65] Atenderholt, XASEdges at <https://upload.wikimedia.org/wikipedia/commons/b/bd/XASEdges.svg> (2009).
[66] W. S. Choi, H. Jeen, J. H. Lee, S. S. A. Seo, V. R. Cooper, K. M. Rabe, and H. N. Lee, Physical Review Letters **111**, 097401 (2013).
[67] G. van der Laan, B. T. Thole, G. A. Sawatzky, J. B. Goedkoop, J. C. Fuggle, J.-M. Esteva, R. Karnatak, J. P. Remeika, and H. A. Dabkowska, Physical Review B **34**, 6529 (1986).
[68] G. van der Laan, E. Arenholz, R. V. Chopdekar, and Y. Suzuki, Physical Review B **77**, 064407 (2008).
[69] C. Aruta, G. Ghiringhelli, V. Bisogni, L. Braicovich, N. B. Brookes, A. Tebano, and G. Balestrino, Physical Review B **80**, 014431 (2009).
[70] E. Folven, Y. Takamura, and J. K. Grepstad, Journal of Electron Spectroscopy and Related Phenomena **185**, 381 (2012).
[71] S. Anders *et al.*, Review of Scientific Instruments **70**, 3973 (1999).
[72] S. Fukushima, (Springer US, 2010).
[73] L. Wang *et al.*, Nature Materials **17**, 1087 (2018).
[74] M. J. Veit, R. Arras, B. J. Ramshaw, R. Pentcheva, and Y. Suzuki, Nature Communications **9**, 1458 (2018).
[75] D. Lu, D. J. Baek, S. S. Hong, L. F. Kourkoutis, Y. Hikita, and Harold Y. Hwang, Nature Materials **15**, 1255 (2016).
[76] J. Chen, Y. Gao, L. Wu, J. Ma, and C.-W. Nan, Materials Research Letters **5**, 329 (2017).

[77] Y. Lee *et al.*, Nature Communications **6**, 5959 (2015).
[78] L. C. Phillips *et al.*, Scientific Reports **5**, 10026 (2015).
[79] M. M. Savosta, P. Novák, M. Maryško, Z. Jirák, J. Hejtmánek, J. Englich, J. Kohout, C. Martin, and B. Raveau, Physical Review B **62**, 9532 (2000).
[80] S. S. Pillai, G. Rangarajan, N. P. Raju, A. J. Epstein, and P. N. Santhosh, Journal of Physics: Condensed Matter **19**, 496221 (2007).
[81] H. Kawanaka, A. Noguchi, M. Yokoyama, H. Bando, and Y. Nishihara, Journal of Physics: Conference Series **200**, 032033 (2010).
[82] H. Hadipour, S. Fallahi, and M. Akhavan, Journal of Solid State Chemistry **184**, 536 (2011).
[83] S. Xu, Y. Gu, and X. Wu, Solid State Communications **270**, 119 (2018).
[84] S. Ryu *et al.*, Applied Physics Letters **110**, 261601 (2017).
[85] H. Kuwahara, Y. Tomioka, A. Asamitsu, Y. Moritomo, and Y. Tokura, Science **270**, 961 (1995).
[86] D. Lu *et al.*, physica status solidi (RRL) – Rapid Research Letters **12**, 1700339 (2018).
[87] U. Shankar, R. Pandey, and A. K. Singh, Journal of Applied Physics **123**, 124301 (2018).
[88] G. Lalitha, N. Pavan Kumar, and P. Venugopal Reddy, Journal of Low Temperature Physics **192**, 133 (2018).
[89] M. Bjorck and G. Andersson, Journal of Applied Crystallography **40**, 1174 (2007).
[90] A. Doran, M. Church, T. Miller, G. Morrison, A. T. Young, and A. Scholl, Journal of Electron Spectroscopy and Related Phenomena **185**, 340 (2012).
[91] M. A. Torija, M. Sharma, M. R. Fitzsimmons, M. Varela, and C. Leighton, Journal of Applied Physics **104**, 023901 (2008).
[92] Y. Jia, R. V. Chopdekar, E. Arenholz, A. T. Young, M. A. Marcus, A. Mehta, and Y. Takamura, Physical Review B **92**, 094407 (2015).
[93] J. Scola, A. Benamar, B. Berini, F. Jomard, and Y. Dumont, Journal of Physics D: Applied Physics **50**, 045302 (2016).
[94] R. Groenen, J. Smit, K. Orsel, A. Vailionis, B. Bastiaens, M. Huijben, K. Boller, G. Rijnders, and G. Koster, APL Materials **3**, 070701 (2015).
[95] S. Yuldashev, H. C. Jeon, H. Im, T. Kang, S. H. Lee, and J. Furdyna, *Anomalous Hall effect in insulating Ga_ {1− x} Mn_ {x} As* 2004), Vol. 70.
[96] B. J. Chen *et al.*, Physical Review B **90**, 155202 (2014).
[97] S. K. Bose, J. Kudrnovský, V. Drchal, and I. Turek, Physical Review B **84**, 174422 (2011).
[98] T. Ma *et al.*, Nature Communications **8**, 13937 (2017).
[99] V. K. Malik, C. Hieu Vo, E. Arenholz, A. Scholl, A. T. Young, and Y. Takamura,

Journal of Applied Physics **113**, 153907 (2013).
[100] R. Venkatesh, M. Pattabiraman, S. Angappane, G. Rangarajan, K. Sethupathi, J. Karatha, M. Fecioru-Morariu, R. M. Ghadimi, and G. Guntherodt, Physical Review B **75**, 224415 (2007).
[101] S. Kundu, A. Das, T. K. Nath, and A. K. Nigam, Journal of Magnetism and Magnetic Materials **324**, 823 (2012).
[102] M. Sharma, J. Gazquez, M. Varela, J. Schmitt, and C. Leighton, Physical Review B **84**, 024417 (2011).
[103] J. Curiale, M. Granada, H. E. Troiani, R. D. Sánchez, A. G. Leyva, P. Levy, and K. Samwer, Applied Physics Letters **95**, 043106 (2009).
[104] S. S. P. Parkin, R. Sigsbee, R. Felici, and G. P. Felcher, Applied Physics Letters **48**, 604 (1986).
[105] R. V. Chopdekar, J. Heidler, C. Piamonteze, Y. Takamura, A. Scholl, S. Rusponi, H. Brune, L. J. Heyderman, and F. Nolting, The European Physical Journal B **86**, 241 (2013).
[106] D. Pesquera *et al.*, Physical Review Applied **6**, 034004 (2016).
[107] D. Pesquera, G. Herranz, A. Barla, E. Pellegrin, F. Bondino, E. Magnano, F. Sánchez, and J. Fontcuberta, Nature Communications **3**, 1189 (2012).
[108] A. Scholl *et al.*, Science **287**, 1014 (2000).
[109] Q. Lu and B. Yildiz, Nano Letters **16**, 1186 (2016).
[110] C. Eames, J. M. Frost, P. R. F. Barnes, B. C. O'Regan, A. Walsh, and M. S. Islam, Nature Communications **6**, 7497 (2015).
[111] H.-T. Zhang, Z. Zhang, H. Zhou, H. Tanaka, D. D. Fong, and S. Ramanathan, Advances in Physics: X **4**, 1523686 (2019).
[112] M. T. Anderson, J. T. Vaughey, and K. R. Poeppelmeier, Chem. Mater. **5**, 151 (1993).
[113] T. G. Parsons, H. D'Hondt, J. Hadermann, and M. A. Hayward, Chem. Mater. **21**, 5527 (2009).
[114] M. A. Zurbuchen *et al.*, Journal of Materials Research **22**, 1439 (2007).
[115] W. Jian, R. Jia, H.-X. Zhang, and F.-Q. Bai, Inorganic Chemistry Frontiers (2020).
[116] S. Tan, F. Sayed, S. Yang, Z. Li, J. Wu, and P. M. Ajayan, ACS Materials Letters **1**, 230 (2019).
[117] A. J. Grutter, D. A. Gilbert, U. S. Alaan, E. Arenholz, B. B. Maranville, J. A. Borchers, Y. Suzuki, K. Liu, and B. J. Kirby, Applied Physics Letters **108**, 082405 (2016).
[118] P. D. Murray *et al.*, ACS Applied Materials & Interfaces **12**, 4741 (2020).
[119] Y. Tsujimoto *et al.*, Nature **450**, 1062 (2007).

[120] Q. Zhang *et al.*, Nature Communications **8**, 104 (2017).
[121] S. K. Pandey, Physical Review B **81**, 035114 (2010).
[122] Q. Li, X. Yuan, L. Xing, and M. Xu, Scientific Reports **6**, 27712 (2016).
[123] J. Wu, J. W. Lynn, C. J. Glinka, J. Burley, H. Zheng, J. F. Mitchell, and C. Leighton, Phys. Rev. Lett. **94**, 037201 (2005).
[124] T. Ishihara, *Perovskite Oxide for Solid Oxide Fuel Cells* (Springer, 2009).
[125] Z. Zhang *et al.*, Physical Review Applied **7**, 034008 (2017).
[126] M.-H. Lee, Y. Kalcheim, J. d. Valle, and I. K. Schuller, ACS Applied Materials & Interfaces **13**, 887 (2021).
[127] P. Giannozzi *et al.*, Journal of Physics: Condensed Matter **29**, 465901 (2017).
[128] P. Giannozzi *et al.*, Journal of Physics: Condensed Matter **21**, 395502 (2009).
[129] S. Zhang and G. Galli, npj Computational Materials **6**, 170 (2020).
[130] J. P. Perdew, K. Burke, and M. Ernzerhof, Physical Review Letters **77**, 3865 (1996).
[131] A. Dal Corso, Computational Materials Science **95**, 337 (2014).
[132] A. Jain *et al.*, APL Materials **1**, 011002 (2013).
[133] H. J. Monkhorst and J. D. Pack, Physical Review B **13**, 5188 (1976).
[134] T. Ishihara, in *Springer Handbook of Electronic and Photonic Materials*, edited by S. Kasap, and P. Capper (Springer International Publishing, Cham, 2017), pp. 1.
[135] X. Liu *et al.*, Advanced Science **6**, 1801898 (2019).
[136] Y. Chen, D. D. Fong, F. W. Herbert, J. Rault, J.-P. Rueff, N. Tsvetkov, and B. Yildiz, Chemistry of Materials **30**, 3359 (2018).
[137] Chen, Yu, and S. B. Adler, Chemistry of Materials **17**, 4537 (2005).
[138] S. M. Ansari, R. D. Bhor, K. R. Pai, D. Sen, S. Mazumder, K. Ghosh, Y. D. Kolekar, and C. V. Ramana, Applied Surface Science **414**, 171 (2017).
[139] H. Yoon, A. Xu, G. E. Sterbinsky, D. A. Arena, Z. Wang, P. W. Stephens, Y. S. Meng, and K. J. Carroll, Physical Chemistry Chemical Physics **17**, 1070 (2015).
[140] E. Rauwel, S. Al-Arag, H. Salehi, C. O. Amorim, F. Cuisinier, M. Guha, M. S. Rosario, and P. Rauwel, International journal of nanomedicine **15**, 7051 (2020).
[141] M. Bahout, P. B. Managutti, V. Dorcet, A. Le Gal La Salle, S. Paofai, and T. C. Hansen, Journal of Materials Chemistry A **8**, 3590 (2020).
[142] G. Yang, W. Zhou, M. Liu, and Z. Shao, ACS Applied Materials & Interfaces **8**, 35308 (2016).
[143] N. V. Kuleshov, V. P. Mikhailov, V. G. Scherbitsky, P. V. Prokoshin, and K. V. Yumashev, Journal of Luminescence **55**, 265 (1993).
[144] K. Ravindranadh, B. Babu, M. C. Rao, J. Shim, C. Venkata Reddy, and R. V. S. S. N. Ravikumar, Journal of Materials Science: Materials in Electronics **26**, 6667

(2015).
[145] N. Sabir, W. Qayyum, S. Z. Hussain, I. Hussain, and F. Amin, *Photoluminescence properties of Co and Ni co-doped CdS/ZnS core/shell nanoparticles* (SPIE, 2018), Vol. 10507, SPIE BiOS, p.^pp. PWB.
[146] T. N. Nunley, T. I. Willett-Gies, J. A. Cooke, F. S. Manciu, P. Marsik, C. Bernhard, and S. Zollner, Journal of Vacuum Science & Technology A **34**, 051507 (2016).
[147] R. V. Chopdekar *et al.*, Journal of Magnetism and Magnetic Materials **322**, 2915 (2010).
[148] A. M. Kane, I. T. Chiu, N. J. Ahlm, R. V. Chopdekar, A. T. N'Diaye, E. Arenholz, A. Mehta, V. Lauter, and Y. Takamura, ACS Applied Materials & Interfaces **12**, 45437 (2020).
[149] M. Merz *et al.*, Physical Review B **82**, 174416 (2010).
[150] B. Bechlars, D. M. D'Alessandro, D. M. Jenkins, A. T. Iavarone, S. D. Glover, C. P. Kubiak, and J. R. Long, Nature Chemistry **2**, 362 (2010).
[151] J. H. Lee, W. S. Choi, H. Jeen, H. J. Lee, J. H. Seo, J. Nam, M. S. Yeom, and H. N. Lee, Scientific Reports **7**, 16066 (2017).
[152] N. Biškup, J. Salafranca, V. Mehta, M. P. Oxley, Y. Suzuki, S. J. Pennycook, S. T. Pantelides, and M. Varela, Physical Review Letters **112**, 087202 (2014).
[153] B. Morcos, P. Lecante, R. Morel, P.-H. Haumesser, and C. C. Santini, Langmuir **34**, 7086 (2018).
[154] K. S. Rao, T. Balaji, Y. Lingappaa, M. R. P. Reddy, and T. L. Prakash, Journal of Experimental Nanoscience **8**, 162 (2013).
[155] A. Maignan, D. Pelloquin, C. Martin, M. Hervieu, and B. Raveau, Journal of Materials Chemistry **12**, 1009 (2002).
[156] T. Motohashi, V. Caignaert, V. Pralong, M. Hervieu, A. Maignan, and B. Raveau, Applied Physics Letters **86**, 192504 (2005).
[157] A. Munoz, C. de la Calle, J. A. Alonso, P. M. Botta, V. Pardo, D. Baldomir, and J. Rivas, Phys. Rev. B **78**, 054404 (2008).
[158] J. Schwerdt, G. Goya, M. P. Calatayud, C. Herenu, P. Reggiani, and R. Goya, Current gene therapy **12**, 116 (2012).
[159] V. A. Bautin, A. G. Seferyan, M. S. Nesmeyanov, and N. A. Usov, AIP Advances **7**, 045103 (2017).
[160] S. Czekaj, F. Nolting, L. J. Heyderman, P. R. Willmott, and G. van der Laan, Physical Review B **73**, 020401 (2006).
[161] U. Bauer, L. Yao, A. J. Tan, P. Agrawal, S. Emori, H. L. Tuller, S. van Dijken, and G. S. D. Beach, Nature Materials **14**, 174 (2015).
[162] C. Bi *et al.*, Physical Review Letters **113**, 267202 (2014).

[163] D. A. Gilbert, A. J. Grutter, E. Arenholz, K. Liu, B. J. Kirby, J. A. Borchers, and B. B. Maranville, Nature Communications **7**, 12264 (2016).
[164] D. A. Gilbert, J. Olamit, R. K. Dumas, B. J. Kirby, A. J. Grutter, B. B. Maranville, E. Arenholz, J. A. Borchers, and K. Liu, Nature Communications **7**, 11050 (2016).
[165] P. Zhang, G. Yin, Y. Wang, B. Cui, F. Pan, and C. Song, Science China Physics, Mechanics & Astronomy **59**, 687511 (2016).
[166] J. J. Yang, M. D. Pickett, X. Li, D. A. A. Ohlberg, D. R. Stewart, and R. S. Williams, Nature Nanotechnology **3**, 429 (2008).
[167] R. Waser, R. Dittmann, G. Staikov, and K. Szot, Advanced Materials **21**, 2632 (2009).
[168] J. Gazquez, S. Bose, M. Sharma, M. A. Torija, S. J. Pennycook, C. Leighton, and M. Varela, APL Materials **1**, 012105 (2013).
[169] T. Yang, V. F. Mattick, Y. Chen, K. An, D. Ma, and K. Huang, ACS Applied Energy Materials **1**, 822 (2018).
[170] M. Karppinen, M. Matvejeff, K. Salomäki, and H. Yamauchi, Journal of Materials Chemistry **12**, 1761 (2002).
[171] J. Yang, W. H. Song, Y. Q. Ma, R. L. Zhang, and Y. P. Sun, Journal of Magnetism and Magnetic Materials **285**, 417 (2005).
[172] J. R. Petrie, C. Mitra, H. Jeen, W. S. Choi, T. L. Meyer, F. A. Reboredo, J. W. Freeland, G. Eres, and H. N. Lee, Advanced Functional Materials **26**, 1564 (2016).
[173] Y. Orikasa, T. Ina, T. Nakao, A. Mineshige, K. Amezawa, M. Oishi, H. Arai, Z. Ogumi, and Y. Uchimoto, The Journal of Physical Chemistry C **115**, 16433 (2011).
[174] D. Marrocchelli, N. H. Perry, and S. R. Bishop, Physical Chemistry Chemical Physics **17**, 10028 (2015).
[175] E. Enriquez, A. Chen, Z. Harrell, P. Dowden, N. Koskelo, J. Roback, M. Janoschek, C. Chen, and Q. Jia, Scientific Reports **7**, 46184 (2017).
[176] K. J. Kormondy *et al.*, Journal of Applied Physics **117**, 095303 (2015).
[177] J. Töpfer, U. Pippardt, I. Voigt, and R. Kriegel, Solid State Sciences **6**, 647 (2004).
[178] W. Paszkowicz, J. Piętosa, S. M. Woodley, P. A. Dłużewski, M. Kozłowski, and C. Martin, Powder Diffraction **25**, 46 (2010).
[179] M. E. Melo Jorge, A. Correia dos Santos, and M. R. Nunes, International Journal of Inorganic Materials **3**, 915 (2001).
[180] H. W. Yang *et al.*, Scientific Reports **4**, 6206 (2014).
[181] J. Vinson, J. J. Rehr, J. J. Kas, and E. L. Shirley, Physical Review B **83**, 115106 (2011).
[182] K. Gilmore, J. Vinson, E. L. Shirley, D. Prendergast, C. D. Pemmaraju, J. J.

Kas, F. D. Vila, and J. J. Rehr, Computer Physics Communications **197**, 109 (2015).
[183] D. R. Hamann, Physical Review B **88**, 085117 (2013).
[184] M. J. van Setten, M. Giantomassi, E. Bousquet, M. J. Verstraete, D. R. Hamann, X. Gonze, and G. M. Rignanese, Computer Physics Communications **226**, 39 (2018).
[185] M. Taillefumier, D. Cabaret, A.-M. Flank, and F. Mauri, Physical Review B **66**, 195107 (2002).
[186] C. Gougoussis, M. Calandra, A. P. Seitsonen, and F. Mauri, Physical Review B **80**, 075102 (2009).
[187] I. T. Chiu *et al.*, Physical Review Materials **5**, 064416 (2021).
[188] C. Menéndez, D. Chu, and C. Cazorla, npj Computational Materials **6**, 76 (2020).
[189] S. Pöykkö and D. J. Chadi, Physical Review Letters **83**, 1231 (1999).
[190] D. J. Keeble, R. A. Mackie, W. Egger, B. Löwe, P. Pikart, C. Hugenschmidt, and T. J. Jackson, Physical Review B **81**, 064102 (2010).
[191] Z. Feng *et al.*, The Journal of Physical Chemistry Letters **5**, 1027 (2014).
[192] P. Wadley *et al.*, Science **351**, 587 (2016).
[193] O. Gomonay, T. Jungwirth, and J. Sinova, Physical Review Letters **117**, 017202 (2016).
[194] O. Gomonay, V. Baltz, A. Brataas, and Y. Tserkovnyak, Nature Physics **14**, 213 (2018).
[195] T. Shiino, S.-H. Oh, P. M. Haney, S.-W. Lee, G. Go, B.-G. Park, and K.-J. Lee, Physical Review Letters **117**, 087203 (2016).
[196] A. Churikova, D. Bono, B. Neltner, A. Wittmann, L. Scipioni, A. Shepard, T. Newhouse-Illige, J. Greer, and G. S. D. Beach, Applied Physics Letters **116**, 022410 (2020).
[197] P. Zubko, S. Gariglio, M. Gabay, P. Ghosez, and J.-M. Triscone, Annual Review of Condensed Matter Physics **2**, 141 (2011).
[198] S. Yoon *et al.*, Nano Letters **21**, 4006 (2021).
[199] D. Meng *et al.*, Proceedings of the National Academy of Sciences **115**, 2873 (2018).
[200] H. Hsu, P. Blaha, and R. M. Wentzcovitch, Physical Review B **85**, 140404 (2012).
[201] R. L. White, Journal of Applied Physics **40**, 1061 (1969).
[202] Y. Jia, R. V. Chopdekar, E. Arenholz, Z. Liu, M. D. Biegalski, Z. D. Porter, A. Mehta, and Y. Takamura, Physical Review B **93**, 104403 (2016).
[203] J. Lüning, F. Nolting, A. Scholl, H. Ohldag, J. W. Seo, J. Fompeyrine, J. P. Locquet, and J. Stöhr, Physical Review B **67**, 214433 (2003).

[204] Y. Takamura, R. V. Chopdekar, A. Scholl, A. Doran, J. A. Liddle, B. Harteneck, and Y. Suzuki, Nano Letters **6**, 1287 (2006).
[205] J. W. Seo, E. E. Fullerton, F. Nolting, A. Scholl, J. Fompeyrine, and J. P. Locquet, Journal of Physics: Condensed Matter **20**, 264014 (2008).
[206] V. V. Kharton, E. N. Naumovich, A. A. Vecher, and A. V. Nikolaev, Journal of Solid State Chemistry **120**, 128 (1995).
[207] V. V. Kharton *et al.*, Chemistry of Materials **20**, 6457 (2008).
[208] R. W. G. Wyckoff, *Crystal Structures 1, Second edition* (Interscience Publishers, New York, New York, 1963).
[209] S. Sasaki, K. Fujino, and Y. Takéuchi, 1979).
[210] J. M. Tarascon, G. Vaughan, Y. Chabre, L. Seguin, M. Anne, P. Strobel, and G. Amatucci, Journal of Solid State Chemistry **147**, 410 (1999).
[211] X. Liu and C. T. Prewitt, Physics and Chemistry of Minerals **17**, 168 (1990).
[212] M. Haverkort *et al.*, Physical review letters **97 17**, 176405 (2006).
[213] Y. Takamura, F. Yang, N. Kemik, E. Arenholz, M. D. Biegalski, and H. M. Christen, Physical Review B **80**, 180417 (2009).
[214] A. P. Ramirez, Journal of Physics: Condensed Matter **9**, 8171 (1997).
[215] M. Abbate *et al.*, Physical Review B **46**, 4511 (1992).
[216] E. Arenholz, G. van der Laan, R. V. Chopdekar, and Y. Suzuki, Physical Review B **74**, 094407 (2006).
[217] D. W. Fischer, Physical Review B **5**, 4219 (1972).
[218] D. W. Fischer, Journal of Physics and Chemistry of Solids **32**, 2455 (1971).
[219] D. W. Fischer, Journal of Applied Physics **41**, 3561 (1970).
[220] L. A. Grunes, R. D. Leapman, C. N. Wilker, R. Hoffmann, and A. B. Kunz, Physical Review B **25**, 7157 (1982).
[221] J. Pflüger, J. Fink, G. Crecelius, K. P. Bohnen, and H. Winter, Solid State Communications **44**, 489 (1982).
[222] M. Abbate, F. M. F. de Groot, J. C. Fuggle, Y. J. Ma, C. T. Chen, F. Sette, A. Fujimori, Y. Ueda, and K. Kosuge, Physical Review B **43**, 7263 (1991).
[223] F. M. F. de Groot, M. Grioni, J. C. Fuggle, J. Ghijsen, G. A. Sawatzky, and H. Petersen, Physical Review B **40**, 5715 (1989).
[224] S. Zhang, H. Vo, and G. Galli, Chemistry of Materials **33**, 3187 (2021).
[225] H. Vo, S. Zhang, W. Wang, and G. Galli, The Journal of Chemical Physics **154**, 174704 (2021).